INVESTIGATION OF DIFFUSE MULTIPATH AT LOW GRAZING ANGLES

By

ANASTASIOS DROSOPOULOS
B. Sc. (Physics) University of Patras (Greece)
M. Sc. (Physics) McMaster University

A Thesis
Submitted to the School of Graduate Studies
in Partial Fulfilment of the Requirements
for the Degree
Doctor of Philosophy

DOCTOR OF PHILOSOPHY (1992) MCMASTER UNIVERSITY
(Ph. D) Hamilton, Ontario

TITLE: **Investigation of Diffuse Multipath at Low Grazing Angles**

AUTHOR: Anastasios Drosopoulos
B. Sc. (Physics) University of Patras (Greece)
M. Sc. (Physics) McMaster University

SUPERVISOR: Dr. Simon Haykin

NUMBER OF PAGES: xi, 93

INVESTIGATION OF DIFFUSE MULTIPATH

Abstract

In the present thesis, an experimental database is used to investigate multipath, focusing mostly on the diffuse component. The experimental conditions cover the case of CW, coherently received microwave radiation, with a sampled aperture linear array, scattered at low-grazing angles, over the sea surface. A variety of frequencies covering the entire X-band and grazing angles were employed to explore the diffuse multipath structure.

A new technique, Thomson's multiple-window-method (MWM), proves to be the proper tool for this experimental investigation. The following characteristics of diffuse multipath, for this particular class of experimental conditions, are extracted for the first time ever:

- Amplitude statistics (1st order statistics).
- Complete wavenumber and frequency domain power spectra (2nd order statistics).
- Bispectra (3rd order statistics).
- Coherencies and transfer functions between channels at different frequencies and grazing angles.
- An improved method for estimating angles of arrival.

Theory plays supportive role only, since the general problem of electromagnetic scattering from rough surfaces still remains to be solved. The main contributions from this research regarding diffuse multipath at low grazing angles are:

- The shape of wavenumber/frequency domain power spectra.
- Confirmation that amplitude statistics for the Lpol channel are K distributed.
- The wavenumber/frequency domain bispectra indicate a non-Gaussian structure for the diffuse multipath component.

Any theory that deals with microwave scattering, over the sea surface, at low grazing angles, has to take these findings into account.

Acknowledgement

I would like to express my sincere appreciation to Dr. Simon Haykin, my advisor, for providing me with an extremely interesting thesis topic, and his pointing out to me Thomson's powerful multiple window method. I would also like to thank my advisory committee, Dr.'s M. Wong, J. Litva, J. Reilly and P. Jessop for their feedback, which helped make this a better thesis. Special thanks are also due to Vytas Kezys for his many valuable and illuminating suggestions that made the topic of diffuse multipath that much more clear to me. Andy Ukrainec also, for his bringing to my attention useful information from the UNIX USENET.

Finally, the financial support of the Government of Ontario (OGS scholarships), The Natural Sciences and Engineering Research Council (NSERC) of Canada, and the Telecommunications Research Institute of Ontario (TRIO) is gratefully acknowledged.

Contents

List of Tables

List of Figures

Chapter 1

Introduction

One of the main problem areas in radar or microwave communication links, is the existence of multipath, particularly at low grazing angles where it becomes harder to construct and implement antenna receivers of high enough resolution to separate direct and multipath signal components.

Multipath refers to the reflections/scattering of a desired signal from objects in the environment, during the propagation of the direct signal from radiating source to receiver. The reflected/scattered signal reaches the receiver from a multiplicity of possible paths, hence the name multipath. It is a form of clutter that is strongly correlated with the desired signal, often leading to fading (i.e., signal attenuation due to phase opposition with multipath). This correlation also renders useless common techniques for clutter suppression like MTI (Moving Target Indication). The problem is compounded at low-grazing angles when both desired signal and multipath enter at the main lobe of the receiving antenna. Resolution of the two components can then be extremely hard if not impossible[1].

Multipath itself is composed of two components, specular and diffuse. The specular component, due to coherent scattering, is usually well defined in amplitude, phase and direction of arrival. As such it can easily be modelled, in principle, in a deterministic manner (the combined estimation of direct and specular components at sub-beamwidth separation can however be an extremely "tough" numerical problem).

The diffuse component on the other hand, is due to incoherent scattering from the rough surface(s) that the propagating signal encounters. As such it is stochastic in nature, usually with unknown statistics. This is particularly so when the scattering surface(s) changes dynamically with time, as is the case for the sea.

The most successful approach to date, in handling the multipath problem, in an angle-of-arrival estimation scenario, is to model multipath as specular scattering only and ignore the diffuse component. At low-grazing angles, for sufficiently smooth scattering surfaces (at least within the

[1]This is due to practical limitations on the physical size of the receiver antenna aperture. If the aperture could become arbitrarily large then there would be no resolution problem.

first one or two Fresnel zones) when diffuse scattering is weak, this is indeed a good approximation. However, when the surface roughness increases, the model mismatch becomes stronger and the quality of the specular approximation becomes poorer.

A complete theoretical model of multipath (or radar clutter) requires the solution of vector electromagnetic scattering from an arbitrary rough surface. This is still an open problem in its most general form, although partial, approximate and empirical approaches to specific situations offer ways of dealing with it.

The main goal of the present thesis, is to use an experimental database to investigate multipath, particularly the structure of the diffuse component at low grazing angles. This will prove valuable, for more accurate modelling of microwave scattering, from the sea surface, at low grazing angles. Such models can be used in improved angle-of-arrival estimation, where the diffuse multipath is a nuisance, as well as in remote sensing, where valuable information regarding conditions of the scattering surface can be extracted from a more accurate model (diffuse multipath/clutter is the desired signal in this case). Other areas of electromagnetic, or acoustic scattering can also benefit from the tools used, and the approach taken, in the present work.

The experimental conditions cover the case of coherently received, CW, X-band radiation, at low grazing angles, over a water surface. A variety of frequencies, covering the entire X-band, and grazing angles, together with two polarization channels, HH and VH offer a rich enough variety of information to perform this investigation. The receiver is a 32 element sampled aperture linear array. A given data snapshot of spatial samples has a wavenumber domain representation where all the different signal components can, in principle, be resolved. The direct signal and the specular multipath component appear as spectral lines while the diffuse multipath component is "coloured" in structure. The need exists to somehow estimate this mixed spectrum, in the best way possible, from a finite set of data samples. Ideally, the method used for this purpose should be non-parametric in nature so as not to be influenced by any a priori assumptions about the structure of diffuse multipath[2]. In fact, the method should be able to validate or disprove hypotheses concerning it.

A new technique, Thomson's multiple-window-method (MWM), proves to be the proper tool for this investigation fulfilling the above requirements. The following objectives are met:

1. Complete wavenumber and frequency spectra, i.e. the 2nd order statistics of diffuse multipath are extracted. A simple theoretical model of quasi-specular electromagnetic scattering from a rough surface shows good qualitative agreement *when shadowing is included.*

2. The bispectrum (3rd order statistics) is investigated and there is evidence of a non-Gaussian structure in the diffuse multipath component.

3. Coherencies and transfer functions between different frequency channels are also estimated.

4. And finally the amplitude statistics (1st order statistics) are examined and compared with the recent theory of K-distributions.

[2]E.g. forcing an ARMA model

The above characteristics of diffuse multipath are extracted for the first time ever for this class of experimental conditions. Note that the development of an improved method for estimating angles-of-arrival in a coloured noise background was also necessary as a prerequisite. The starting point for this was the F-test statistic of the MWM. A priori information was also incorporated in this estimator that improved performance.

The above results clearly show that MWM is an excellent tool for experimental investigations. Information such as the above can be used in any area of electromagnetic scattering. Radar, remote sensing, laser speckle studies, medical imaging, etc.

The main contributions resulting from this experimental investigation are:

- An improved method for estimating angles-of-arrival, used successfully to extract the direct and specular components from the data. This filtering makes possible the investigation of the diffuse multipath structure.
- The power spectrum in both wavenumber and frequency domain is estimated, displaying for the first time the experimentally observed, coloured noise shape of diffuse multipath, at low grazing angles. The importance of shadowing, through a simple theoretical model, is made evident, accounting for the observed spatial variations of diffuse multipath.
- The non-zero bispectrum, and the K-distributed amplitude, clearly show the non-Gaussian structure of diffuse multipath. This has important implications in remote sensing.

The outline of the thesis is:

Chapter 2 To provide understanding of the physical phenomena involved, this chapter offers a theoretical background, discussing the nature of the sea surface and electromagnetic scattering from it. A collection of journal papers, articles and textbooks, provide a partial "glimpse" of work in this area and some interesting ideas are highlighted.

Chapter 3 A brief outline of the experimental set-up and the signal processing "tools" used in this investigation is covered here, showing the extent and usefulness of Thomson's multi-window-method.

Chapter 4 The core of the thesis is presented here, focusing on the information extracted from the experimental database. Theory and other supporting work, leads to some important conclusions regarding diffuse multipath at low-grazing angles.

Chapter 5 The final chapter brings together the individual results of Chapter 4, and discusses the implications. Points of interest for further research are given here as well.

Appendix A A technique for generating pseudo-random-numbers from a K distribution is outlined, together with a method for extracting the relevant K distribution parameters from a given dataset.

Appendix B The details of the signal model development are outlined here. A general framework is provided, where any scattering model can be fitted and tested.

Chapter 2

Theoretical Background

Before dealing with the actual investigation on diffuse multipath, some understanding of the physics involved is required. This chapter outlines a background of useful theoretical and practical information to provide this understanding. Section 2.1 discusses the immediate propagation environment of the microwave signal, right above the sea surface, appropriate for low grazing angles. A brief description of the nature of the sea surface follows (section 2.2), making evident the complexity involved. Section 2.3 on electromagnetic scattering and rough surfaces, goes into more detail about the general problem of electromagnetic scattering from a rough surface. A survey of useful references from the open literature is also done, showing some of the usual methods of attacking this problem. The emphasis is on the microwave regime of the electromagnetic wave spectrum and rough sea surfaces. Some novel and interesting approaches are also pointed out. In section 2.4, the first principles, vector scattering integral is shown, and the difficulty of obtaining a general solution for an arbitrary rough surface is explained. Section 2.5 briefly discusses the K distribution and section 2.6 the signal model.

2.1 Sea surface boundary layer

The sea surface boundary layer consists of the atmospheric layer immediately above the sea surface (order of a few meters or tens of meters), where the electromagnetic (EM) waves of interest are propagating.

Fortunately, for EM wave propagation in the atmosphere at X-band frequencies, we do not have the strong absorptions (mainly from oxygen and water molecules) that occur at higher frequencies. What we do have is variations in the atmospheric refractive index, in both space and time, due mainly to variations in pressure, temperature and relative humidity (partial pressure of water vapour). Note that temperature inversions and humidity variations can produce a highly variable refractivity profile that can lead to duct formation. Ducts are waveguiding regions in the

atmosphere that can trap or change the propagation path to unexpected directions. In maritime environments, i.e. above the sea surface, duct formation can be a frequent phenomenon. Nathanson [88, pages 38–41] gives tables and graphs of experimentally observed ducts and it is seen that for the ranges (less than 5 km) and the low grazing angles of interest, the overall effect is probably small enough to be neglected.

Other, more normal refraction effects, occur due to the spherical nature of the earth's surface and the decrease of the average refractive index with height. Bending of horizontal rays downwards is then expected. This can be corrected by assuming an effective earth radius proportional to the actual earth radius R_E. The standard value for this proportionality constant K is 4/3. Note that K depends strongly on weather conditions and can vary along the propagation path. Diffraction phenomena, which are highly frequency dependent, are also produced by the curvature of the spherical earth. However, only in the case of a smooth sphere an analytic solution exists. As the earth's roughness increases (sea or terrain) where diffraction and multiple diffraction effects become more and more important, the complete solution of the appropriate field equations is still an open question, and an area of active research.

In the scattering models used in this work, the value $K = 4/3$ is used, as a good approximation for the short propagation distance involved. The refraction and diffraction effects that occur due to the spherical nature of the earth's surface are also neglected for the same reason. Weather conditions again, were homogeneous enough during the experimental data collection, to warrant the use of the free-space model, where the atmospheric refractive index is a constant, $n = 1$.

The physical phenomenon that cannot be ignored is that of reflection/scattering of EM waves from the sea surface.

2.2 The nature of the sea surface

Let us imagine a calm and glasslike sea surface. If a light breeze springs up the first response is the random appearance of many small wavelets, called capillary waves. These are only a few centimetres in length and a few millimetres in height and the restoring force that tries to resist the wrinkling they cause on the sea surface is the surface tension. If the driving force, the wind, dies out, the capillary waves die out too and the sea again becomes smooth. If the wind continues to blow, the capillary waves grow in size and become gravity waves (gravity is now the restoring force). These waves are more durable. They continue to propagate even if the generating wind stops.

The coupling of the wind with the sea surface can transfer energy to the waves by a direct push on their upwind faces, if they are running slower than the wind; by frictional drag, a measure of how good a grip the wind can get on the waves; and by pressure differences in the air above them. Waves may grow up to a certain height after which the growth is predominantly in length. As soon as they reach their growth limit they break (white caps) and the organized energy of the wave motion turns into disorganized turbulent motion. Water viscosity also saps wave energy, although to

a smaller extent than turbulence. The wind itself (strength, fetch and duration) and the non-linear wave-wave interactions are two more additional factors that complicate the energy balance equation besides wave breaking and water viscosity. Even today, efforts continue in oceanographic research to understand the overall energy balance of the ocean wave system.

The statistical distribution of the sea surface heights (wind-wave system) is Gaussian in the linear approximation of a superposition of non-interacting sinusoidal water waves. Waves do interact however, and their coupling is non-linear. This produces a continuous redistribution of the energy and momentum of the waves causing the statistics of the ocean surface to be non-Gaussian, non-stationary and non-homogeneous, in general.

Wave-wave interactions (linear and nonlinear) as well as interactions with land surfaces (either above or below the water) are still areas of active research. Kinsman [65] and Phillips [101] are the classic introductory references in this area. A more recent discussion at an elementary level, of the interaction of radar/radio waves with the sea surface and near surface, is also given by Apel [2].

2.3 Electromagnetic scattering and rough surfaces

The straightforward approach to the scattering problem of microwaves from the rough sea surface is to start from Maxwell's equations, impose suitable initial and boundary conditions and then solve them. Prerequisite for this however, is the exact knowledge of the value of the total field (direct and scattered) at the surface boundary. Since the sea surface can be quite rough, factors that affect the boundary field are:

- the many different scale water waves (and different wavenumber spectra, non-stationary in general, that depend on the wind in a non-simple manner)
- breaking waves, leading to foam and white caps
- edge discontinuities from the wave tops
- shadowing, depending on the receiver (Rcvr) and transmitter (Xmtr) line of sight
- diffraction and multiple scattering effects which together with shadowing become significant at the lower grazing angles
- EM wavelength, polarization and incidence angle

Clearly, measuring the total field at the sea surface boundary to the required accuracy is impossible.

In applications in the radar area (tracking, surveillance or navigation) the scattered sea return is a nuisance, hence the name sea clutter. The primary functions of radar (detection, tracking and classification of targets) are impaired. In remote sensing on the other hand, where the target of interest is the sea surface itself, this is the desired signal, offering the potential to extract much

useful information on weather and wind conditions, internal wave structure, surface water quality and possibility of contaminants, to mention a few. These potential applications have provided a powerful motivation towards a better understanding of sea return and much progress has been made since the late forties.

One of the earliest discussions on sea return appears in Kerr [63]. Spherical surface reflections are nicely taken care of with the introduction of a divergence factor and some simple models of the properties of the sea surface scattering cross section are investigated. The model simplicity, combined with the rather meagre amount of experimental data available at the time, allows only some general conclusions to be drawn. The material however, is still relevant today as a useful starting point for serious modelling of the propagation channel. Note that since most radar systems have co-location of Xmtr and Rcvr antennas, most of the published data in sea return refers to backscattering. Data for the forward scatter case, such as the experimental dataset used in this thesis, is much less common.

It is currently accepted that sea surface scattering at microwave frequencies is predominantly done by capillary waves (Bragg resonant scatterers at microwave wavelengths) with the larger gravity waves providing an underlying modulation. The exception is the specular direction where specular scatter predominates [132]. Note that the Bragg resonant wavelength depends on the local angle of incidence which means that capillary waves of a number of different wavelengths contribute to the scattering. Their distribution over the surface of the larger gravity waves is not uniform and the exact shape is still not well known. To further complicate matters, foam and large water droplets are generated when waves break, and there is still no adequate theory to describe their interaction with microwaves. Furthermore, for grazing incidence, shadowing becomes important. Portions of the wave being observed may be shadowed by other in-between waves. Again, near grazing, both constructive and destructive interference may take place between the direct EM wave incident on an ocean wave and that reflected off the surface. Both shadowing and interference effects, modify significantly the received signal from what it would be if only the Bragg scattering mechanism was involved.

Energy not appearing in the well-defined specular direction must either be absorbed in the underlying surface, scattered into wide angular regions including backscatter or clutter components unrelated to the specular angle, or forward scattered in a conical lobe about the specular angle. All three phenomena have been observed in varying degrees. Most of this energy appears in the forward direction (due mostly to capillary waves from the sea surface; and small discontinuities – order of wavelength – from land surfaces, including twigs and vegetation). Most of the forward scattered energy (for slightly to medium rough surfaces) [12, 16], appears to originate from the *glistening surface* (similar to the Fresnel zones) according to a normally distributed surface facet model. Scattering is done by the tilted facets and the glistening surface is a function of Xmtr/Rcvr geometry and surface properties, such as roughness and correlation distance. For low elevation targets the glistening surface extends essentially to the horizon, and energy from the more distant portions of the surface is subject to multiple scattering by intervening surface features (shadowing

phenomenon). Barton [11, 12] emphasizes the existence of a *horizon* component based on the observation that, small variations in elevation angle of the receiver antenna, correspond to larger scattering areas near the horizon, which results in a larger amount of power received.

The first order statistics of sea surface scattering refer to the amplitude distribution which could be Rayleigh, lognormal or Weibull. More recently, all these amplitude distributions are found to be particular cases of the more general family of K-distributions. Second order statistics (correlations and spectra) depend on so many factors that it is almost impossible to find a model that incorporates all of them. Several experimentally observed wavenumber spectra, have asymmetrical shapes and may even be bimodal. Both first and second order statistics depend on the radar resolution cell. If this is large, it is bound to have a large number of scatterers leading to Gaussian-like behaviour and a Rayleigh amplitude distribution (from central limit theorem arguments). For high resolution radars where the cell size becomes smaller, Gaussianity breaks down leading to the appearance of coherent clutter spikes that can last for several seconds. Third order and higher statistics, are supposed to be able to extract non-linearities (and therefore non-Gaussianities) of an underlying stochastic process. One of the first applications of the bispectrum (3rd order statistics) was by Hasselmann et al. [50] on the bispectra of ocean waves. Recently, Chen and Fung [28] have started investigating non-Gaussian distributed random surfaces. Apparently, the introduction of skewness can account for the difference between upwind and downwind scattering coefficients and the level difference between VV and HH polarizations. It is also now well admitted that sea clutter exhibits nonstationary properties above sea state 3. Constant false alarm (CFAR) detection methods based on power contrast between cells are endangered, as the desired target may be eliminated if it exists in a cell with strong clutter.

The sea surface is an example of a random surface and much of the work done on EM scattering from general rough surfaces is applicable here as well. An example with some similarity to microwave scattering from the sea, is that of laser light scattering from metallic or dielectric rough surfaces. Laser speckle is analogous to microwave clutter spikes and laser scattering from phase screens (fictitious plane surfaces that randomize the phase of a propagating wave without affecting its amplitude – used as surface models) originally led to the development of the family of K-distributions.

The scattering of EM waves from a randomly rough surface has been studied extensively for a number of years [16, 13, 97]. Of the many theories that have been proposed, there are two that are most widely used. The Kirchhoff, also called Physical Optics or tangent plane approximation and the small perturbation method (SPM). The Kirchhoff approximation (KA) is applicable to surfaces with gentle undulations, whose average horizontal dimension is large compared with the incident wavelength λ. In other words, the radius of curvature of the surface irregularities is large compared to λ. SPM on the other hand, requires both the surface standard deviation and correlation length to be smaller than λ. Note that both approaches, as usually developed, break down when incidence and/or observation angles come close to grazing, and neither method applies when the surface is

rough on length scales comparable to a wavelength.

In KA, the field scattered by a point on the surface is approximated by the field that would be scattered by a tangent plane at that point. The validity of KA [138] holds for

$$2kr_c\cos^3\theta >> 1$$

where $k = 2\pi/\lambda$, the wavenumber, r_c is some minimum or average radius of curvature, and θ is the local angle of incidence. The implication is, that for backscattering, the theory is better for large angles of incidence and is expected to perform poorly for the smaller ones. Bass and Fuks [13] note that for the forward scattering case the limits of validity should be larger. Indeed, an excellent experiment on rough surface scattering (of laser light from carefully prepared material samples) conducted by O'Donnell and Mendez [96] in 1987, supports the above claim. On the other hand, the comment made by Long [74, page 78] should be kept in mind: that models based on KA, as usually implemented, describe "... a smooth undulating surface with hills much less than a wavelength in height and separated by hundreds of wavelengths ... not typical of most terrain". Note also that depolarization effects or energy conservation are not correctly predicted. A step in the right direction is, taken by Chen and Ishimaru [27, 55] where KA is extended to handle very rough surfaces. A second order scattering formulation is implemented, with shadowing included, that is still mathematically tractable (at least for the 1-dim case that the paper discusses), and the experimentally observed backscattering enhancement seems to be contained in this approach.

In SPM, as in any perturbation approach, a parameter ϵ is introduced. Conventionally, this is taken to be the root-mean-square rough surface height (with appropriate units). In the original formulation, the Rayleigh hypothesis is used to express the reflected and transmitted fields into upward- and downward-going waves, respectively. The field amplitudes are then determined from the boundary conditions and divergence relations. More recently, the extended boundary condition (EBC) method, in combination with the extinction theorem (where the induced surface fields extinguish the incident field below the surface) does away with some mathematical ambiguities of the Rayleigh hypothesis (although giving the same final expansions for the scattered fields) [92, 90, 91]. Series expansions of the surface and scattered fields in terms of $k\epsilon$ are then done. By equating same order terms the desired order solutions can be obtained. The 0th order solutions are just the reflected and transmitted fields of a flat surface. 1st order give the lowest order incoherent scattered intensities and it is only with the 2nd order solutions, giving the lowest order correction to the coherent reflection and transmission coefficients, that depolarization effects are evident (expressions become mathematically very complicated for higher orders).

A reformulation of SPM in terms of series expansions of the phase of the fields (phase perturbation) done by Winebrenner [138] and Winebrenner and Ishimaru [140, 139], leads to a resummation of the expansion series that seems to have much better convergence properties. Simulations with the phase perturbation method (PPM) [56] also indicate that it is not limited to either small roughness or gentle undulations and the validity regime, covers the validity regimes of classical KA, SPM, and

also the intermediate region of roughness scales. Both approaches, i.e. 2nd order KA and PPM show promise as scattering models. At the present time though, they are not yet fully worked out for vector EM scattering from an arbitrary rough surface.

Indeed, the popular approach at the moment to this problem is to combine conventional KA and SPM into a composite or two-scale model. The KA covers the large scale irregularities (large gravity waves for sea surface scattering) while SPM handles the ripples or capillary waves. A phenomenological parameter needs to be introduced though, the critical wavenumber k_d, that splits the roughness spectrum into large and small scale. The value usually chosen for k_d is $\approx \frac{1}{3}$ the Bragg wavenumber [118, 119] which makes the computed scattering cross-section to be roughly similar to that of KA. The combination of the two scales can be done either in the EM field (coherent) or in the intensities (incoherent — simpler mathematically). The two-scale composite model extends the limits of validity of KA or SPM. However, at low grazing angles (high incidence angles) the usual shadowing, diffraction and multiple scattering effects are still significant and the model breaks down. Note also, that the recent trend, is towards numerical computation of the scattered field [35].

Winebrenner's [138] recent PhD thesis (1985) has an excellent discussion on the state-of-the-art of rough surface scattering theories up to 1985. Other useful references are: Ulaby et al. [130], and Tsang et al. [129]. A partial smorgasbord of papers, dealing with sea surface and rough surface scattering, that were found useful, is outlined in the following.

The general theory of rough surfaces is provided by the early papers of Longuet-Higgins [75, 76, 77]. They offer interesting points and a good example of the mathematical modelling of a random surface.

An early model of sea surface scattering by DeLorenzo and Cassedy [34] in 1966 investigates a possible scattering mechanism. Models at the time were postulating that the sea surface is composed of a dense collection of *independent* small scatterers, therefore coherent scattering should occur only in the specular direction, implying backscatter to be incoherent. Experiments however show that both coherent and incoherent backscatter is possible. To account for this, the model suggests that two separate mechanisms are responsible for sea returns (not the same as for the two-scale model that is introduced later). Coherent returns are postulated to be reflections from large scatterers which are superimposed on the small scatterers (the small being though to cause the incoherent returns). Little physical support is given for these scatterers. The concept however of scattering from a narrow-band surface (i.e. surface whose statistical representation is narrow-band) is introduced and this can lead to strong coherent returns in other directions than the specular. Peaks in the RF spectra at harmonics of the ocean wave spectral peak can be and are observed. The construction of a random process with a narrow-band spectrum peaking at a frequency other than zero is also discussed and the development seems to be similar to Rayleigh's SPM.

Simulations of scattering from 1-dim perfectly conducting rough surface can be found in [4, 93, 72, 46, 25] (the latter two have a good discussion on how to generate Gaussian correlated random surfaces numerically although Mitchell [84] and Ogilvy [97] were also found useful. Chen and

Ishimaru [27, 55] perform some Monte-Carlo simulations for scalar wave scattering from 1-dim, soft (Dirichlet boundary conditions), Gaussian rough surfaces. Extraction of statistical parameters of random surfaces from the surface spectrum (claimed to be more robust in some respects) is outlined in [107]. Bidirectional scattering by [69].

A precise quantitative relationship [7] between the roughness heights and the winds for the longer higher gravity waves is complicated by several factors. First, it takes several hours for waves to build up to their full strength under the influence of the wind; for example it takes 20 hours for the sea to build up to full or "saturated" height under 15 knot winds. In most instances, the winds will not stay constant either in magnitude or direction for this long a period and hence the sea is rarely saturated at the longer wavelengths. Second, the homogeneity of the wave spectrum aroused in a given region depends on the spatial area over which the winds are blowing; this area is called the "fetch" and may be as small as 10ℓ km in length. Third, part of the roughness is due to winds or storms located far away in space and/or time from the region of interest; this is called "swell'. It is usually quite directional and "narrowband" and hence its spectrum appears as spikes in the 2-dim surface wavenumber plane. Some of the simpler ocean wave height spectrum models (e.g. Neumann-Pierson and Phillips) developed by oceanographers over the past 15 years usually neglect the effect of limited fetch and swell. They furthermore assume that the driving winds have been blowing sufficiently long, leading to a fully developed sea. There are other, much more complex models created by research panels of people working in this area that attempt to correct and predict these effects.

The surface height distribution is not the only distribution of interest when dealing with the sea surface. In the facet model the importance of the proper slopes for reflection/scattering in a given direction is clearly evident. Cox and Munk [31, 32] is the classic work on experimental data on the slope distribution of the sea surface spectrum (check also [136] for a correction). They show that the wave spectrum is closer to being isotropic than the cosine-squared directionality assumed in the Neumann-Pierson and also some small deviations from normality and Gaussianity.

Barrick [7, 8] develops an effective surface impedance model for wave propagation over the sea, applicable for EM waves in the MHz range (HF and VHF). He points out [8] that at microwave frequencies the ocean sea surface is "composite" and thus more difficult to analyze. Together with Bahar [9] they correct Kodis [67] in deriving the expression for the quasispecular scattering cross section at high frequencies for perfectly conducting surfaces. An older paper of Barrick [6] discusses a preliminary formulation of rough surface scattering based on the specular point theory. Fung and Chan [44] talk about backscattering by composite rough surfaces, and Brown [24] on approximate theories for rough surface scattering.

Mitzner [85] corrects Beckmann [16] on the change in polarization on reflection from a tilted plane and Beckmann reciprocates by writing a book on depolarization of EM waves [15]. Torrance and Sparrow [125] expand on a geometrical theory of diffuse reflections from a rough surface.

Eftimiu [41, 42] takes a different approach. The rough surface is viewed as a realization of a stochastic process and the scattered field as a nonlinear stochastic functional of this process. An expansion in orthogonal Wiener-Hermite functionals is then performed. The point of view is interesting but also complicated and difficult to apply. More promising appears to be the excellent paper by Gallatin [48], describing a functional-integral representation of rough surfaces, using methods already applied to quantum field theory. Lower order terms in his expansion coincide with the classical approach of a Gaussian surface with the discontinuity of the correlation function at the origin nicely taken care of (based on physical grounds). Both the exponential and Gaussian autocorrelation functions that are usually assumed to hold in an ad-hoc manner, fall out of this formalism for a certain range of values of the expansion coefficients. There also are parameters to account for possible non-zero skewness and/or curvature in the probability distributions involved. The modified Bessel function appears as well, for 2-dim random surfaces (see current ideas on K-distributions) and higher order terms in Gallatin's expansion naturally introduce fractals.

A series of papers in the optics literature [141, 142, 143] discuss the application of polarization or colour [66] to separate specular highlights from images, thereby enhancing the underlying object image. This concept could be applied to radar and indeed [104] outlines a technique of adaptive processing of microwave sea echo for suppression of strong reflections from scatterers based on frequency diversity.

Straiton and Tolbert [115] in 1956 employ a similar experimental set-up to ours, although with circular polarization and incoherent reception. The simple graphical analysis indicates that the received signal is composed of a direct, specular and a normally distributed fluctuating component.

Berg and Hoop [17] offer a nice discussion on calculating the scattered and transmitted EM field between two media separated by a rough surface interface. In their approach, the field equations and radiation condition are satisfied analytically, while the boundary conditions at the interface are satisfied numerically (this has to do with analytic extension in the vicinity of the interface). Apparently, the iteration procedure employed in the numerical extension works well.

Glazman [49] performs an analysis of the Kirchhoff approximation for a well-developed sea. Good points are made and a list of references on the current status of actual ocean wave spectra is given. Of note is the appearance of a microscale length in his formalism that can lead to fractal behaviour. Mudaliar and Lee [87], a good example of SPM application, talk about anisotropy and a modified radiative transfer function that to a first-order approximation is potentially useful in passive remote sensing.

Valenzuela [132] reviews theories for the interaction of EM and ocean waves emphasizing backscattering. A graph of the dominant physical mechanisms and pertinent theories of scattering for the backscatter case vs. angle of incidence is given there. Polarization dependency is also discussed. Note that backscattering of X-band waves is greater for vertical than horizontal polarization, becoming more so for increasing angle of incidence and sea water dielectric constant. Spike occurrence, however, is greater for the horizontal case. Wright [144] introduced in 1968 the two-scale or

composite surface model to better explain experimental data. In this model the sea is assumed to be composed of an infinite number of slightly rough patches. The net scattered power is an average of the scattered power from a single patch over the distribution of slopes of the dominant waves of the ocean (non-coherent formulation – in the coherent, it is the scattered field that is treated so). For microwaves the dominant waves are the long gravity waves and the slightly rough patches are created by the capillary waves. This tilting of the patches (small scale roughness) by the gravity waves (large scale roughness) can also cause depolarization. Basically, the nature of the radar return from the sea at microwave frequencies is resonant, or Bragg, scattering. The non-coherent composite-surface model is quite adequate for angles of incidence from normal to near grazing, for the lower radar frequencies (up to 0.5 GHz). For the higher frequencies though, a disagreement for horizontal polarization becomes evident near grazing. Another dubious assumption is that the two roughness scales are uncorrelated. The converse has been shown to hold by Keller and Wright [62] in 1975. This has implications both for scattering and in the energy transfer from atmosphere to ocean.

Holliday [52, 53] uses SEASAT-A and SARSEX synthetic aperture radar (SAR) data for small incidence angles and backscattering. The results are interesting. There are cases where the assumed Bragg scattering model fails. It is basically a small amplitude effect as its derivation from SPM demonstrates. The underlying SPM assumption is that $4k_z^2 < \sigma_h^2 >$ is smaller than one, where k_z is the z-component of the radar wavevector and $< \sigma_h^2 >$ the mean square wave height. For the SEASAT-A SAR data $k_z = 24.6\ m^{-1}$ and $< \sigma_h^2 >$ can easily be $0.1\ m^2$ for modest sea states. Consequently, scattering mechanisms involving tilt can be as important as resonant scattering at the Bragg wavenumber. Holliday develops a new model using a finite surface amplitude formulation instead of infinitesimal for the scattering of EM waves from the ocean surface (lowest order equivalent to Kirchhoff). Details are given of the model derivation for a perfectly conducting surface and the tie with actual ocean spectra is neatly done. The second order iterations are seen to be equivalent to SPM. There still are some problems with depolarization; higher order iterations may be needed, making the formalism cumbersome. Holliday also points out that mechanisms producing ocean wave spectral perturbations do not appear to be well understood, especially for large surface currents produced by flows over bottom topography and internal waves. It is convenient to make simple assumptions (like weak hydrodynamic interaction theory in the relaxation time approximation) and hope that they work. For this reason, he notes that his model has the "defect" of not including the significant wave packet advection effects or the case of appreciable perturbations. See also [118].

Wetzel [137] is another good paper, discussing some of the fine points of backscattering at extreme grazing angles (less than 1°). He uses Smith's shadowing function and also notes that "evaporation establishes a persistent humidity layer about 10 m thick over the sea surface, and extensive measurements have shown that this layer defines propagation conditions close to the surface for at least 85 % of the time". For a ground based radar (height around 20 or 50 m) this layer begins to affect things significantly, starting from ranges about, or greater than 5 km. Some plausible

arguments are used to derive realistic parameter values for the sea surface, and it is also explained that scattering at low grazing angles is done by visible (to the radar) scattering "islands". When the range increases, approaching the horizon, even though the size and density of the "islands" might remain the same, the spacing between them increases rapidly. If shadowing did not exist then we would expect to see an increased return from the horizon (Barton's horizon effect) due to the larger visible area that is compressed within the antenna's beamwidth. Wetzel explains that the return will peak before then, i.e. there is no horizon component (in agreement with our own experimental data). An interesting modification to the shadowing function is also done, for grazing angles less than about 1 or 2 degrees. Shadowing is separated into micro- and macro- shadowing and both effects are included. The scarcity of accurate and reliable measurements in the open literature for such regimes is also pointed out, and a list is given on the state-of-the-art for microwave backscattering at low grazing angles:

- For grazing angles in the neighbourhood of 6° the scattering cross section for vertical polarization is about 10 times greater than for horizontal.
- For angles between 2° and 6° backscatter begins to differentiate, the vertical polarized returns remaining noiselike, while the horizontally polarized returns take on an increasingly spiky aspect, always visually associated with breaking water.
- At angles below 2° the Doppler frequencies of the horizontal returns are consistent with the group velocity appropriate to the prevailing wind-wave system while the vertical have somewhat lower frequencies (about 40%).
- At angles below 1° it is suggested that the returns for both horizontal and vertical might approach each other in both magnitude and appearance.

Nathanson [88] devotes a chapter to sea and land backscatter verifying the above observations. More recently Trizna and Hansen [127, 128], examine radar sea backscatter, at low grazing angles, for HH and VV polarizations, for a variety of sea states. They look into the fit of the Weibull distribution to the data, observing that a single Weibull distribution fits the VV data, while the HH data frequently required two independent Weibull fits. Again, the occurrence of sea spikes is more frequent in the HH case. The implication is that different scattering mechanisms are responsible for the two polarizations.

The development of a shadowing theory has an interesting history. The first paper appearing in this area was by Beckmann [14] in 1965. Brockelman and Hagfors respond with [22] where by using a better physical random number generator show some of Beckmann's weaknesses. A lively debate follows in the discussion following the last paper. Credit should be given to Beckmann for his original formulation. Latter publications by Smith [114] and Wagner [133] expand his ideas without the original errors, and Sancer [109] does a full formulation of KA with shadowing properly included. The final word is written by Lynch and Wagner [79] where they discuss shadowing, multiple scatter

(double scatter) and energy conservation for 1-dim rough surfaces. They show, using an incoherent scattering approach, that these effects become significant for large incidence (low grazing) angles and/or appreciably rough surfaces.

Leader [71] discusses incoherent backscatter from rough surfaces. His derivation incorporates effects of local polarization tilt angles, leading to a first-order cross-polarized scattering component. In [70] he investigates a coherent model (one of the few papers that do this).

Recent work by Plant and Keller [102] discuss experimental evidence of Bragg scattering in microwave Doppler spectra of sea return. Wright [145] talks about the modulations in amplitude, velocity and orientation that the larger-scale motions of the ocean surface inflict upon the short gravity-capillary waves (predominant radar scatterers for microwave frequencies). Data from water tank experiments are used to show some interesting phenomena (e.g. Doppler splitting appearing when wind increases). The implication for SAR imagery is, that more parameters need to be sensed than is currently the case.

Mrstik and Smith [86] discuss some of the multipath limitations of low angle tracking for a monopulse system. They check simple models like Lambert's and Beckmann and Spizzichino's with and without Barton's modifications. Some theoretical performance limits are derived, which experimental data up to 1978 do not disqualify (the author's however point out that there is a great scarcity of data for forward scattering).

Masuko et al. [80] give some backscattering measurements for X and K_a bands from the ocean surface with airborne scatterometers.

An excellent paper by Donelan and Pierson [36] discusses radar backscattering and equilibrium ranges in wind-generated waves. A two-scale incoherent model is applied and a systematic and thorough effort is made to include as many physical effects as possible (e.g. breaking, viscosity, wedges, nonlinear interactions) based on experimental watertank data as well as satellite (RADSCAT). This is clearly the direction such research should take.

Valenzuela [131], Boerner et al. [20] and Fung [43] discuss aspects and mechanisms of polarization and depolarization in rough surface scattering. Fung and Eom [47] also include multiple scattering effects for a bistatic geometry. Another series of papers [18, 19, 89] discuss nonideal system effects on depolarized measurements, a must for extracting the right information when dealing with different polarization channels.

2.4 EM rough surface scattering

The starting point in the mathematical treatment of the vector EM scattering from rough surfaces is Huygen's principle. This states that the field at an observation point $\mathbf{r}$, caused by a number of radiating sources enclosed by a surface S, can be expressed by the field values on S and some appropriate Green's function, through a vector integral representation. Details can be found in Sancer [108], Kong [68], Ulaby et.al. [130], Chew [29], Cho[30] and Tai [116, 117] among others,

leading to the following expressions for the scattered field

$$\mathbf{E}^s(\mathbf{r}) = \oint_{S'} dS' \{i\omega\mu \mathrm{G}(\mathbf{r}|\mathbf{r}') \cdot [\hat{\mathbf{n}} \times \mathbf{H}(\mathbf{r}')] + [\nabla \times \mathrm{G}(\mathbf{r}|\mathbf{r}')] \cdot [\hat{\mathbf{n}} \times \mathbf{E}(\mathbf{r}')]\} \tag{2.1}$$

$$\mathbf{H}^s(\mathbf{r}) = \oint_{S'} dS' \{-i\omega\epsilon \mathrm{G}(\mathbf{r}|\mathbf{r}') \cdot [\hat{\mathbf{n}} \times \mathbf{E}(\mathbf{r}')] + [\nabla \times \mathrm{G}(\mathbf{r}|\mathbf{r}')] \cdot [\hat{\mathbf{n}} \times \mathbf{H}(\mathbf{r}')]\} \tag{2.2}$$

An $e^{-i\omega t}$ time dependence is assumed, $\mathbf{r}$ is the observation point, $\mathbf{r}'$ is the surface point and $\mathrm{G}(\mathbf{r}|\mathbf{r}')$ is the dyadic Green's function of the particular problem, related to the corresponding scalar Green's function through

$$\mathrm{G}(\mathbf{r}|\mathbf{r}') = \left[\mathrm{I} + \frac{1}{k^2}\nabla\nabla\right] g(\mathbf{r}|\mathbf{r}')$$

and S' is the *illuminated* part of the scattering surface.

The total field is assumed to be the sum of the incident and scattered fields

$$\mathbf{E}(\mathbf{r}) = \mathbf{E}^i(\mathbf{r}) + \mathbf{E}^s(\mathbf{r})$$

$$\mathbf{H}(\mathbf{r}) = \mathbf{H}^i(\mathbf{r}) + \mathbf{H}^s(\mathbf{r})$$

so that inside the integrands in relations (2.1) and (2.2) it is seen that only the tangential components of the total field on the boundary surface are required. In terms of the scalar Green's function, the above representation, together with the Franz and Stratton-Chu representations (the two other most common) are displayed in table 2.1.

Note that in the Stratton-Chu representation *both* the tangential *and* the normal components of the field on the scattering surface S' are required. Sancer [108], also points out the problem of an associated boundary line charge (due to the finite size of the scattering surface) that has to be explicitly included as well. This charge is implicitly included in the other representations.

Interestingly enough, Cho [30] is the only author that I am aware of, who points out that even these integral representations are defective, in the sense that for a given complex scatterer there exists a countable set of operating frequencies where these representations cease to portray the scattered EM field. A unique solution to the EM scattering problem in R^3 has to satisfy the proper Dirichlet or Neumann boundary conditions in a suitable Banach space and the associated operators in this space have to be compact (the necessary requirement for a stable numerical solution). Cho claims that this is still an open question for R^3, for the case of the integro-differential equations in table 2.1. Other authors, e.g. Chew [29], claim that the radiation conditions are enough to guarantee uniqueness, since an analytic extension is possible for the fields above the highest surface point and below the lowest surface point, which leaves the problem of specifying the boundary conditions accurately enough.

Indeed, the problem of specifying accurate boundary conditions is the "toughest". One approach is to take the limit as $\mathbf{r}$ gets close to $\mathbf{r}'$, generating an iterative solution from one of the equation sets in table 2.1. Singularity questions need to resolved then, which is where the extinction theorem with the extended boundary conditions is useful. The brute-force numerical approach,

Table 2.1: The three most common integral representations in terms of the scalar Green's function.

Integral representation (2.1) and (2.2)

$$\begin{aligned}
\mathbf{E}^s(\mathbf{r}) &= \oint_{S'} dS' \Big\{ i\omega\mu g(\mathbf{r}|\mathbf{r}')[\hat{\mathbf{n}} \times \mathbf{H}(\mathbf{r}')] + \frac{i\omega\mu}{k^2} \nabla\nabla g(\mathbf{r}|\mathbf{r}') \cdot [\hat{\mathbf{n}} \times \mathbf{H}(\mathbf{r}')] \\
&+ \nabla g(\mathbf{r}|\mathbf{r}') \times [\hat{\mathbf{n}} \times \mathbf{E}(\mathbf{r}')] \Big\} \\
\mathbf{H}^s(\mathbf{r}) &= \oint_{S'} dS' \Big\{ -i\omega\epsilon g(\mathbf{r}|\mathbf{r}')[\hat{\mathbf{n}} \times \mathbf{E}(\mathbf{r}')] - \frac{i\omega\epsilon}{k^2} \nabla\nabla g(\mathbf{r}|\mathbf{r}') \cdot [\hat{\mathbf{n}} \times \mathbf{E}(\mathbf{r}')] \\
&+ \nabla g(\mathbf{r}|\mathbf{r}') \times [\hat{\mathbf{n}} \times \mathbf{H}(\mathbf{r}')] \Big\}
\end{aligned}$$

Franz representation

$$\begin{aligned}
\mathbf{E}^s(\mathbf{r}) &= \nabla \times \oint_{S'} dS' [\hat{\mathbf{n}} \times \mathbf{E}(\mathbf{r}')] g(\mathbf{r}|\mathbf{r}') + \frac{i}{\omega\epsilon} \nabla \times \nabla \times \oint_{S'} dS' [\hat{\mathbf{n}} \times \mathbf{H}(\mathbf{r}')] g(\mathbf{r}|\mathbf{r}') \\
\mathbf{H}^s(\mathbf{r}) &= \nabla \times \oint_{S'} dS' [\hat{\mathbf{n}} \times \mathbf{H}(\mathbf{r}')] g(\mathbf{r}|\mathbf{r}') - \frac{i}{\omega\mu} \nabla \times \nabla \times \oint_{S'} dS' [\hat{\mathbf{n}} \times \mathbf{E}(\mathbf{r}')] g(\mathbf{r}|\mathbf{r}')
\end{aligned}$$

Stratton-Chu representation

$$\begin{aligned}
\mathbf{E}^s(\mathbf{r}) &= \oint_{S'} dS' \{ i\omega\mu [\hat{\mathbf{n}} \times \mathbf{H}(\mathbf{r}')] g(\mathbf{r}|\mathbf{r}') + [\hat{\mathbf{n}} \cdot \mathbf{E}(\mathbf{r}')] \nabla' g(\mathbf{r}|\mathbf{r}') + [\hat{\mathbf{n}} \times \mathbf{E}(\mathbf{r}')] \times \nabla' g(\mathbf{r}|\mathbf{r}') \} \\
\mathbf{H}^s(\mathbf{r}) &= \oint_{S'} dS' \{ -i\omega\epsilon [\hat{\mathbf{n}} \times \mathbf{E}(\mathbf{r}')] g(\mathbf{r}|\mathbf{r}') + [\hat{\mathbf{n}} \cdot \mathbf{H}(\mathbf{r}')] \nabla' g(\mathbf{r}|\mathbf{r}') + [\hat{\mathbf{n}} \times \mathbf{H}(\mathbf{r}')] \times \nabla' g(\mathbf{r}|\mathbf{r}') \}
\end{aligned}$$

where different realizations of a 2-dim rough surface are generated, would require samples at sub-intervals of the wavelength λ. Huge matrices would be the result, overwhelming the capacity of today's computers. This is the reason why most numerical simulations deal with 1-dim idealizations of rough surfaces. Useful results can still be obtained in such a case, for isotropic, cylindrical surfaces, at least in showing comparative performance and validity regimes of different methods.

Note however, the use of the conjugate gradient method [35] for a 2-dim metallic rough surface. This could be the approach required, for an effective numerical solution of the scattering problem from a rough surface.

2.5 The K distribution

Recently, another approach to the scattering problem, that sidesteps the mathematical difficulties pointed out in the last section, has proved itself to be quite successful. This is the adaptation of the random walk model to scattering. Although it does not represent in any sense an exact solution to Maxwell's equations, this empirical model usually seems to show excellent agreement with experimental data.

The starting point is the modelling of the scattered field at some frequency ω, at the detection point $\mathbf{r}$, at time t, from a given radar resolution cell, as the contribution from N scatterers:

$$\mathbf{E}^s(\mathbf{r},t) = \sum_{i=1}^{N} \mathbf{a}_i(\mathbf{r},t)\exp[j\phi_i(\mathbf{r},t)]\exp(j\omega t)$$

Here $\mathbf{a}_i(\mathbf{r},t)$ is a real "form factor" governing the angular distribution of radiation from the ith scatterer, while $\phi_i(\mathbf{r},t)$ is a phase factor depending on its position at time t with respect to the observation point $\mathbf{r}$. By imposing, various properties on N, a_i or ϕ_i, the correlation properties of the surface in both space and/or time can easily be brought into play, leading eventually to the K distribution as the probability distribution of the amplitude of the scattered field [60, 61].

The theory was originally developed for electromagnetic scattering by random phase screens by Jakeman and Pusey [57, 58] when they noticed that similar results held for microwave sea echo. After their first publication in this area [59] in 1976, a great number of other workers found that indeed the agreement with experiment is generally excellent.

Watts [134, 135] and Hou and Morinaga [54] develop the detection aspects in K-distributed clutter and Nohara and Haykin [95] use an extensive database to show an excellent fit of radar backscatter data with the K-distribution plus thermal noise model. Oliver [98] and Oliver and Tough [99] outline a method of simulating correlated K-distributed clutter, which should be closer to the real world since real clutter is indeed correlated in both time and space. Note also the recent letter by Armstrong and Griffiths [3] regarding such simulations.

From another, more empirical point of view, the K-distribution clutter model is explained as follows: For radars with low spatial resolution, where the dimensions of the resolution cell are

generally much greater than the sea swell wavelength, and for grazing angles greater than about 10°, it is well known that the clutter amplitude is Rayleigh-distributed. Moreover, the temporal decorrelation period of the returns is fairly short, of the order of 10 ms, and if frequency agility is implemented (the radar frequency is changed from pulse to pulse by at least the transmitted pulse bandwidth) the returns are fully decorrelated from pulse to pulse. As the radar resolution increases, and for smaller grazing angles, the clutter amplitude distribution develops a longer "tail" and the returns become more "spiky". The temporal and spatial characteristics also change. Clutter spikes having decorrelation periods of several seconds or more are observed, and the returns are no longer fully decorrelated from pulse to pulse by frequency agility. This latter phenomenon is due to the mean sea surface structure which is no longer "smeared" (averaged) out by a low radar resolution.

The overall behaviour can be well modelled by two components. The first is an underlying mean level (the mean sea surface structure), which has a long temporal decorrelation period (order of several seconds), not affected by frequency agility. It characterizes, for example, the mean level variation of clutter spikes or the periodic variation in signal amplitude, seen when looking up or down a sea swell. The second component is termed the "speckle" component, due purely to the resonant scattering by the sea ripples [126]. This is always Rayleigh distributed, indicating a large number of scatterers in the resolution cell. The mean level of the speckle component is determined by the first component. The radar return due to the former, has a fairly short decorrelation period (typically 10 ms) and is fully decorrelated pulse to pulse by frequency agility.

Averaging the speckle component (amplitude) over all possible values of the local mean level, we obtain:

$$p(x) = \int_0^\infty p(y)p(x|y)dy$$

where $p(x)$ is the overall probability density function (PDF) of the clutter amplitude returns, $p(y)$ is the PDF of the clutter mean level and $p(x|y)$ is the PDF of the speckle component. It has been found that $p(y)$ is a good fit to the $\chi_{2\nu}$ family of distributions, so that

$$p(y) = \frac{2b}{\Gamma(\nu)}(by)^{2\nu-1}\exp(-b^2y^2)$$

where b is a scale parameter and ν is a shape parameter. The speckle component is Rayleigh-distributed with mean value y, so that

$$p(x|y) = \frac{\pi x}{2y^2}\exp\left(-\frac{\pi x^2}{4y^2}\right)$$

The overall PDF $p(x)$ becomes then

$$p(x) = \frac{4c}{\Gamma(\nu)}(cx)^\nu K_{\nu-1}(2cx)$$

where $c = b\sqrt{\pi/4}$ and ν are the scale and shape parameters respectively, of the K distribution, which takes its name from the modified Bessel function of the second kind K. There are two main reasons for its popularity:

1. There is some physical underlying basis for such a model, and more important,
2. the K distribution is general enough that it can cover the two extremes of the other currently accepted ad-hoc models[1], lognormal (for $\nu \to 0$), where it can become very long-tailed and spiky, and Rayleigh (for $\nu \to \infty$).

Appendix A outlines a possible scheme for generating K distributed pseudorandom numbers, together with a method for estimating the shape and scale parameters from a given set of data.

2.6 Signal Model

For an isolated point target of cross-section σ, the power available to a matched load at the receiver of a general bistatic radar system is given by the radar equation

$$P_r = \frac{P_t G_t G_r \lambda^2 \sigma}{(4\pi)^3 R_t^2 R_r^2}$$

where P_t, P_r are the transmitter/receiver power respectively, G_t, G_r the transmitter/receiver antenna power gain in the direction of transmission/reception, respectively, σ, is the radar scattering cross-section of the point target, R_t, the distance between transmitter and target, R_r, the corresponding distance between target and receiver and finally, λ is the wavelength of the propagating EM wave.

The generalization to extended targets is easily done by introducing the concept of an *average radar scattering cross-section per unit area*, σ^o, also known as the scattering coefficient. An extended area target is then viewed as being composed of a collection of statistically identical targets, of differential size, with radar scattering cross-section $d\sigma = \sigma^o dA$. The radar equation becomes then

$$dP_r = \frac{P_t G_t G_r \lambda^2 \sigma^o}{(4\pi)^3 R_t^2 R_r^2} dA$$

and the total average received power can be obtained by integrating over the *illuminated area*, A_o

$$P_r = \int_{A_o} \frac{P_t G_t G_r \lambda^2 \sigma^o}{(4\pi)^3 R_t^2 R_r^2} dA$$

In general, σ^o is a function of system parameters (frequency, polarization and aspect angle) and target parameters (surface roughness and dielectric properties). To show the polarization dependence explicitly, we can attach subscripts to σ^o making it σ^o_{pq}. The convention used is that the first subscript refers to the received polarization and the second to the transmitted. Any theoretical study of the interaction between electromagnetic waves and an extended target must deal with the derivation of formulas for σ^o_{pq}. The connection with the theories of EM scattering from a rough surface, is through[130, page 933]

$$\sigma^o_{pq} = \frac{4\pi R^2 < |\mathbf{E}^s_{pq}|^2 >}{A_o |E_0|^2}$$

[1]For $\nu = 0.5$ it is also equal to the Weibull distribution.

where R is the distance from the point of observation to the centre of the illuminated area A_o and E_0 is the magnitude of the incident EM wave (assumed to be plane).

In Appendix B the details are given on how one can proceed from this point on, to the theoretical formulation of the wavenumber spectrum, appropriate for a linear array receiver

$$S(\kappa) = \delta(\kappa - \kappa_T) + |\tilde{\rho}|^2 \delta(\kappa - \kappa_S) + \sigma_n^2 + S_D(\kappa_D)$$

where

$$\kappa = \frac{d_e}{\lambda} \sin\theta$$

is related to the projected wavenumber to the array axis, with d_e the array interelement spacing, λ the EM wavelength and θ the direction of arrival of an incoming plane wave. The subscripts T, S and D refer to the target(direct), specular and diffuse components respectively and the diffuse component of the spectrum is given by

$$S_D(\kappa_D) = \frac{R^2}{4\pi G_t(\theta^t, \phi^t) G_r(\theta^t, \phi^t)} \int_{\phi=0}^{\pi} \frac{G_t(\theta, \phi) G_r(\theta, \phi)}{R_t^2} \sigma^o(\mathbf{k}_i, \mathbf{k}_s) \left| \frac{\sin\alpha}{1 - \cos\alpha(1 + h_R/R_E)} \right| d\phi$$

where ϕ, θ are the azimuth and elevation angles respectively. The superscript t refers to the target/transmitter. For complete generality, a spherical earth model is assumed, with R_E the earth radius, h_R the receiver height and α the angle, from the centre of the earth, to the scattering point under consideration on the earth's surface. Finally, κ_D corresponds to all the possible diffuse component directions of arrival (i.e. the angles θ that result in a non-zero integrand). The total diffuse power is given by

$$P_D = \int_{-\pi/2}^{\theta_{max}} S_D(\kappa_D) d\theta$$

where $\theta = -\pi/2$ corresponds to the receiver base and $\theta = \theta_{max}$ to the transmitter base or horizon.

2.7 Summary

This chapter discussed some of the theoretical background, required, for the understanding of the physics involved, in EM scattering, from the rough sea surface. A literature survey gives a "flavour" and "glimpse" into the research being done in this area. Practical aspects on the difficulties in evaluating the vector scattering integral are pointed out and the new approach of the K distribution is briefly outlined. Finally, the appropriate signal model for the experimental environment in this thesis is described.

Chapter 3

Experimental set-up and tools

The goal of this thesis is to investigate the diffuse multipath structure at low grazing angles. The previous chapter provided some background information towards an understanding of the physics involved. In this chapter, the actual experimental set-up is described (section 3.1) and Thomson's powerful multiple-window-method is outlined (sections 3.2 – 3.3). The latter is the major signal processing tool used in this investigation, both for 2nd and 3rd order statistics (power spectra and bispectra).

3.1 Experimental set-up

The experimental data collection was performed at a site on the mouth of Dorcas Bay, which opens onto the eastern end of Lake Huron on the west coast of the Bruce Peninsula, close to Tobermory, Ontario, in late October – early November of 1987. This particular location was chosen because of the high sea states normally encountered there, which are caused by a combination of westerly winds, the shallow water offshore[1] and the long fetch across Lake Huron. The transmitter was situated at a distance $L = 4.61$ km from the receiver, both being within 10 m of the water's edge. Fig. 3.1 shows the path profile. The receiver was secured at the top of a tower and its centre was at a height h_R above the water's edge while that of the transmitter was at h_T (adjustable).

The transmitter consists of two antenna horns, one above the other, the top one being set for horizontal (H) and the bottom one for vertical (V) polarizations, respectively. Each horn was also capable of transmitting at different frequencies in order to implement frequency agility. For the latter, two different frequency signals were transmitted simultaneously. One of them was always at the fixed frequency of 10.2 GHz, while the other's frequency was varied from 8.02 – 12.34 GHz with a 30 MHz step size according to the formula: $8.02 + 0.03p$ GHz. The picket number p controlled the frequency step size in the agile channel.

[1] The greatest depth along the transmission path was 12 m

Table 3.1: Specifications of MARS, used in the Lake Huron Experiments

Transmitter
- 100 mW CW into one or two 22 dB horns
- simultaneous dual frequencies
- option of dual polarization (H) or (V)
- adjustable transmitter height h_T

Antenna Array
- 32 element linear array vertically oriented
- array aperture 1.82 m, inter-element spacing 5.715 cm
- array machined to $\pm$ 0.1 mm tolerance
- multi-frequency capability 8.02 – 12.34 GHz with 30 MHz steps

Receiver elements
- 2 receiving channels per array element
- 10 dB horizontally polarized horns as array elements
- $\sim$ 25 dB nominal cross polarization rejection ratio
- coherent demodulation with nominal frequency stability to 10^{-12} over a few seconds
- 0.1 Hz Doppler resolution
- 1 Hz – 2 kHz sampling rate capability

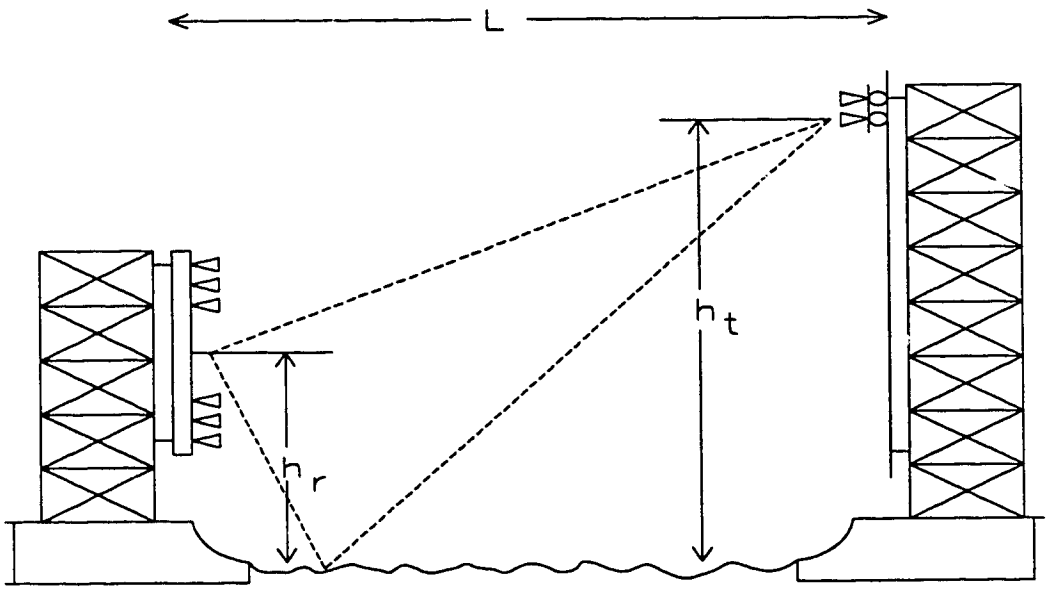

Figure 3.1: The path profile of the lake Huron experiment. The transmitter tower is at the right and the receiver array tower at the left.

The available options for the transmitted signal were therefore:

- When a horizontally polarized signal was desired, the top H horn would transmit the mixture of the fixed and agile frequency signals while the bottom V horn was idle.
- For an H and V dual-polarized signal, the H horn would transmit the agile and the V horn the fixed frequency signals.
- Finally, for a vertically polarized signal, the top H horn remained idle while the bottom V horn transmitted the mixture of fixed and agile frequency signals.

The microwave source was produced by phase locking to a highly stable 5 MHz crystal oscillator operating at a constant temperature. A travelling wave tube amplifier (TWTA) with a maximum gain of 40 dB was then used to amplify the source signal before feeding it to the transmitter horns. System control at the transmitter was achieved with a PC-XT microcomputer that adjusted transmission frequency, TWTA gain and carriage height.

The receiver is a 32-element linear array designed and built by a group led by V. Kezys and E. Vertatschitsch at the Communications Research Laboratory (CRL) of McMaster University and forms the main part of MARS, a Multi-parameter Adaptive Radar System. It is a coherent, sampled aperture, linear receiver array, vertically oriented, composed of 32 pairs of horizontally polarized standard gain horn antennas. Each pair of horns corresponds to a single array element and offers the opportunity to always implement frequency agility and when desired, by choosing one of the options for the polarization of the transmitted signal, polarization diversity, HH or HV.

The RF and IF local oscillators and the RF testing signal generator were shared by all the receiver elements. Since coherent reception is implemented, each receiver horn is followed by a quadrature demodulator block so that phase information can be extracted.

System control at the receiver is provided with a PC-AT microcomputer that offers a completely automated data collection environment. For each trial, only the parameters defining the desired physical conditions need to be fed into the computer. The computer accordingly adjusted the frequency of the RF oscillator for the agile channels, the IF amplifier gains, the bandwidth of the low-pass filters in the I and Q channels and the sampling rate of the samplers. It also sent commands via a radio link to the transmitter computer that controlled the transmission operation. Most of the data were sampled with a 62.5 Hz sampling rate, corresponding to 8 sample points per cycle at the baseband frequency. They were then digitized by A/D converters with 12-bit precision and stored onto hard disk for off-line processing.

The data were divided into three groups with respect to polarization: like-polarized, dual-polarized and cross-polarized. The first four characters in their name refers to the collection date, e.g. *nov3*. The next two characters define the group they belong to; *dh* for the like-polarized group where both transmission and reception are H-polarized; *dd* for the dual-polarized group where both polarizations are transmitted; *dv* for the cross-polarized group where only a cross polarized signal is

received; A fourth group of data for the purpose of aperture calibration was also collected and the dataset designation is *cff*.

The numeral following the above designations is simply a dataset index providing order among similar datasets collected within the same day. It is followed by the data subset number. As an example, *nov3:dd1;2* stands for the second subset of a dual polarized dataset, collected on November 3, being the first dataset in this group collected on that particular day. We normally have 127 snapshots per data subset (offering us about 2 sec worth of data) and 16 subsets per dataset.

The data are carefully calibrated, both in phase and quadrature (IQ calibration) using known injected tone signals, and in aperture (aperture calibration) using a far-field technique. The details are given in a CRL technical report [37]). The tone-estimation capability of Thomson's MWM in the presence of an unknown noise background is successfully used there as well.

In our experimental data investigation we examine the diffuse multipath component at a variety of frequencies and grazing angles. For the latter, a nominal value of the angular separation between the direct and specular components can be estimated, using the known transmitter and receiver heights and a spherical or flat earth model (the difference between the two models is negligible for such a short path length).

3.2 Thomson's multiple-window-method

In examining the second order statistics (i.e. power spectra in both wavenumber and frequency domain) a non-parametric estimation method of the best possible resolution was desired. The non-parametric aspect would not introduce any subjective structure or biases about the underlying diffuse multipath while the resolution aspect could handle the case of two line components, at sub-beamwidth separation, in an unknown coloured noise background.

Such a method was developed by Thomson [120], [122] and [123]. It involves the use of the discrete prolate spheroidal sequences as data windows. The original data sequence (in time or space) is individually windowed with each of the above windows (the number depending on the time-bandwidth product of the process under investigation), thus generating a number of multiple, windowed data sequences. Their Fourier transforms (performed with FFT's), called eigencoefficients, can be viewed as the expansion coefficients of the original data sequence on the prolate basis. These eigencoefficients can be used in a data adaptive manner to perform spectrum and line component estimation among other things [124].

An outline of the method follows. Further implementation details, together with examples are given in Drosopoulos and Haykin [39].

MWM outline

Assume that we have a finite dataset of N contiguous samples, $x(0), x(1), \ldots, x(N-1)$, which are observations from a stationary, complex, ergodic, zero-mean, Gaussian process. The discrete-time

spectral representation of the data sequence $\{x(n)\}$ is given by the Cramèr representation

$$x(n) = \int_{-1/2}^{1/2} e^{j2\pi fn} dZ(f) \tag{3.1}$$

where $dZ(f)$ is the orthogonal increment of the underlying stochastic process that our observations $\{x(n)\}$ come from. The second order statistics, i.e. power spectrum $S(f)$ is defined from

$$\mathsf{E}\{dZ(f)\} = 0, \qquad S(f)df = \mathsf{E}\{|dZ(f)|^2\}$$

By taking the Fourier transform of the data

$$\tilde{x}(f) = \sum_{n=0}^{N-1} x(n) e^{-j2\pi fn}$$

and substituting the Cramèr representation for $x(n)$ we obtain the *fundamental equation of spectrum estimation*

$$\tilde{x}(f) = \int_{-1/2}^{1/2} \mathsf{D}_N(d-\nu) dZ(\nu) \tag{3.2}$$

where the kernel is recognized as the Dirichlet kernel

$$\mathsf{D}_N(f) = \sum_{n=0}^{N-1} e^{-j2\pi fn} = \exp[-j\pi f(N-1)] \frac{\sin N\pi f}{\sin \pi f}$$

In order to get the best possible estimate of $\tilde{x}(f)$ from our finite data sample and (3.2) we first need to perform an eigendecomposition of the Dirichlet kernel.

Slepian [112] has already done this and for the discrete data case all that is needed is to perform the eigendecomposition of the following Toeplitz system

$$\sum_{m=0}^{N-1} \frac{\sin 2\pi W(n-m)}{\pi(n-m)} v_m^{(k)}(N,W) = \lambda_k(N,W) v_n^{(k)}(N,W)$$

In matrix form, the above eigenvalue equation is written as

$$\mathbf{T}(N,W)\mathbf{v}_{(k)}(N,W) = \lambda_k(N,W)\mathbf{v}_{(k)}(N,W)$$

where

$$\mathbf{T}(N,W)_{mn} = \begin{cases} \sin[2\pi W(m-n)]/[\pi(m-n)] & ; m,n = 0,1,\ldots N-1 \text{ and } m \neq n \\ 2W & ; \text{for } m = n \end{cases}$$

The eigenvectors $v_n^{(k)}(N,W)$ are the discrete prolate spheroidal sequences (DPSS's) or Slepian sequences in honour of Dave Slepian who first studied their properties. These are the data windows that are used in MWM. W is the analysis window (in normalized units $0 < W < 0.5$) related to the time-bandwidth product NW of the process $\{x(n)\}$. The eigenvalues $\lambda_k(N,W)$ are

a measure of how much signal energy is concentrated in W. Only the first $K \approx 2NW$ Slepian sequences, which all have $\lambda_k(N,W) \approx 1$ need be used. It is then that we have the best possible spectrum estimator that optimizes the bias/variance trade-off that is usually the problem in spectrum estimation from a finite data sample.

Both Thomson [120] and Slepian [110], [111], [112], [113] give asymptotic expressions for the computation of the Slepian sequences; it is probably the complexity of these expressions that initially discourages people from using the prolate basis. If, however, only the eigenvectors are required, Slepian [112] notes that the DPSS's satisfy a Sturm-Liouville differential equation leading to

$$\mathbf{S}(N,W)\mathbf{v}_{(k)}(N,W) = \theta_k(N,W)\mathbf{v}_{(k)}(N,W)$$

The matrix S is tridiagonal in the sense that

$$\mathbf{S}(N,W)_{ij} = \begin{cases} \frac{1}{2}i(N-i) & ; j = i-1 \\ (\frac{N-1}{2} - i)^2 \cos 2\pi W & ; j = i \\ \frac{1}{2}(i+1)(N-1-i) & ; j = i+1 \\ 0 & ; \text{otherwise} \end{cases}$$

Even though the eigenvalues θ_k are not equal to λ_k, they are ordered in the same way and the eigenvectors are the same. Tridiagonal systems are easier than Toeplitz to solve, and this offers a good practical way of numerically computing the eigenvectors. The single EISPACK routine IMTQL2 is sufficient if one desires all eigenvectors. Since, however, only a small number of eigenvalues and eigenvectors is actually needed, the combination RATQR and TINVIT is less wasteful of computer time. Given the eigenvectors, the eigenvalues can then be found[2] from

$$\lambda_k(N,W) = [\mathbf{v}_{(k)}(N,W)]^T \mathbf{T}(N,W)\mathbf{v}_{(k)}(N,W)$$

The Fourier transform of Slepian's DPSS's gives us the discrete prolate spheroidal functions or Slepian functions

$$V_k(f) = \sum_{n=0}^{N-1} v_n^{(k)}(N,W)e^{-j2\pi fn}$$

We can now solve (3.2) by expanding its factors in $(f-W, f+W)$ using the Slepian basis. From Mercer's theorem, the kernel expansion is

$$\mathrm{D}_N(f-\nu) = \sum_{k=0}^{\infty} \lambda_k V_k(f) V_k^*(\nu)$$

[2]Thomson[122] uses BISECT and TINVIT to evaluate the Slepian sequences, and

$$\lambda_k(N,W) = \int_{-W}^{W} |V_k(f)|^2 df \Big/ \int_{-1/2}^{1/2} |V_k(f)|^2 df$$

for the eigenvalues.

and the orthogonal increment process is

$$dZ(f-\nu) = \sum_{k=0}^{\infty} x_k(f) V_k^*(\nu) d\nu$$

Using orthogonality properties the coefficients of the orthogonal process are given by

$$x_k(f) = \sum_{n=0}^{N-1} x(n) v_n^{(k)}(N,W) e^{-j2\pi fn}$$

We call the $\{x_k(f)\}$ the *eigencoefficients* of the sample. Since they are computed by transforming the data multiplied by the kth data window $v_n^{(k)}(N,W)$, their absolute squares

$$\hat{S}_k(f) = |x_k(f)|^2$$

are individually direct spectrum estimates and we call them *eigenspectra.*

The adaptive spectrum

While the lower order eigenspectra have excellent bias properties there is some degradation as k increases toward $2NW$. In his 1982 paper [120], Thomson introduces a set of weights $\{d_k(f)\}$ that downweight the higher order eigenspectra so that $S(f)$ can be estimated as

$$\hat{S}(f) = \frac{\sum_{k=0}^{K-1} |d_k(f)|^2 \hat{S}_k(f)}{\sum_{k=0}^{K-1} |d_k(f)|^2}$$

leading to the iterative expression

$$\hat{S}^{(i+1)}(f) = \left[\sum_{k=0}^{K-1} \frac{\lambda_k \hat{S}_k^{(i)}(f)}{[\lambda_k \hat{S}^{(i)}(f) + \hat{B}_k(f)]^2}\right] \left[\sum_{k=0}^{K-1} \frac{\lambda_k}{[\lambda_k \hat{S}^{(i)}(f) + \hat{B}_k(f)]^2}\right]^{-1}$$

As starting value for $\hat{S}(f)$ we can take the average of the two lowest order eigenspectra and a fair estimate of the expected value of the broadband bias $\mathsf{E}\{B_k(f)\}$, $\hat{B}_k(f)$, is given by

$$\hat{B}_k(f) = \mathsf{E}\{B_k(f)\} = (1-\lambda_k)\sigma^2$$

where the process variance is estimated as

$$\sigma^2 = \int_{-1/2}^{1/2} S(f) df = \mathsf{E}\{|x(n)|^2\} \approx \frac{1}{N} \sum_{n=0}^{N-1} |x(n)|^2$$

Convergence is rapid with successive spectrum estimates differing by less than 5% in 5–20 iterations. If desired, a more accurate (also more complex) estimation of $B_k(f)$ is possible ([120, 39]).

Line component estimation

The sample eigencoefficients can also be used to estimate line components in the spectrum. An F-test statistic can be set up, at each frequency point f_i (scanning the normalized frequencies from -0.5 to 0.5) to determine which of the following two hypotheses is true:

H_0: there is no line component at $f_i - W < f < f_i + W$

$$\mathsf{E}\{x_k(f)\} = 0$$

H_1: there are one or more line components at $f_i - W < f < f_i + W$

$$\mathsf{E}\{x_k(f)\} = \sum_i \mu_i V_k(f - f_i)$$

where μ_i is the complex amplitude of the ith line component. Two variants of a linear regression problem can now be set up:

Point regression

$$\min_{\mu_i} \left\{ \sum_{k=0}^{K-1} \left| x_k(f) - \sum_i \mu_i V_k(f - f_i) \right|^2 \right\}$$

and integral regression

$$\min_{\mu_i} \left\{ \sum_{k=0}^{K-1} \int_{f_i - W}^{f_i + W} \left| x_k(f) - \sum_i \mu_i V_k(f - f_i) \right|^2 df \right\}$$

The summation over i takes into account a possible multiplicity of lines within the analysis window W. In our experience it is integral regression, that is more robust due to the averaging effects of integration. Note also that a multiple-line F-test can be somewhat complicated to set up.

Coherencies and transfer functions

The next step after investigating the properties of a single data sequence is to compare two sequences, say $\{x\}$ and $\{y\}$, collected under similar or different conditions (frequency or polarization in our case) and see whether there is any similarity between them.

Coherency is the complex quantity

$$\tilde{\gamma}(f) = \frac{S_{xy}(f)}{\sqrt{S_{xx}(f) S_{yy}(F)}}$$

in essence, the cross-correlation in the frequency domain (for time domain sequences), while the *transfer function* shows how one can transform the "input" sequence $\{x\}$ to the "output" sequence $\{y\}$ through

$$Y(f) = H(f)X(f)$$

The advantage of working in the frequency domain lies in the fact that Fourier transformed data, of even moderately long-tailed distributions, tend to be Gaussian as the length of the data sequence increases (central limit theorem). This is useful in obtaining estimates, as their bias/variance properties are then more easily controlled.

MWM offers a robust approach (Chave et.al. [26]) of estimating coherencies and transfer functions that can handle data outliers like point defects and local nonstationarity. Point defects are isolated outliers that exist independent of the structure of the process under study. Typical examples include dropped bits in digital data, transient instrument failures, and spike noise due to natural phenomena. Local nonstationarity means a departure, of finite duration, from the underlying stationary base state.

The $K \approx 2NW$ sample eigencoefficients $\{x_k(f)\}$ and $\{y_k(f)\}$ are used to set up

$$\tilde{c}(f) = \frac{\sum_{k=0}^{K-1} x_k(f) y_k^*(f)}{\sqrt{\sum_{k=0}^{K-1} |x_k(f)|^2 \sum_{k=0}^{K-1} |y_k(f)|^2}}$$

as the basis for an estimate of $\tilde{\gamma}(f)$, and

$$y_k(f) = \sum_{k=0}^{K-1} h(f) x_k(f)$$

as the basis for an estimate of $H(f)$.

Chave et.al. [26] and Thomson and Chave [124] give details on how to robustify the above estimates as well as how to include jackknifed error bounds.

3.3 Bispectrum estimation

The assumptions that are commonly made in time series analysis are:

1. the process under investigation is stationary, and
2. it can be described by a linear model.

Up to this point, we have also assumed that diffuse multipath is a Gaussian stochastic process. Second order stationarity implies then full stationarity since moments higher than two are zero. Also, Gaussian processes are linear, with a large body of theoretical and applied work already available.

The stochastic signal in the receiver that describes clutter and/or diffuse multipath is non-stationary and non-linear, in general, for large enough intervals of time and high enough sea state conditions. Assuming that the time interval of data collection for a single dataset is short enough (2 sec) for stationarity to hold, an estimate of the process bispectrum can immediately show whether Gaussianity holds. If the process is found to be non-Gaussian, then it is possible that it might also be non-linear. (A Gaussian process is linear, but a non-Gaussian process is not necessarily non-linear).

One of the early references on the bispectrum (the first member in the family of polyspectra or higher-order spectra) was Brillinger's, in 1965 [21]. He ends on a pessimistic note, since higher order moments require a much larger data sample in order to be efficiently estimated with the same accuracy as the second order statistics. Later on, Nikias and Mendel introduced the bispectrum to the Digital Signal Processing community (see the tutorial papers by Nikias and Raghuveer [94], Mendel [83], and also the monograph of Gabr and Rao [106] for a good introduction). A more efficient estimator was developed based on the ARMA model (details in [105]) opening the way to a wider use of the bispectrum in the large class of signal processing problems where the ARMA model is applicable.

Higher order statistics have the potential to extract more information about the underlying non-linear structure of a process and given the availability of estimation tools, a strong motivation exists to apply them to real data, as part of a thorough signal processing analysis. The bispectrum is a complex valued, 2-dim, frequency domain expansion of the third moments of a process. As such, a non-zero bispectrum magnitude at some pair of frequencies (f_1, f_2), indicates a non-linear phase coupling of all the harmonic component pairs, whose individual frequencies are f_1 and f_2 respectively. Phase information that the 2nd order spectrum suppresses, is now made available.

For a stationary, discrete-time, 1-dim process, with unit sampling time, the Cramér spectral representation is

$$x(t) = \int_{-1/2}^{1/2} e^{j2\pi ft} dX(f)$$

and the bispectrum $B(f_1, f_2)$ is defined as

$$\mathsf{E}\{dX(f_1)dX(f_2)dX(f_3)\} = \begin{cases} B(f_1, f_2)df_1 df_2 & \text{for } (f_1 + f_2 + f_3) \bmod 1 = 0 \\ 0 & \text{otherwise} \end{cases}$$

One can also use the third order moments

$$B(f_1, f_2) = \sum_{\tau_1=-\infty}^{\infty} \sum_{\tau_2=-\infty}^{\infty} \mathsf{E}\{x(t)x(t+\tau_1)x(t+\tau_2)\} e^{-j2\pi(f_1\tau_1 + f_2\tau_2)}$$

or [10]

$$B(f_1, f_2) = \tilde{X}(f_1)\tilde{X}(f_2)\tilde{X}(-f_1 - f_2)$$

where $\tilde{X}(f)$ is the Fourier transform of $x(t)$. The latter expression makes extraction of the symmetry relations

$$B(f_1, f_2) = B(f_2, f_1) \tag{3.3}$$

$$B(f_1, f_2) = B(f_1, -f_1 - f_2) \tag{3.4}$$

$$B(f_1, f_2) = B^*(-f_1, -f_2) \tag{3.5}$$

simpler. Note that relation (3.5) holds only for real processes $x(t)$ leading to 12 symmetry regions in the 2-dim frequency plain. For complex processes when it does not hold, the symmetry is only sixfold

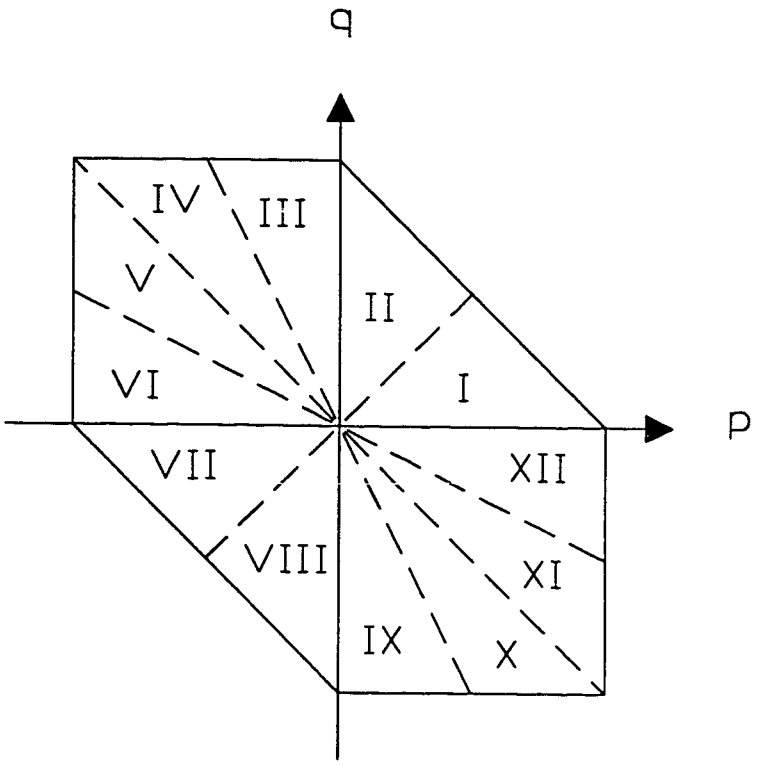

Figure 3.2: The hexagonal support of the bispectrum of a bandlimited signal and its symmetry relations. For a real signal the bispectrum is completely determined by a single octant, e.g., region I, all other octants being determined from the symmetry relations. For a complex signal, two point-symmetric octants are required, e.g., I and VII.

(see Fig. 3.2 which shows the hexagonal region of support for the bispectrum and the symmetries involved for both real and complex processes).

Nikias and Raghuveer [94] describe the conventional non-parametric approach for estimating the bispectrum. The third-order moment sequence is first estimated and then a properly windowed 2-dim Fourier transform is taken. In [121] [3] Thomson uses MWM, to obtain:

$$\hat{B}(f_1, f_2) = \frac{1}{\gamma} \sum_{j,k,l=0}^{K-1} \hat{x}_j(f_1)\hat{x}_k(f_2)\hat{x}_l(f_3)P(j,k,l)$$

where

$$P(j,k,l) = \sum_{n=0}^{N-1} v_n^{(j)}(N,W)v_n^{(k)}(N,W)v_n^{(l)}(N,W)$$

with $v_n^{(j)}(N,W)$ an element of one of the Slepian sequences,

$$\gamma = \sum_{j,k,l=0}^{K-1} \hat{P}^2(j,k,l)$$

a normalization constant, and $\hat{x}_k(f)$ the sample eigencoefficients defined earlier in this chapter, adaptively weighted with $d_k(f)$. Averaging of n_S ensembles is done through

$$\hat{B}(f_1, f_2) = \frac{1}{n_S} \sum_{i=1}^{n_S} \hat{B}_i(f_1, f_2)$$

where $\hat{B}_i(f_1, f_2)$ is the bispectrum estimate from each ensemble.

3.4 Summary

The experimental set-up, used in the data collection of the database investigated in this thesis, is briefly described. An outline of Thomson's MWM is also given, showing some of the possibilities in extracting 2nd and 3rd order information from the database. Note that MWM is still is a state of development [122] so there is still room for improvement.

[3] These Proceedings cover a great many applications of higher order spectral analysis showing many possible uses.

Chapter 4

Experimental Data Investigation

The core of the thesis work is presented in this chapter, where the signal processing investigation tools already described, are finally applied to the experimental database. The first step (section 4.1) is to estimate and extract the direct and specular components (AOA estimation). The filtered, residual process, contains then the desirable diffuse multipath component together with the ubiquitous receiver noise (assumed to be white). The power spectra (both wavenumber and frequency domain) of diffuse multipath can then be estimated (section 4.2). This is the first time that the wavenumber spectrum, of a low-grazing angle signal, in a background of diffuse multipath, is estimated. A simple quasi-specular scattering model (McGarty's) highlights the importance of shadowing, since only when shadowing is incorporated in the model, do we get even qualitative agreement with the experimental results. Investigation of possible relations between different simultaneous frequencies is then done (section 4.3) through coherency and transfer function estimation. Small coherency between channels implies that different parts of the scattering surface are responsible for each channels's contribution. Looking into the amplitude distribution (1st order statistics), we see (section 4.4) excellent agreement with the K distribution. This implies that a non-linear underlying structure may be present and warrants the use of the bispectrum (section 4.5).

4.1 Angles-of-arrival

The Rcvr is a linear array with 32, uniformly spaced, standard horn antennas as elements. The reception is coherent, leading to a vector snapshot of 32 complex data samples at each instant of time. There usually are 64 or 127 snapshots per dataset. Each of these snapshots may be regarded as a realization of a mixed process, i.e. a process that has lines (direct and specular components) as well as a continuous background component (diffuse multipath). In the wavenumber domain (analogous to the frequency domain for time sampled signals) the line components have the physical meaning of incoming plane waves, impinging on the linear array Rcvr, while the continuous background

Table 4.1: Three experimental datasets, HH polarized, used in the AOA examples. The distance between transmitter and receiver is 4.61 km in all cases.

	dataset	frequency (GHz)	separation (BW)	h_r (m)	h_t (m)
1	*nov9:dh6;7*	9.76	0.247	8.67	9.59
2	*nov9:dh7;6*	10.2	0.118	8.67	4.37
3	*nov9:dd1;2*	10.12	0.483	8.67	18.06

component is the diffusely scattered part of the transmitted signal that reaches the Rcvr.

Since the separation of the two coherently related line components is less than a beamwidth (within the analysis window W), the double-line F-test from Thomson's MWM is used to extract them. This is equivalent to angle-of-arrival (AOA) estimation in the presence of unknown coloured noise. The estimation is normally done on a snapshot-by-snapshot basis to bring up any possible signal non-stationarity. A maximum likelihood (ML) estimator is also implemented, for comparison. ML was chosen because it provides a commonly used frame of reference, against which all modern parametric methods are compared with. To single out the effect, if any, of including diffuse multipath in the AOA estimation process, which MWM implicitly does, the only a priori knowledge that we assume for ML, is that we have two incoming plane waves in a white noise background.

Figures 4.1 – 4.3 show some typical examples from HH polarized data at different frequencies and grazing angles. Table 4.1 displays the pertinent parameters of each individual dataset (see also [39] for other examples and more details on the ML estimator). A flat earth model[1] is used to calculate the expected angular separation between the direct and specular components. This latter quantity (angular separation) provides a better comparison measure between expected and estimated results, since it is unaffected by possible tilts of the Xmtr and Rcvr towers, occurring from wind action (at least in the vertical direction).

The signal ratio $\rho = a_2/a_1$ (magnitude and phase) is computed as well, where a_1 and a_2 are the complex amplitudes (referred to the array center) of the assumed direct and specular components. This ratio is related to the reflection coefficient R of the scattering surface. Ideally, for a smooth, plane, water surface, at 10 GHz, for HH polarization and low grazing angles, the reflection coefficient R should have a magnitude approximately equal to 0.9 and a phase of approximately 180°. For a rough surface, according to the Kirchhoff approximation, the mean magnitude is modified by [16]

$$\exp\left[-\left(\frac{4\pi\sigma_h \sin\psi}{\lambda}\right)^2\right]$$

where ψ is the grazing angle and σ_h is the rough surface height variance.

The magnitude therefore of ρ can be modeled as a function of R, modified by the above roughness correction and possibly, the effects of the earth's curvature can be included by using the

[1] A spherical one was also implemented, the difference being negligible for the short path involved (~ 5 km).

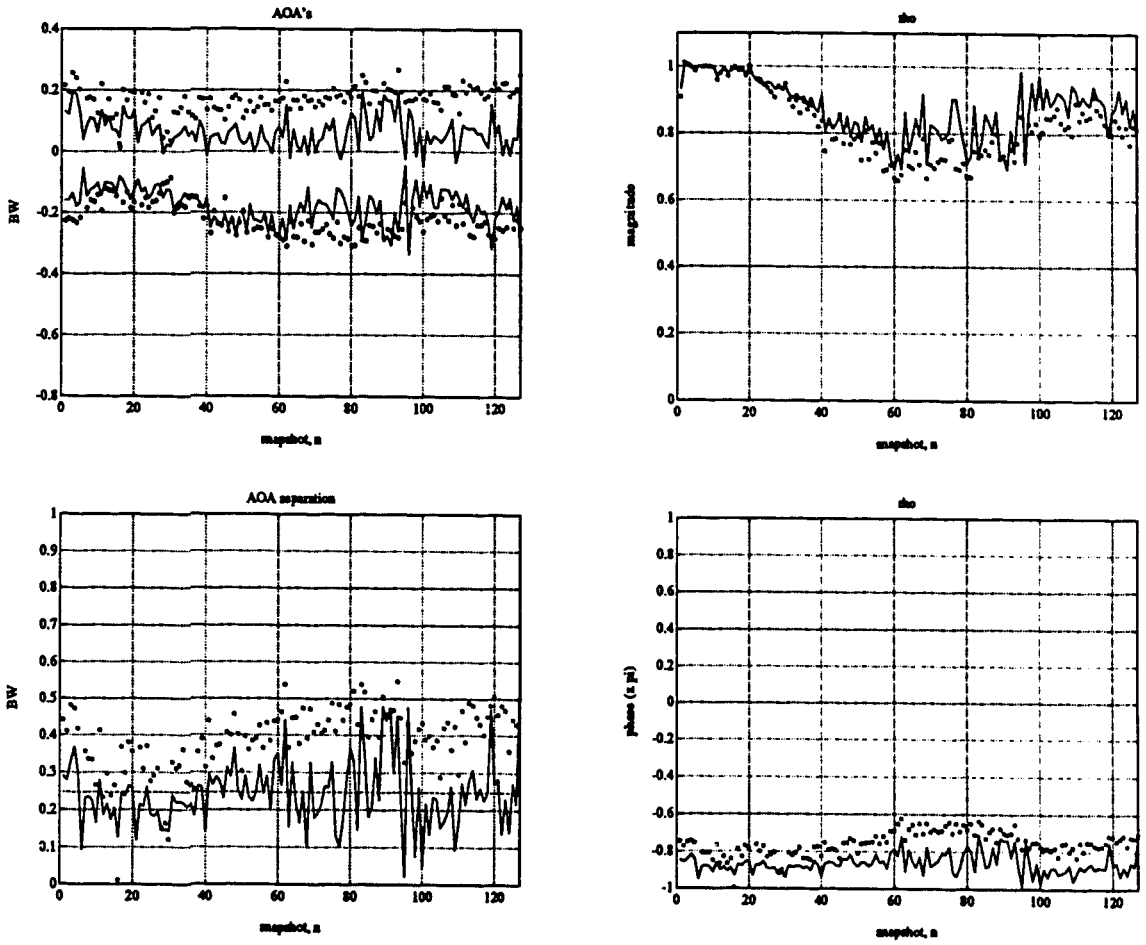

Figure 4.1: Dataset 1, *nov3:dh6;7, f=9.76 GHz*, far-field calibrated by *nov1:cff7;7*. Solid lines correspond to MWM estimates. In the top left graph the direct component is above the specular, and * and o correspond to the ML direct and specular components, respectively. The bottom left graph shows the estimated angular separation between direct and specular components compared with the nominal (dashed line). In the top right graph the magnitude of the specular reflection coefficient ρ is displayed, while in the bottom right it is the phase. The * in both cases corresponds to the ML estimates.

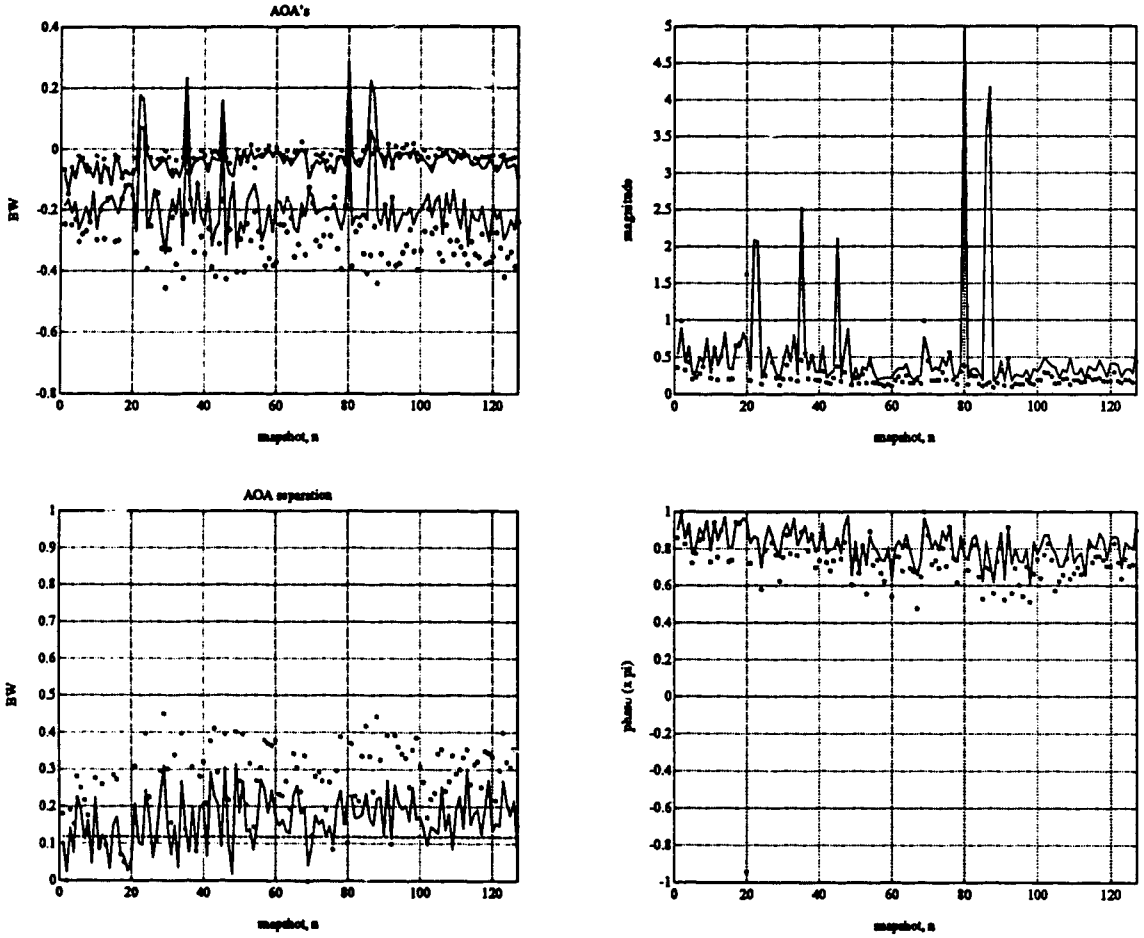

Figure 4.2: Dataset 2, *nov3:dh7;6, f=10.2 GHz*, far-field calibrated by *nov2:cff2;1*. This dataset was collected under the worst high wind conditions and the lowest grazing angle. The ML estimator converged only for 118 snapshots, while MWM converged for all 127. Cases are seen however where even MWM has difficulties.

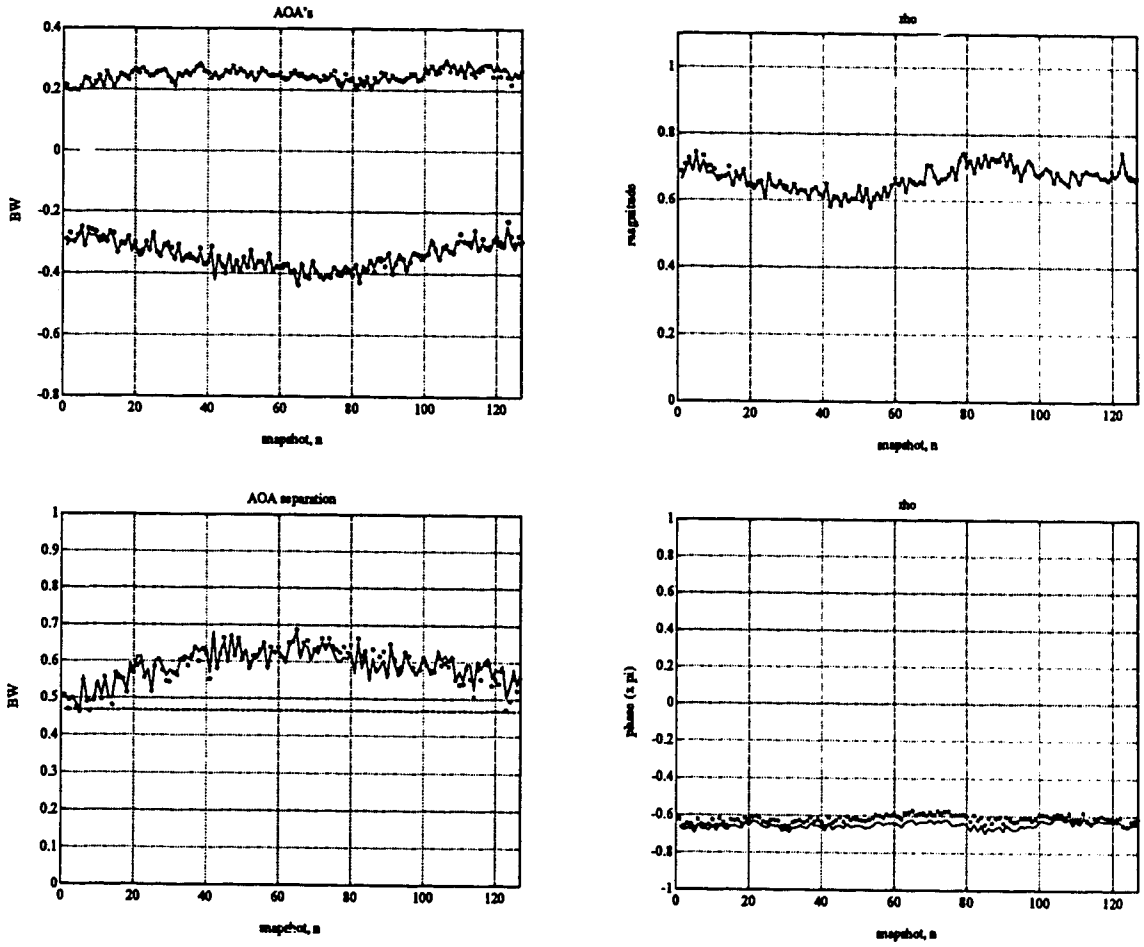

Figure 4.3: Dataset 3, *nov3:dd1;2, f=10.12 GHz*, far-field calibrated by *nov1:cff6;8*. The bias observed in this case seems to have a periodic behaviour. There are two possible explanations. One is that the wave structure at the specular point is visible so that the changing wave height is observed. The other is that the antenna tower is being tilted by the wind, and the periodic variation observed could be caused by the tower swaying away from the vertical, making the actual separation angles larger than nominal.

Table 4.2: The bias (compared to the specular model computed AOA separation from the known system geometry) and variance of the MWM and ML estimators for Figs. 4.1 - 4.6 are given here (BW units are used). The better performance of MWM is clearly evident.

Figure	model separation	ML bias	MWM bias	ML variance	MWM variance
4.1	0.247	0.144	0.003	0.113	0.117
4.2	0.118	0.153	0.034	0.132	0.081
4.3	0.483	0.078	0.080	0.031	0.030
4.4	0.118	0.144	0.005	0.052	0.038
4.5	0.247	0.083	0.081	0.013	0.013
4.6	0.490	0.071	0.013	0.005	0.005

divergence factor. The phase of ρ, on the other hand, includes both the phase of R and the path length difference between the direct and specular paths, which may result in a shift in the observed phase, away from 180°. The quantity ρ, the specular model reflection coefficient, provides a way to check the quality of the data calibration. It happens, occasionally, that some far-field calibration data are collected under drastically different conditions from the actual experimental data, leading consistently to $|\rho| > 1$. As this would imply that the specular component is more powerful than the direct, data calibrated with these tables are rejected. Focusing weather conditions might exist, e.g. waveguiding ducts, where this phenomenon is indeed observed. However, this is not the case here. The more likely explanation for this observation is, that the degree of coherency (when $|\rho| \approx 1$ and $\arg(\rho) \approx 180°$) between the direct and specular components is great enough to almost cancel them out. This can make the estimation/resolution problem particularly difficult, increasing both bias and variance of the AOA estimators. Surface roughness appears then to be "beneficial" for AOA estimation since it may destroy the above mentioned phase opposition conditions.

Note that if the AOA estimator uses more than one snapshot, e.g. a sliding window of 5 snapshots, the results are smoother (Fig. 4.4). The best improvement however, can be achieved, if frequency agility (more snapshots at different carrier frequencies) *and* a priori information is incorporated in the AOA estimator [64, 38, 40]. The a priori information implemented here, consists of knowledge of the Rcvr height above the water surface and the range between Xmtr and Rcvr. A flat-earth specular model is then used to relate the direct and specular AOA's. The result is a single unknown AOA, and a simpler one dimensional optimization problem. More complex models may also be used [73], for even better results, at the expense of a higher computational load. Table 4.2 gives numerical values for bias and variance of the MWM and ML estimators.

Figures 4.5 and 4.6 show two examples of the multiple frequency, a priori information, AOA estimation, at two different grazing angles. Each estimated AOA uses 4 concurrent snapshots, at different frequencies, and the flat earth parametric model mentioned above, to effectively estimate a single AOA, that of the direct component. The improvement for both estimators (MWM and ML),

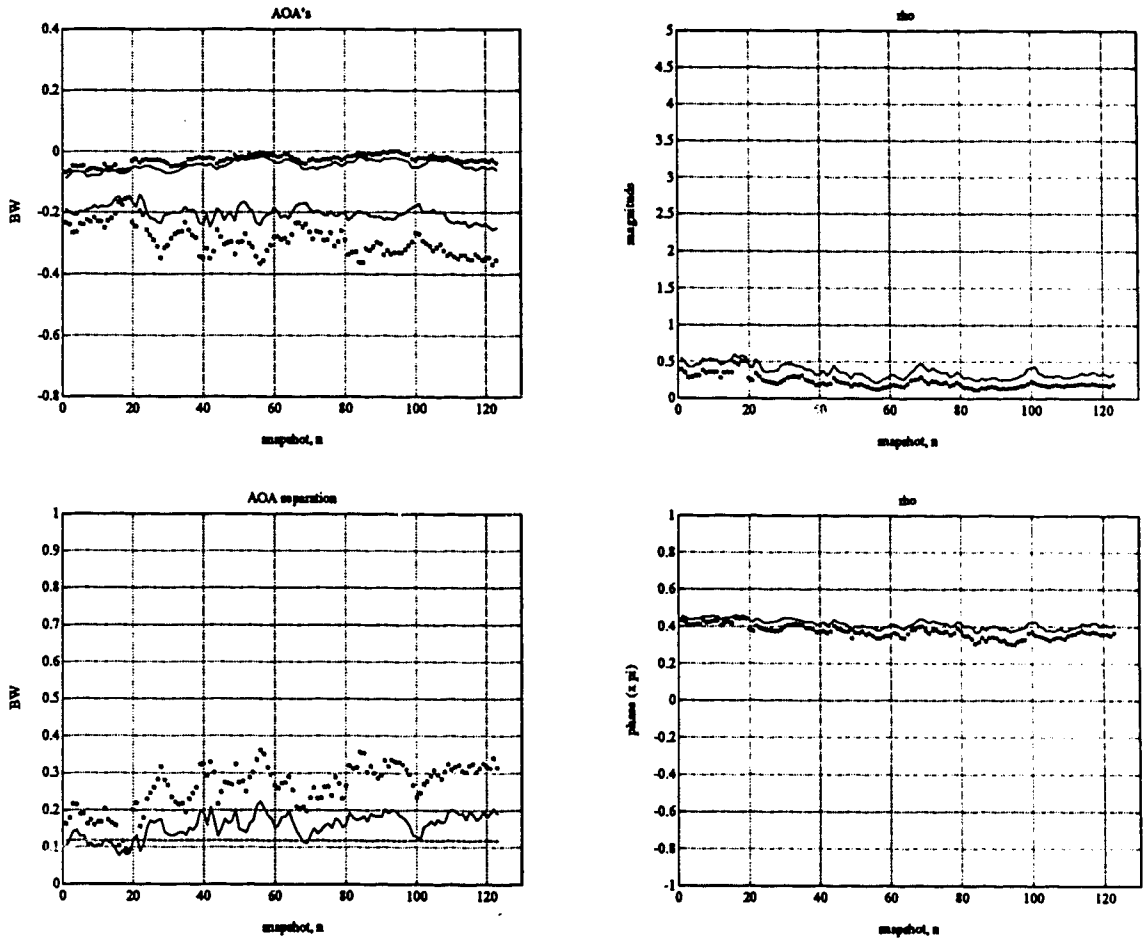

Figure 4.4: Dataset 2, *nov9:dh7;6*, when a sliding window of 5 snapshots is used for both estimators. Note the smoother behaviour. Both estimators converge for all 123 snapshots. The $|\rho| > 1$ cases have disappeared.

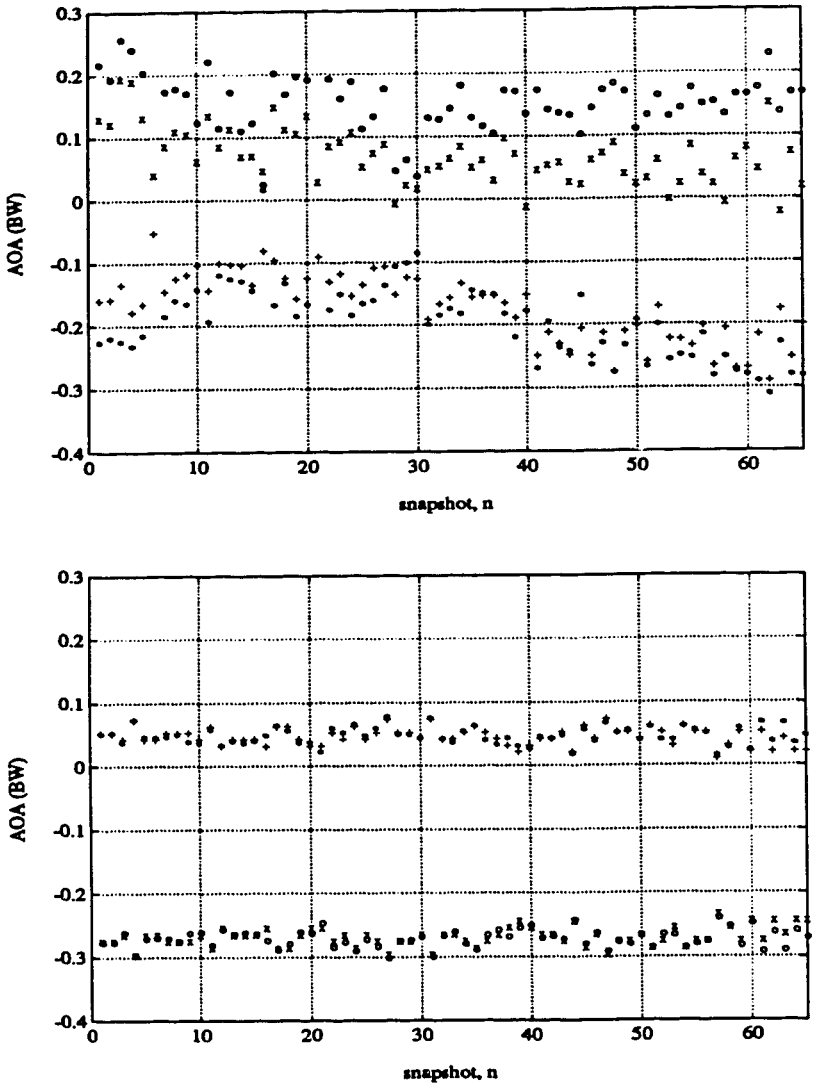

Figure 4.5: A dataset with 0.247 BW nominal separation at 9.76 GHz. (a) 1 frequency, no a priori assumptions, MWM direct and specular component ($\times$ and $+$), maximum likelihood ($\circ$ and $*$). (b) 4 frequencies (8.05, 9.76, 11.5 12.34 GHz), with additional information. MWM direct and specular component ($+$ and $\times$), maximum likelihood ($*$ and $\circ$).

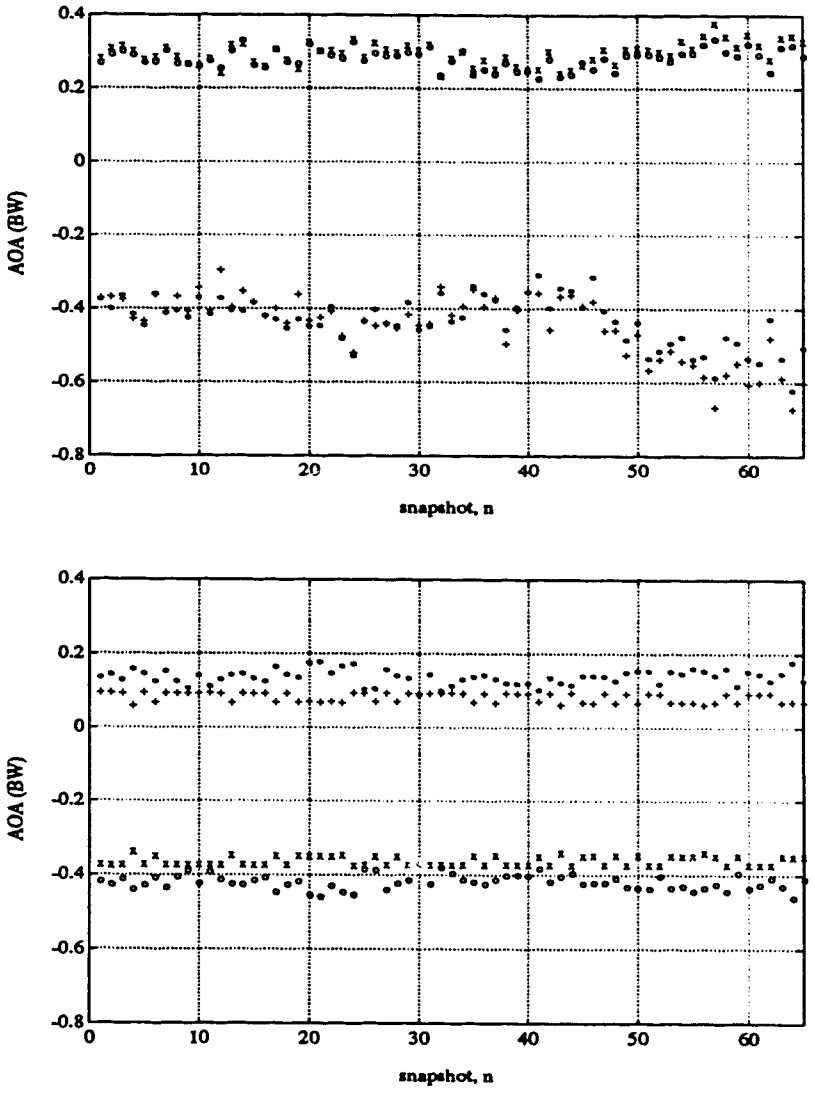

Figure 4.6: A dataset with 0.490 BW nominal separation at 12.34 GHz. (a) 1 frequency, no a priori assumptions, MWM direct and specular component (× and +), maximum likelihood (∘ and ∗). (b) 4 frequencies (9.52, 10.72, 11.92 12.34 GHz), with additional information. MWM direct and specular component (+ and ×), maximum likelihood (∗ and ∘).

regarding bias and variance, is clearly evident.

Based on the results displayed in the figures here, and from other cases as well, we can make the following observations for the like polarized datasets:

- At the higher separations ($\sim$ 0.5 BW) between the two line components, both estimators are in good agreement with each other. Note that when additional information is used (Fig. 4.6) the MWM variance is slightly less than the ML variance, and that the MWM AOA separation is slightly closer to the known separation.
- At the smaller separations ($\sim$ 0.25 BW or less) when the model mismatch occurring as a result of neglecting the diffuse component, is more pronounced, some problems appear with both estimators. Occasionally, when using a single snapshot, both MWM and ML give AOA's with $\rho > 1$, and ML frequently fails to converge altogether. A sliding window of more than one snapshot leads to smoother behaviour, and additional information can certainly improve things.

The overall performance of MWM as an AOA estimator is seen to be better than ML. The latter estimator assumes a white-like background noise throughout the entire wavenumber region while for MWM this holds only within the analysis window W. The ability of MWM to estimate line components in the presence of unknown coloured noise *without* disturbing the noise component, should also be emphasized[2]. Note that the scenario used in these experiments is not particularly complicated. In real life situations, where jamming or other radiating sources exist, MWM has an overwhelming advantage over ML, if the ML model does not use the correct number of sources; MWM is not affected by sources outside the analysis window (robustness to interference). This, together with the fact that one can obtain information about the background noise spectrum in a non-parametric manner, makes MWM an extremely versatile and useful tool in investigating power spectra (among other things).

4.2 Diffuse multipath power spectra

An example of a fully reconstructed wavenumber spectrum for a single snapshot is given in Fig. 4.7. The shape of the diffuse component background is clearly seen, for the first time, at such low grazing angles. Further confidence is gained by estimating the jackknife bounds (Fig. 4.8) of the same spectrum. Note that these bounds, if anything, are very conservative, which means that the actual bounds are tighter. The power spectrum estimation technique, can be expanded to include more than one snapshots and this is done for all the 127 snapshots in a dataset. Putting together all these average spectra for the fixed channels (same frequency), of a collection of datasets, at the same Xmtr/Rcvr heights, collected in the same day and closely enough in time, we have Figs. 4.9 and 4.10, for the wavenumber and frequency domain power spectra respectively. Each line graph in

[2]This is used to some advantage in the data calibration procedure [37].

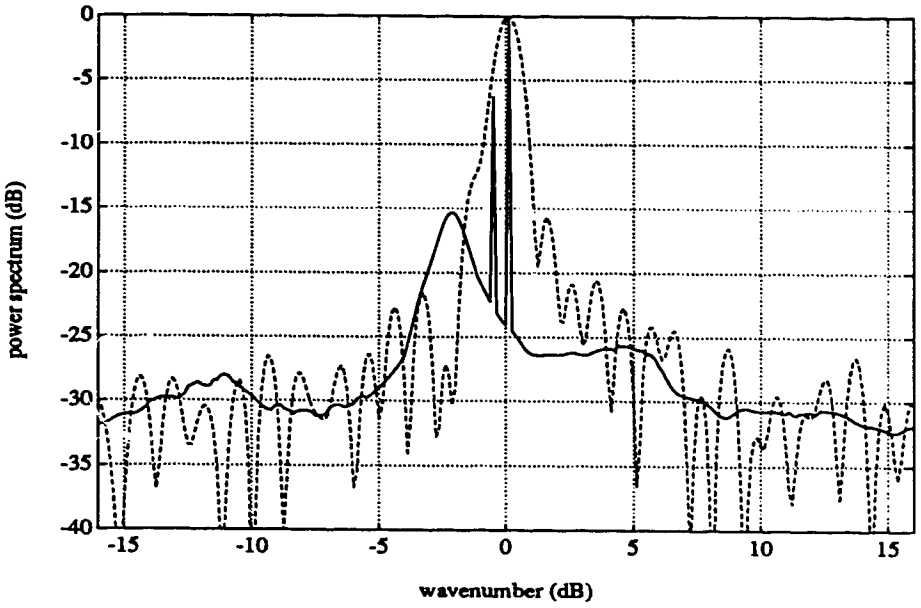

Figure 4.7: The fully reconstructed wavenumber spectrum of the first snapshot of *nov3:dh3;2* far-field calibrated with *nov2:cff2;1*. The dashed line shows the corresponding rectangular periodogram estimate of the spectrum.

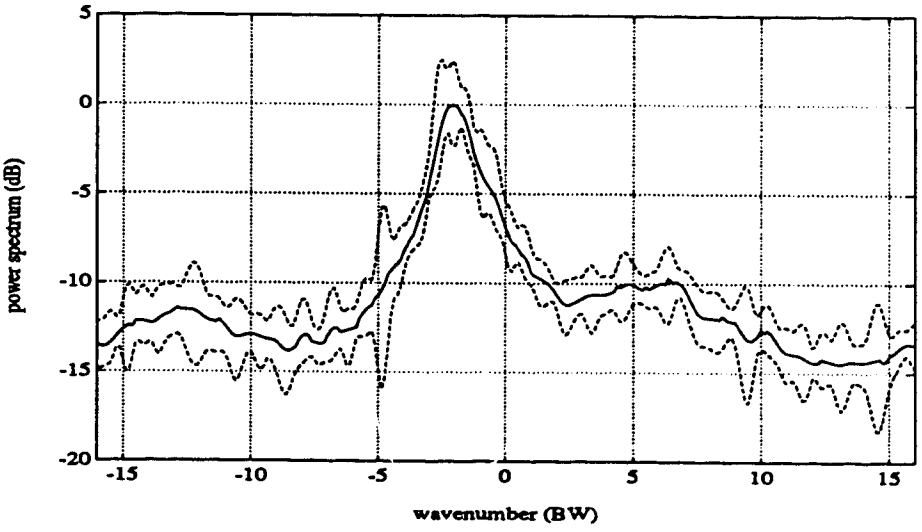

Figure 4.8: The diffuse component of the above spectrum with the jackknife bounds.

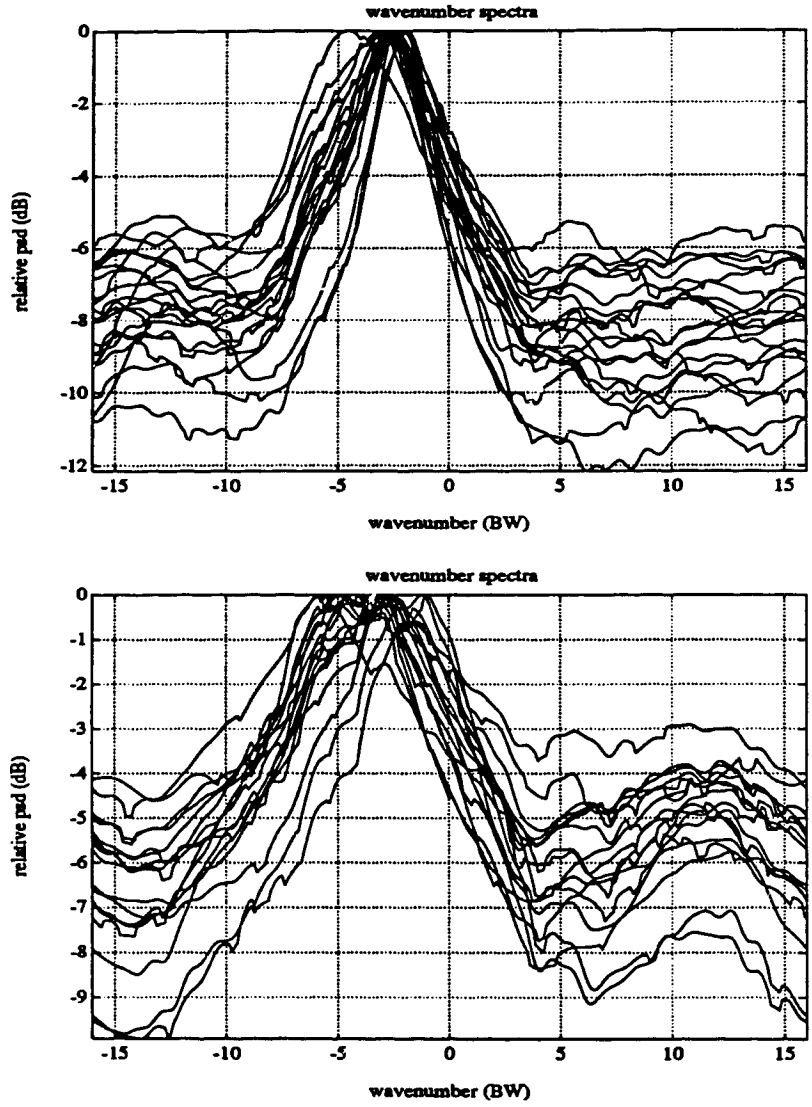

Figure 4.9: The wavenumber spectra of a variety of similar fixed channel datasets from *nov9:dh9;** and *nov9:dh4;** (top graph) and from *nov4:dh9;** (bottom graph). Note that the diffuse peak center at the bottom graph is less well-defined, due to the estimated AOA separation being smaller than that for the top graph case.

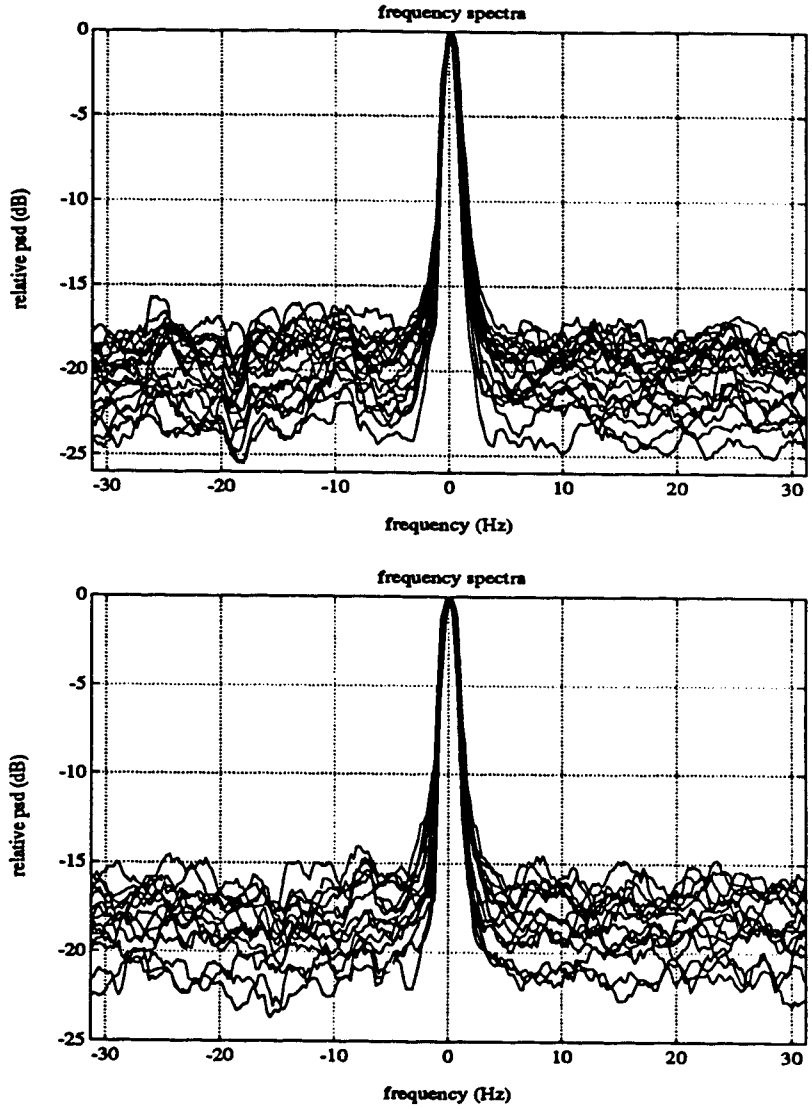

Figure 4.10: The corresponding frequency spectra of the datasets from *nov3:dh3;** and *nov3:dh4;** (top graph) and from *nov4:dh9;** (bottom graph).

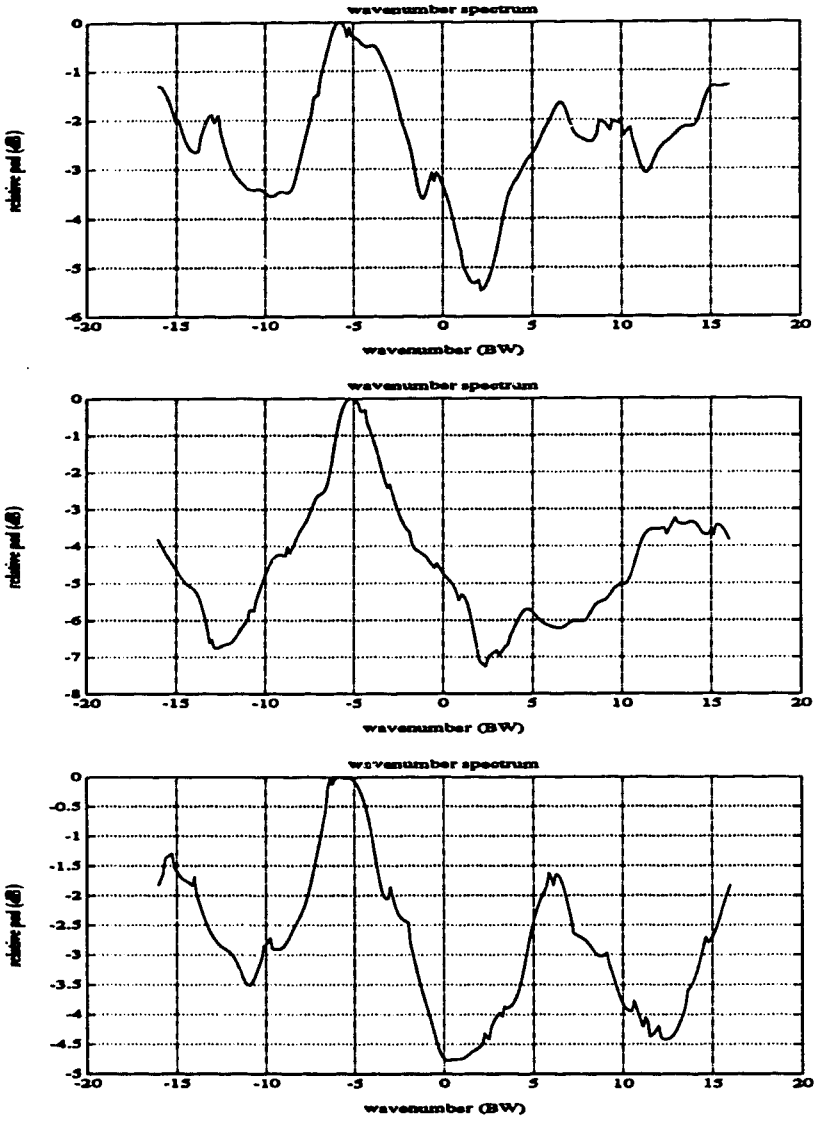

Figure 4.11: The average wavenumber spectra of Datasets 1 – 3 respectively.

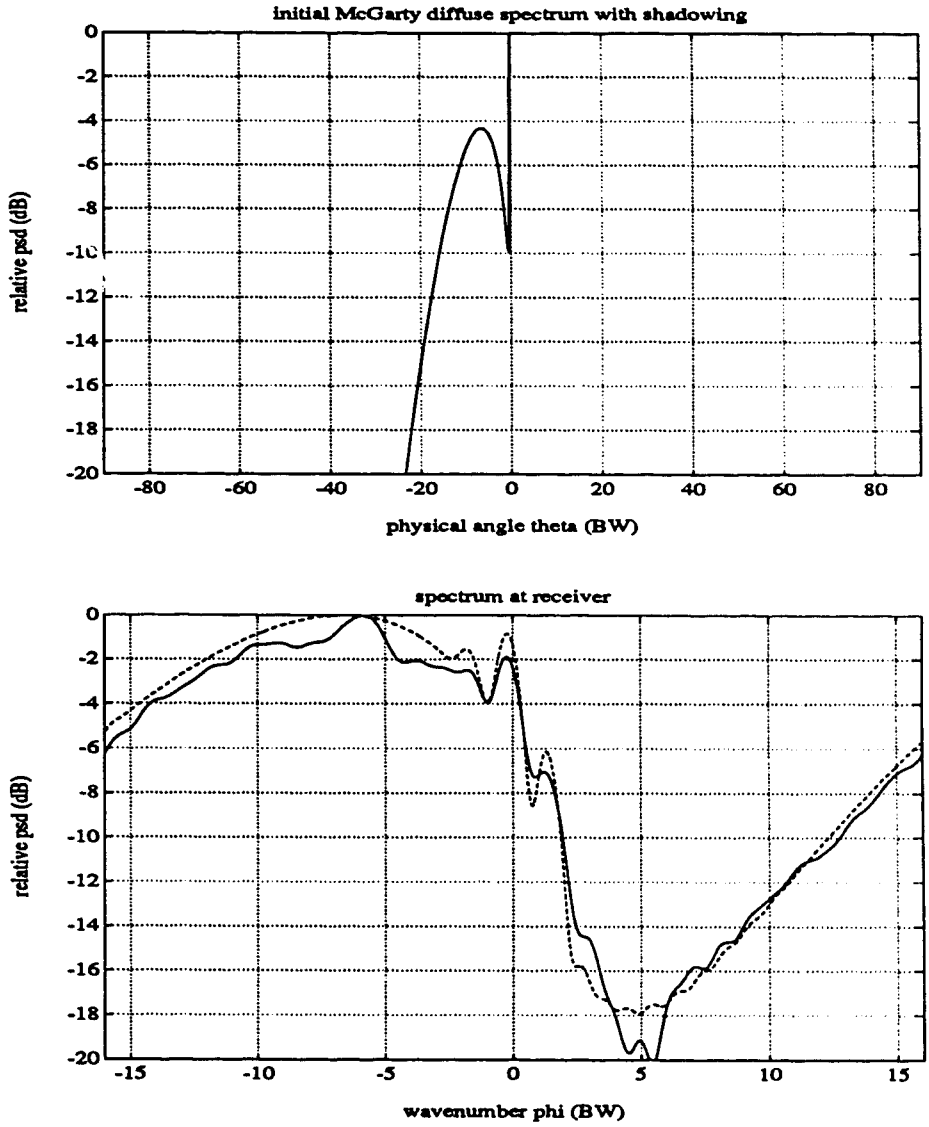

Figure 4.12: The McGarty diffuse spectrum for a geometry similar to ours (top graph). This is transformed in the bottom graph, with wrap-around and grating lobes included, and gives the theoretical spectrum (dashed line) that should be observed at the receiver. The solid line graph illustrates the average spectrum of 127 snapshots, generated by a Karhunen - Loève expansion based on the theoretical spectrum.

the wavenumber domain is an average spectrum from 127 snapshots. The frequency domain spectra are estimated by taking each of the 32 element, time traces and averaging across time. The results from the latter indicate a Gaussian correlation. The average wavenumber spectra from the three datasets in Table 4.1 are also shown in Fig. 4.11 and wrap-around is then clearly evident.

A theoretical investigation using McGarty's quasi-specular model *with shadowing included* is seen from Fig. 4.12 to be in qualitative agreement. Note that there is no horizon component, as Barton's model predicts for the low angle tracking case. The diffuse spectrum is peaking a few beamwidths before the horizon and may extend beyond the unambiguous field of view of the array receiver. Any diffuse power that does so is wrapped around on the positive part of the spectrum.

4.3 Coherencies and Transfer functions

Possible relations between different simultaneous frequency/polarization channels can be derived by estimating the coherency and transfer functions. This would be extremely useful in modelling of complicated processes, particularly in remote sensing, geology, or medical imaging, where a number of different model parameters concerning the reflecting surface or layers, can be expressed as functions of coherencies and/or transfer functions between different channels. Regarding microwave remote sensing of the sea surface, the relation between the wind, driving the sea waves, and the surface scattering coefficient, is something that is already used in remote sensing satellites.

Figs. 4.13 – 4.15 display the Mean Squared Coherence (MSC), its phase, the magnitude of the transfer function and the ratio of variance estimated by the jackknife to the conventional (normal-theory) variance of the transfer function [124]. For the latter quantity, a value larger than one, indicates non-linearities present. The estimates shown are for both wavenumber and frequency domains.

We observe that:

1. Fig. 4.13 is typical for all channels. All 127 snapshots (or 32 times traces) are combined in the estimation and a low degree of coherency is obtained. The technique of investigating channel cross-correlations was also implemented in [82] (although for Doppler spectra and different polarizations) and their explanation for low cross-correlation was that different parts of the scattering surface were responsible for each channel. The same interpretation is given here as well.

2. Fig. 4.14 uses the unfiltered channels of the same datasets. As expected, the existence of the coherent direct and specular components is seen to increase the degree of interchannel coherence.

3. Finally, in Fig. 4.15, two single consecutive snapshots (time traces) are investigated. The degree of coherency is again increased, but the estimator variance (jackknife bounds) becomes

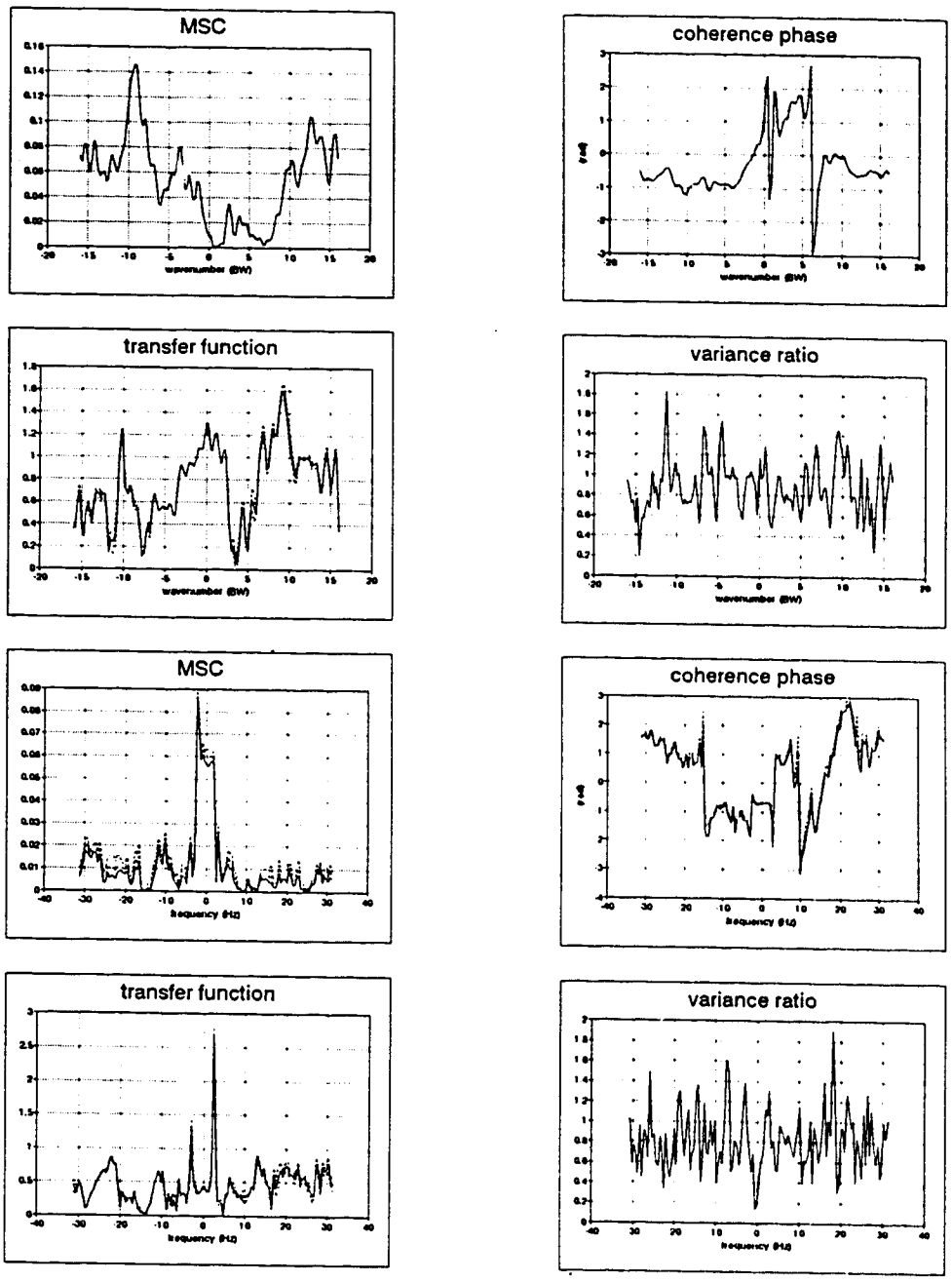

Figure 4.13: Coherence and transfer function for *nov4:dh9;1* fixed (10.2 GHz) and agile channel (8.05 GHz), concurrent collection. The top four graphs are for the wavenumber domain, while the bottom four are for the frequency domain. Similar results are obtained for all different frequency channels.

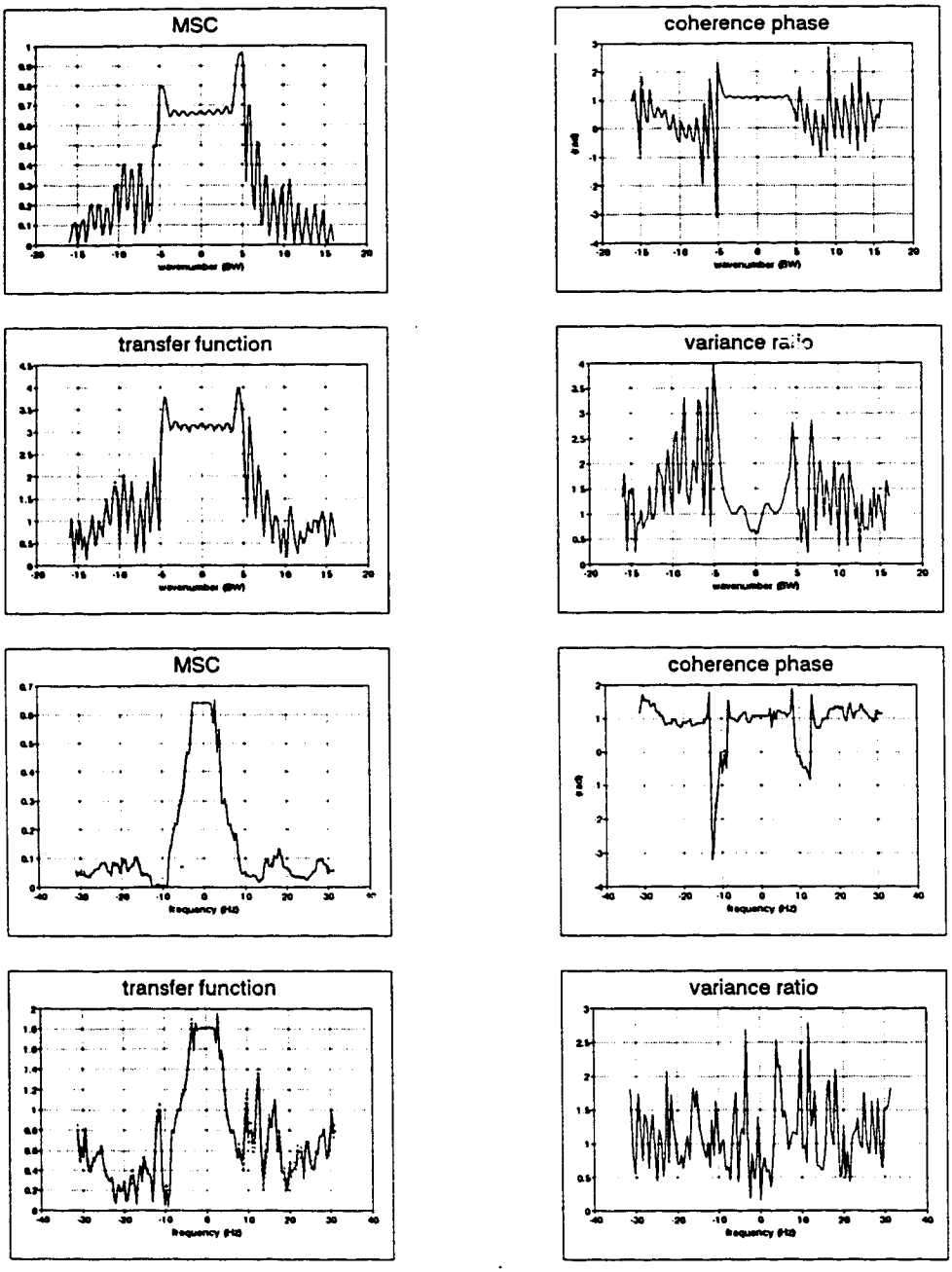

Figure 4.14: Coherence and transfer function for *nov4:dh9;1* fixed and agile channel, 10.2 and 8.05 GHz respectively, concurrent collection. The unfiltered datasets that contain the coherent direct and specular components are used.

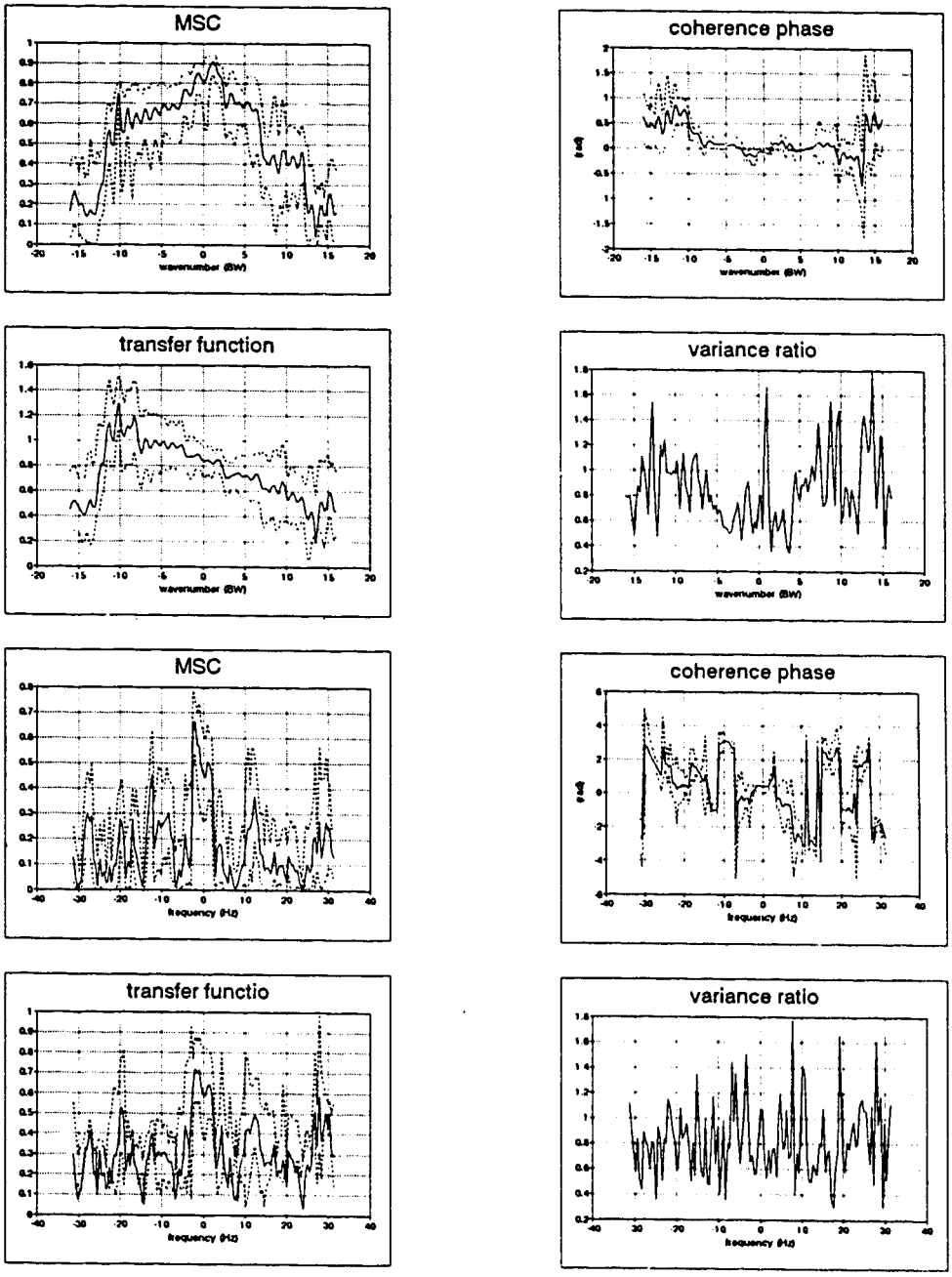

Figure 4.15: Coherence and transfer function for *nov4:dh9;1* fixed channel; 1st and 2nd snapshot (top 4 graphs); 1st and 2nd time trace (bottom 4 graphs).

larger too, since there are fewer samples. Taking snapshots (time traces) at larger separations, the estimator results come closer to those of Fig. 4.13.

The conclusion from this exercise, for the Lake Huron database, is that the data are reasonably decorrelated from channel to channel. However, this is not so for snapshots (time traces) that are close together and care must be taken if sample independence is desired.

4.4 Amplitude statistics

Diffuse multipath is a form of radar clutter. As such, its amplitude statistics should exhibit similar behaviour. It is well known that when the resolution cell on the scattering surface is large, and contains many scatterers, the combined signal is a Gaussian random phasor (law of large numbers) leading to Rayleigh amplitude statistics. Shadowing, or smaller resolution cells, contain less scatterers, leading to longer tailed distributions like the log-normal. It is now commonly accepted that the K-distribution covers the above two extreme cases, including the ones in-between.

After extracting the direct and specular components, we should be left with the diffuse multipath component plus thermal noise. Assuming that the amplitude distribution is K distributed with thermal noise present, Watts [135], gives formulas to estimate the shape ν and scale b^2 parameters of the best fitted K distribution, including the thermal noise power $2\sigma^2$. These are based on the 2nd, 4th and 6th moments (about zero) of the data. Since higher order moments are very sensitive to the data size, a large number of samples is required. For this reason, similar datasets, of 127 snapshots each, are combined into two large, augmented, datasets (the same ones used for the power spectra in Figs. 4.9 – 4.10). The first has $127 \times 32 \times 18 = 73,152$ data samples and the second $127 \times 32 \times 32 = 130,048$. These should be enough samples for a valid conclusion to be drawn. Indeed, in Table 4.3 the results support the K distribution assumption.

The difference of the before and after case is quite striking in Figs. 4.16 – 4.17. It clearly shows the power of MWM to effectively filter out the direct and specular components. Two important implications of these results are:

1. Despite the CW nature of the microwaves employed in the experimental data collection, which uses the largest possible area of the sea surface for scattering (i.e. large resolution cell), the low-grazing angle conditions are enough to limit the amount of scatterers (i.e. limit the size of the illuminated part of the surface) effectively leading to K distributed amplitude statistics.

2. Since the amplitude statistics are K distributed, the underlying process is non-Gaussian, justifying the use of higher-order statistics.

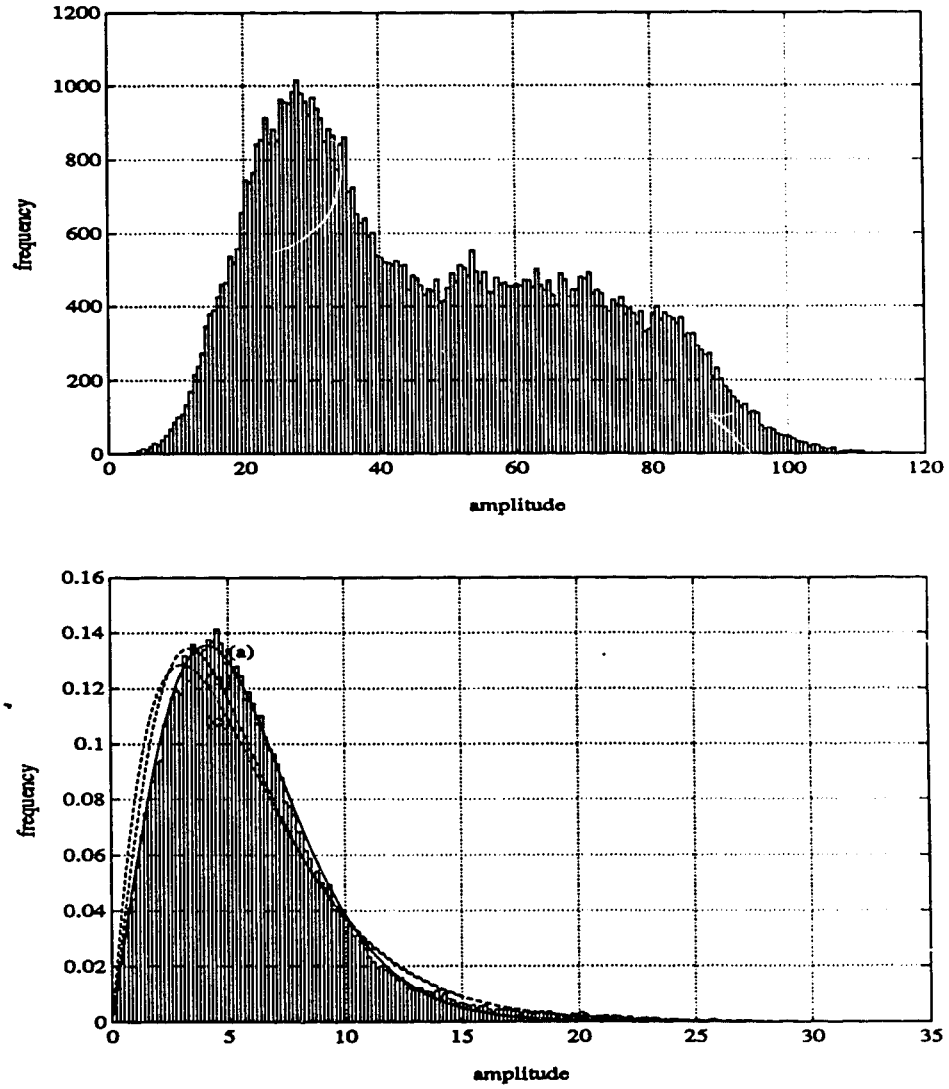

Figure 4.16: Amplitude histogram of 18 fixed channel datasets from *nov4:dh9*. The top graph is before extraction of the direct and specular components with MWM, while the bottom one is after. 200 bins are used. In the bottom graph, curve (c) is the PDF of the no-thermal noise model, curve (b) is the PDF of the thermal noise model and (a) of the least squares fit of the thermal noise model.

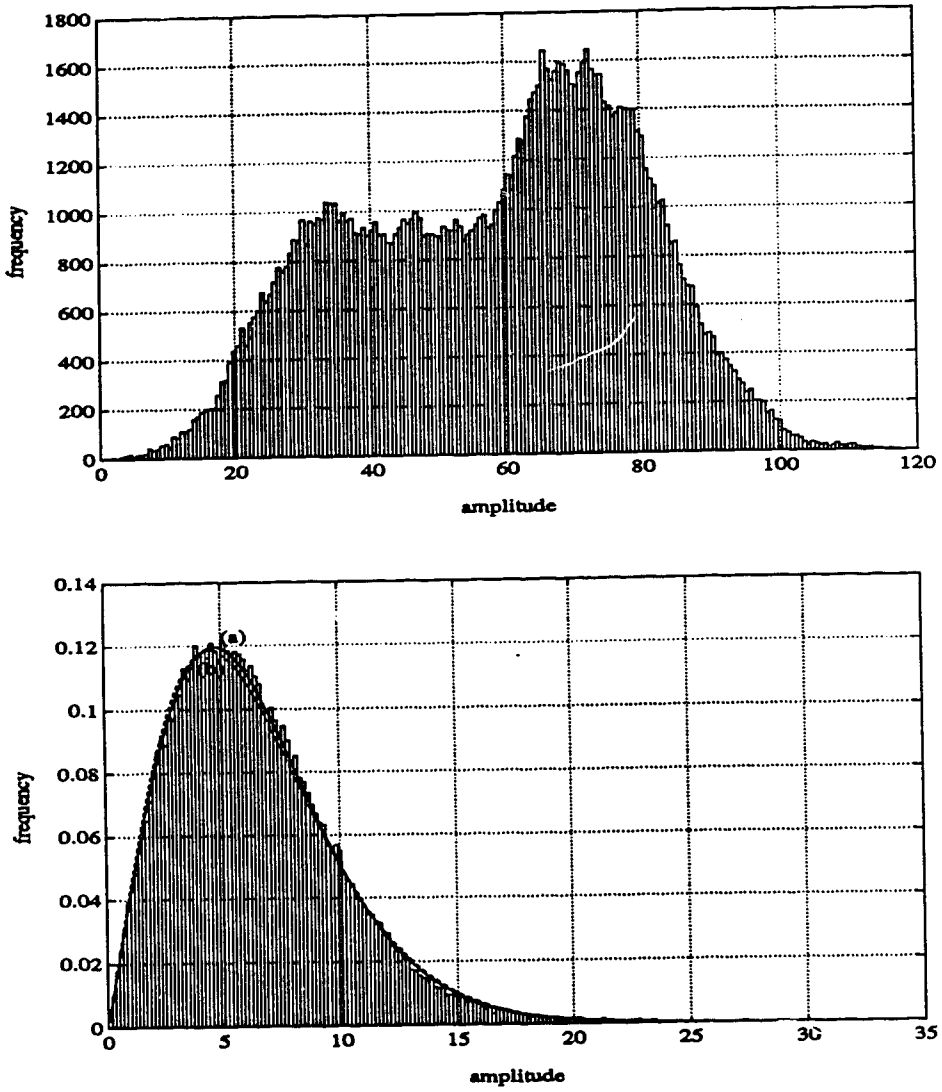

Figure 4.17: Amplitude histogram of 32 fixed channel datasets from *nov3:dh3* and *nov3:dh4*. The top graph is before extraction of the direct and specular components with MWM, while the bottom one is after. Again, 200 bins are used. In the bottom graph, curve (b) is the PDF of the no-thermal noise model and curve (a) is the PDF of the thermal noise model.

Table 4.3: The results from assuming K-distributed amplitude statistics. The shape ν and scale b^2 parameters with and without thermal noise of power $2\sigma^2$. The Kolmogorov-Smirnov test is applied to the latter case as well.

dataset	with thermal noise				without noise	
	ν	b^2	$2\sigma^2$	*KS test*	ν	b^2
nov4:dh9	1.197	3.713×10^{-2}	7.623	0.095	1.683	4.402×10^{-2}
nov3:dh3 + dh4	1.324	6.377×10^{-2}	27.79	0.999	5.571	1.308×10^{-1}
nov4:dh9 LS fitted	1.085	6.636×10^{-2}	21.78	0.938		

4.5 Bispectrum

Higher-order statistics or spectra, suffer from the same problems as higher order moments. A large number of good quality samples are required for accurate results and the higher the order, the more sensitive and "fragile" are the estimates. The third order statistics with the bispectrum are investigated in this section. As far as the author is aware from the published open literature, this is the first time that this is done for diffuse multipath at low grazing angles conditions. Figs. 4.18 - 4.21 show the results in both wavenumber and frequency domain, for the two large datasets of the previous sections. The MWM technique for estimating the bispectrum is employed, which should extract the desired information in an optimum manner from the amount of data available. Not surprisingly, a strongly non-zero bispectrum magnitude is evidence that, diffuse multipath, at low grazing angles, is non-Gaussian in character. Note that this does not imply that the 2nd order analysis with the power spectra is useless. The bispectrum is "blind" to Gaussian processes and a large bispectrum magnitude does not mean that the non-Gaussian component of the combined process is larger than the linear (Gaussian). It simply makes available phase information that the power spectrum suppresses, showing the non-linear coupling (quadratic and higher) in the frequency or wavenumber components of diffuse multipath.

To get a better "feeling" on what the bispectrum tells us, we have to look into theoretical models of the sea surface that take account of non-linearities. An excellent reference is available in Longuet-Higgins [77] where the effect of non-linearities, on statistical distributions, in the theory of sea waves, is discussed. The model investigated there, is that of "free" waves, in which the viscous damping is neglected and the stresses at the free surface are assumed to be identically zero. Both the surface height and surface slope distributions are expanded to include non-linear terms. For radar scattering, it is the latter distribution that is more significant, since only when the slopes (facet model) are properly oriented, is there energy transmitted to the Rcvr. The development describes the surface heights and slopes as weakly non-linear, i.e. their representation, in the first order approximation, is a sum of independent random components (that converges to the Gaussian for both quantities). However, quadratic and higher order interactions between the components can

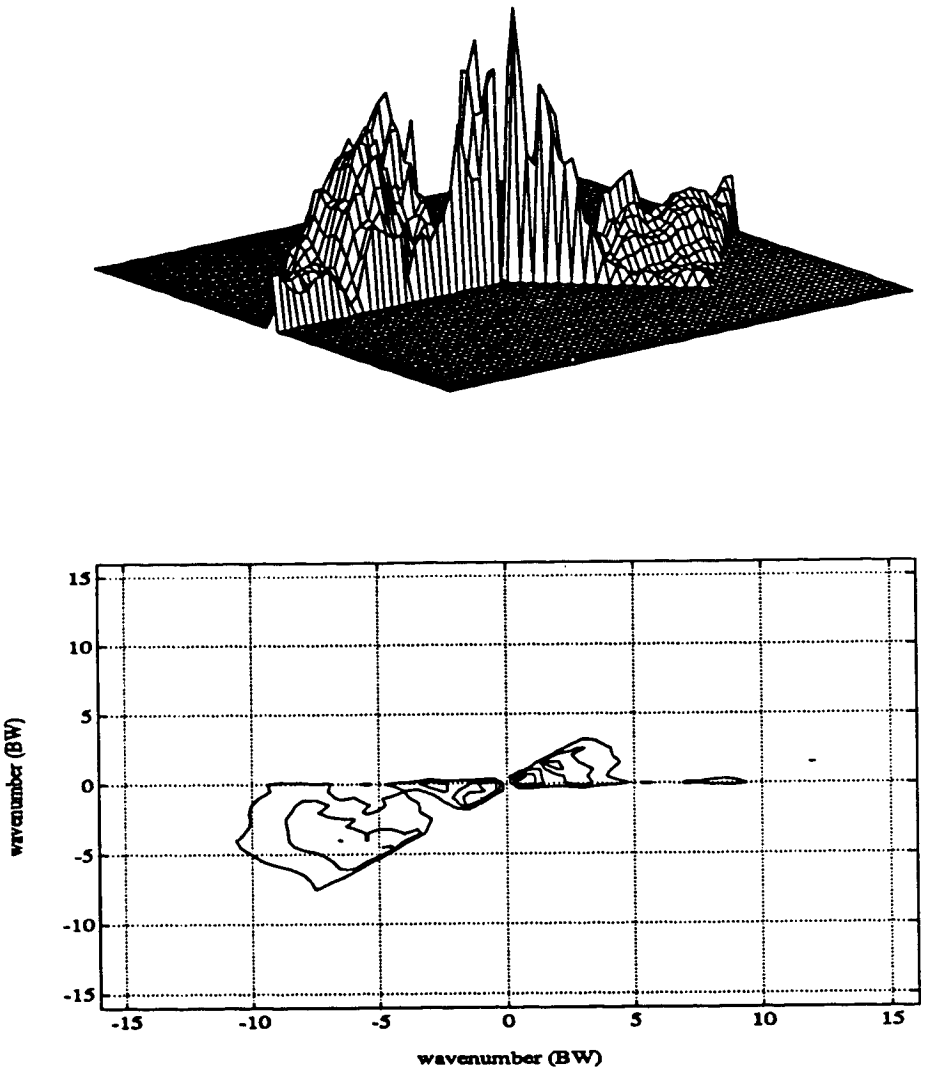

Figure 4.18: Bispectrum magnitude of all *nov4:dh9* fixed channel datasets, wavenumber domain. Peak value is 228.07.

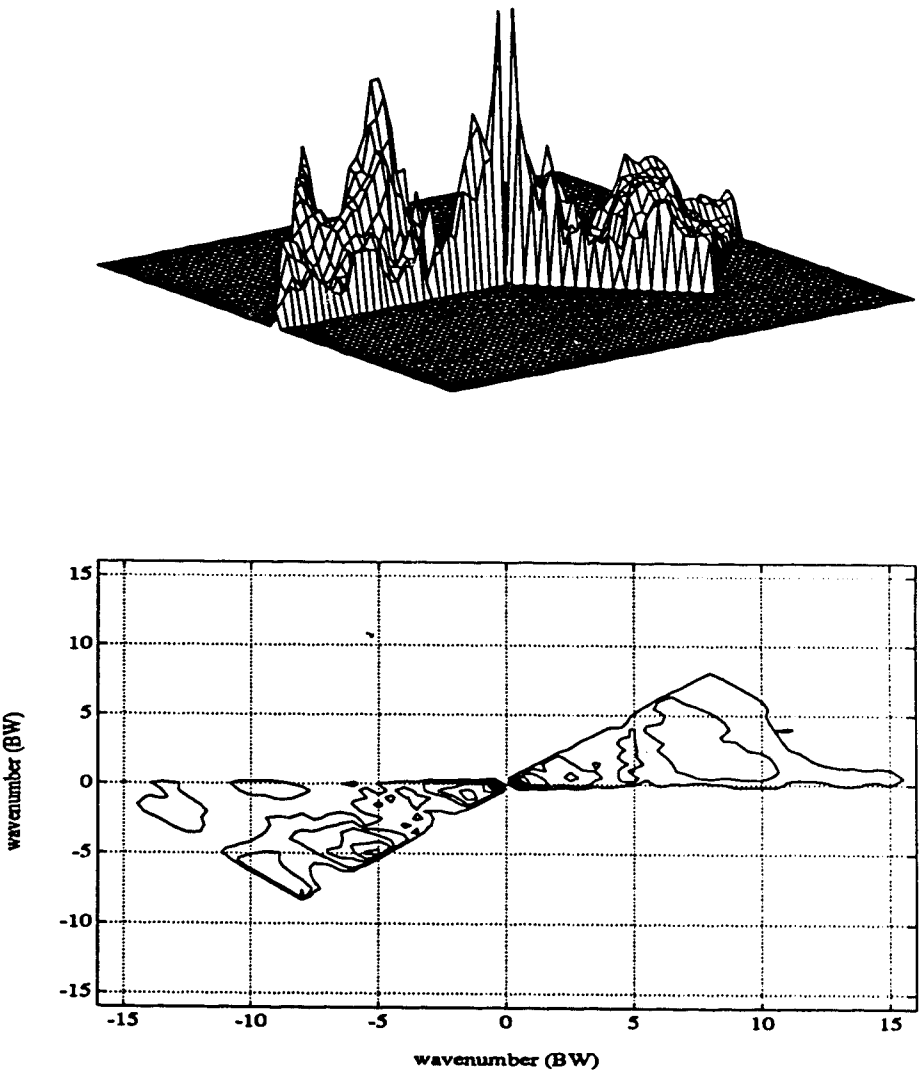

Figure 4.19: Bispectrum magnitude of all *nov9:dh9 + dh4* fixed channel datasets, wavenumber domain. Peak value is 144.58.

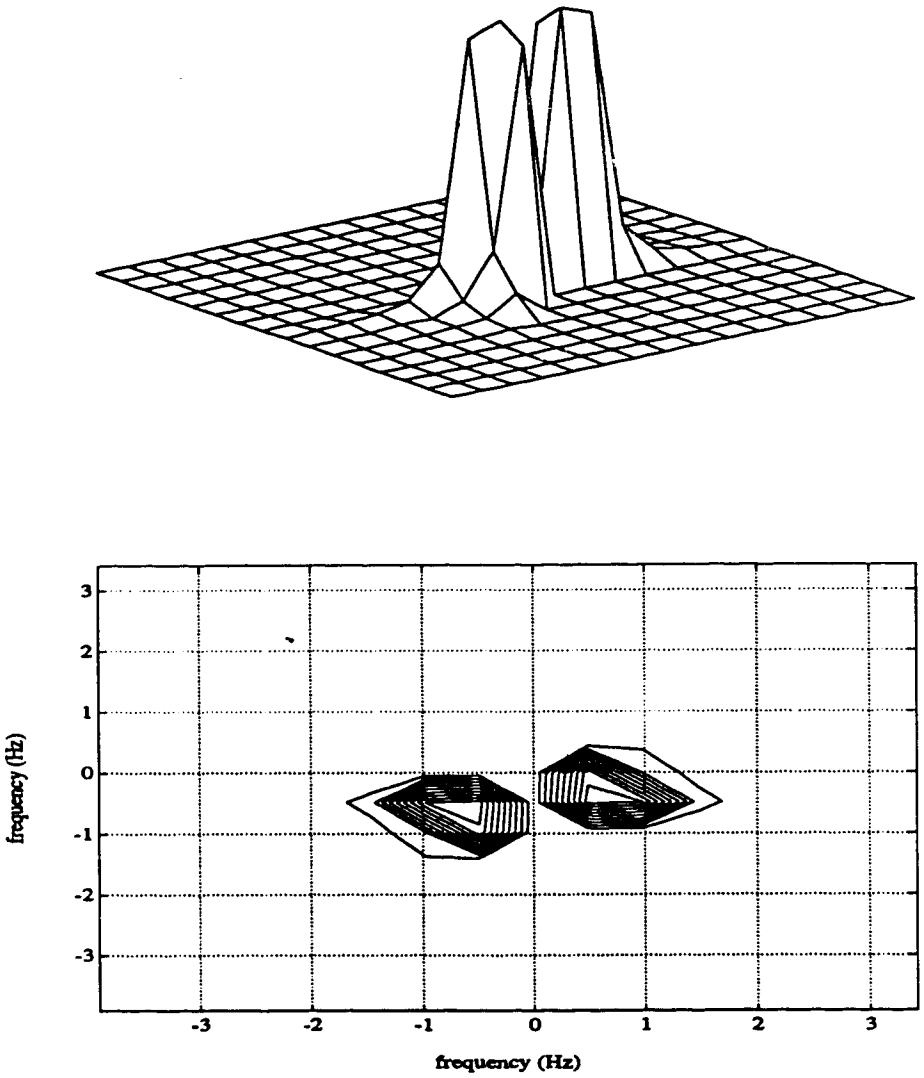

Figure 4.20: Bispectrum magnitude of all *nov4:dh9* fixed channel datasets, frequency domain. Peak value is 1.89×10^4.

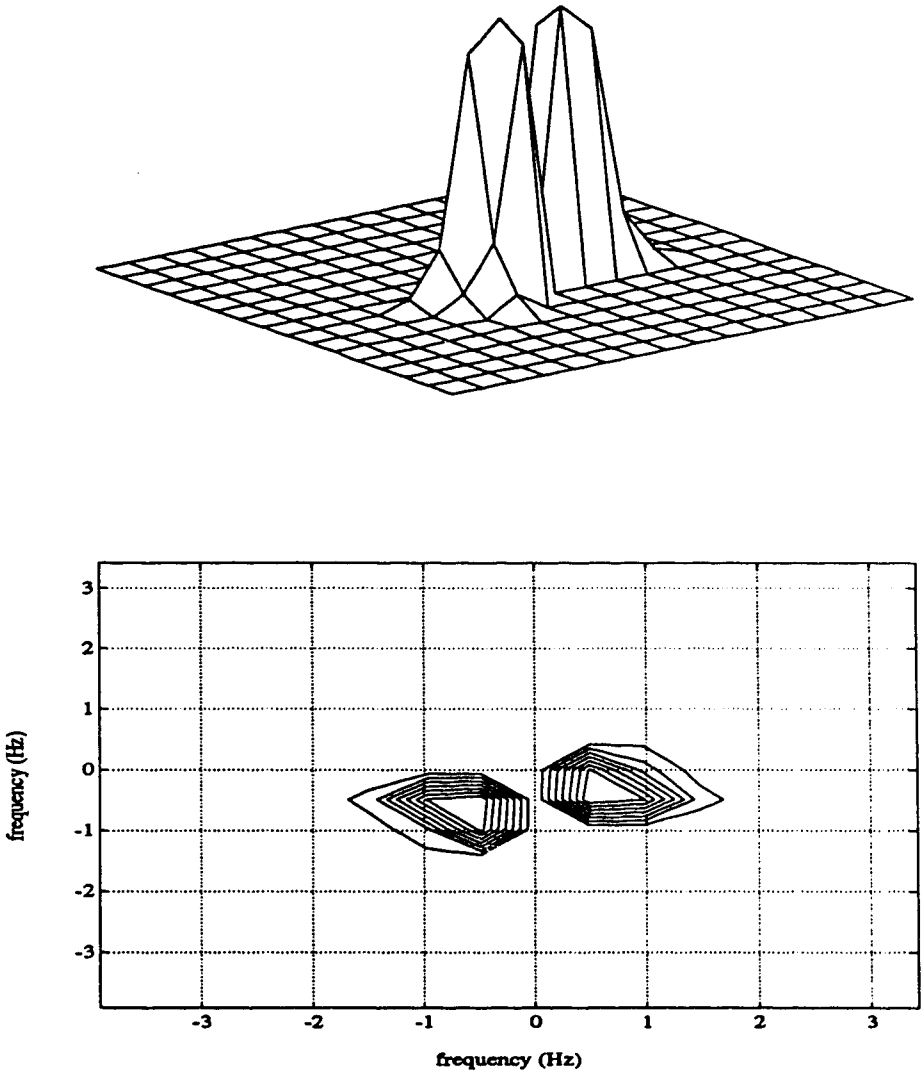

Figure 4.21: Bispectrum magnitude of all *nov3:dh3 + dh4* fixed channel datasets, frequency domain. Peak value is 1.58×10^4.

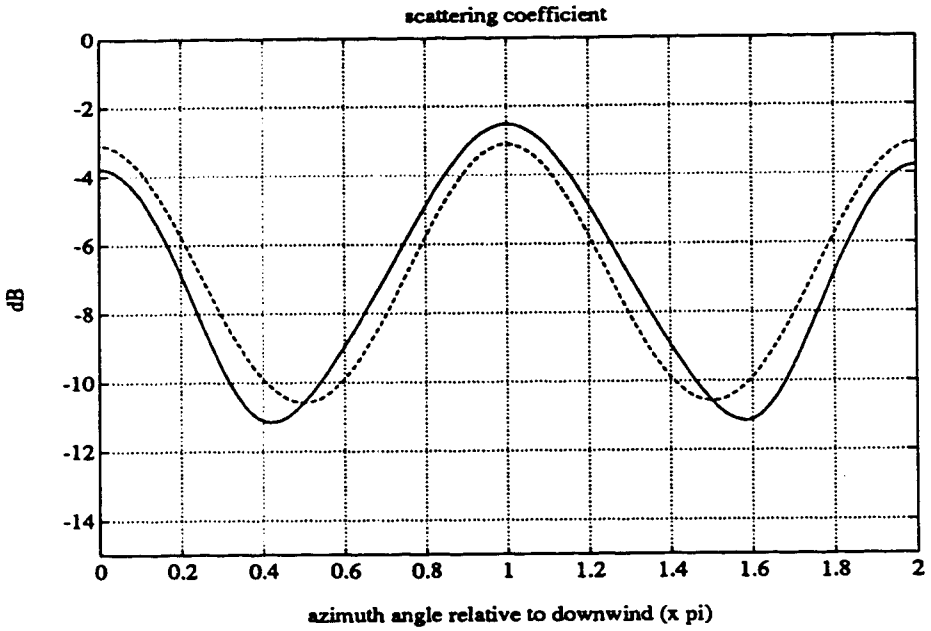

Figure 4.22: The backscatter scattering coefficient for the Kirchhoff approximation of the skewness model of Chen and Fung, as a function of the wind direction. The solid line graph includes skewness, while the dashed one does not. It can be seen that skewness destroys the symmetry of the non-skewness model, making possible the discrimination of upwind and downwind directions.

no longer be entirely neglected. The bispectrum is defined as the Fourier transform of the third-order moments of a process, and is therefore related to the "skewness". In fact, both distributions (heights and slopes), are experimentally shown to have non-zero skewness, the latter being of the same or higher order of magnitude than the former. This non-zero skewness of the slope distribution has the physical meaning of asymmetry about the mean, implying that time reversal is not possible (forward wave slopes become rear slopes and vice versa without altering the surface statistics). Such asymmetry is caused by energy transfer between different parts of the surface wavenumber spectrum and also by viscosity and atmospheric stresses on the sea surface. As such, the skewness, and by implication the bispectrum, may be a sensitive indicator of energy transfer and dissipation within the water. Note also, that the part of the surface wavenumber spectrum that microwaves are resonant with, are the short wavelength ripples (capillary waves). The received signal therefore, is going to be influenced by that part of the spectrum predominantly, with the larger gravity waves providing some modulation (see also [78]). Not much is known about the exact shape of this surface wavenumber spectrum and the non-zero, sea return, bispectrum, observed in this investigation, points to a potentially useful avenue of extracting this information.

Chen and Fung [28] have recently (1991) proposed a scattering model that attempts to include 3rd order non-linear effects through the introduction of a skewness function in the slope distribution. This leads to a scattering coefficient that breaks into two parts. One, not including the skewness function and the other, directly proportional to the Fourier transform of this function (definition of bispectrum). The model employs the Integral Equation Method (IEM) and the Kirchhoff approximation. No shadowing, multiple scattering or diffraction effects is included, but this is clearly the right way to go in order to explain the experimentally observed facts. Numerical examples and experimental data are used for the backscattering case. In fact, a version based only on the Kirchhoff and stationary phase approximation is given in [45]. The development there, is duplicated here, to extract a similar curve of the scattering coefficient as a function of the azimuth angle relative to the downwind direction. The difference is relatively minor, but the upwind and downwind directions are clearly picked out when the non-linear component is included in the model due to the difference in levels between the two directions.

4.6 Summary

The signal processing tools described in the previous chapter were employed in investigating the experimental database. Thomson's MWM proved to be a powerful technique for filtering out the direct and specular components through AOA estimation. 1st, 2nd and 3rd order statistics were extracted through the estimation of

1. the amplitude distribution, which was shown to be K distributed,

2. the power spectra (both wavenumber and frequency domain) showing the exact shape of diffuse multipath in those domains, and

3. the bispectrum, which offers the potential of extracting additional information from the sea surface.

In addition to the above, MWM was employed in estimating coherencies and transfer functions between different frequency channels.

Chapter 5

Conclusion

The main goal of this thesis is the experimental investigation of diffuse multipath at low grazing angles. The Lake Huron database, provides data of different X-band carrier frequencies and varying grazing angle conditions. Only HH datasets were investigated, due to calibration difficulties with the HV datasets. This provided enough information, that with the help of Thomson's MWM some important finding were made:

- First order statistics, the amplitude distribution of diffuse multipath was estimated, and agreement was observed with the recent theory of K distributions.
- The general shape of the wavenumber power spectrum is found. A simple theoretical model was implemented and *only with shadowing included* was there agreement between theory and experiment.
- The bispectrum was estimated, both in the wavenumber and frequency domain. Results indicate evidence of a non-Gaussian structure present.
- Finally, an important tool was developed, Thomson's MWM. This provided the best possible *non-parametric* estimates, of the 2nd and 3rd order statistics of the lake Huron dataset. The ability to estimate line components, both frequency/wavenumber and complex amplitude, in the presence of unknown coloured noise, *without disturbing the noise*, was successfully implemented in AOA estimation and in the data calibration.

Thomson's MWM is a technique that is still in a state of development. The adaptive spectrum employed here, is a relatively simple robust estimator, suitable for the quality of the Lake Huron datasets. More complex estimators are possible, but there are still questions concerning their behaviour for low power areas of the spectrum.

Regarding AOA estimation of an unknown number of sources, in unknown coloured noise, the F-test statistic performs as a threshold detector. Note that the integral regression version is shown

to be more robust, but work is still required to formulate the correct expressions for estimator bias and variance.

In applying the method, user interaction is necessary, to choose various time-bandwidth products that "tunes" the estimator to the desired signal. There is no "automatic" way like Akaike's criterion of estimating the number of tones present. Again, the double line F-statistic is very intensive computationally, requiring hours of computer time to estimate a single 256 point grid (the fault probably of the author's "brute-force" implementation). It would be nice if this could be sped up.

Concerning the results from the experimental investigation:

1. The amplitude distribution of the diffuse multipath component was shown to be K distributed. This is due to the low grazing angle conditions that introduce shadowing, multiple scattering and diffraction effects, limiting the number of scatterers from the large scattering area that is available for CW radiation. For high grazing angles, the expected form of the amplitude distribution is Rayleigh.

2. The general shape of the power spectrum of diffuse multipath, in the wavenumber domain, is now available. More realistic simulations and radar system performance evaluations can now be done without a priori assumptions. In fact, MWM is already implemented in actual radar systems [23], for the purpose of estimating the background spectrum, to construct better prewhitening filters.

3. Coherence and transfer function estimation between different channels can be estimated. For the database employed here, the only information that came out from this investigation, was a measure of the decorrelation/independence of consecutive snapshots/time traces. A theoretical treatment of EM scattering can provide models of the scattering coefficient ratios, for different frequencies and more particularly, polarizations. This ratio can be related to both coherence and transfer functions between the different channels and is much more sensitive to the model structure. This was not done here, as a more complex, two-scale model would be the minimum requirement for this theoretical investigation.

4. The most novel result, however, concerns the bispectrum estimates which clearly shows a non-Gaussian structure for diffuse multipath. Note that the bispectrum is mainly related to slope skewness, of the order of σ^3 where σ is the rms variance of the slope distribution [77]. It is also known, that the surface structure of the sea is in general weakly non-linear. Diffuse multipath, scattered from such a surface, can therefore be characterized as weakly non-linear also. Investigations of the bispectrum can lead to a better understanding of the actual spectrum of the capillary waves and their modulation from the larger gravity waves, something that is still not well known today. However, a finer sampling rate in time, is a definite requirement, in order to investigate the low frequency regime $\sim 0-1$ Hz. Experiments in the future should implement that.

To summarize, the overall contribution from this thesis is, that it provides experimentally based foundations for a more accurate model implementation of EM scattering from the rough sea surface.

Appendix A

Simulating K distributions

The K distribution is recent enough that, there is as yet no standard pseudorandom number (PRN) generator for it. The straightforward approach is to use the transformation method described in [103, page 200]. A desired PRN can be generated from a transformation of uniform $U[0,1]$ deviates, if the cumulative distribution function is known. The requirement here is the ability to compute the modified Bessel function K_ν for fractional values of ν in general. Numerical Recipes [103] and Abramowitz and Stegun [1] offer approximating formulas only for integer and half-integer ν's. IMSL generalizes to fractional values of ν, but their implementation is still somewhat cumbersome to use. A different approach, based on a numerical method of solving an associated Fokker-Planck equation is described in Oliver and Tough [99]. An approximate technique is also discussed there, where one can impose temporal and spatial correlations on the K distributed PRN's, bringing the quality of simulations closer to "reality"; Oliver's method offers a simple algorithm for generating Gamma-Lorentzian noise, implying that there are several additional steps that still need to be taken before one can have standard K distributed PRN's. See also the recent letter by Armstrong and Griffiths [3] where some improvements are made, in this area.

The standard form of the K distribution is:

$$p(x) = \frac{4c}{\Gamma(\nu)}(cx)^\nu K_{\nu-1}(2cx) \tag{A.1}$$

derived from the integration of

$$p(x) = \int_0^\infty p(x|y)p(y)dy$$

where $p(y)$ is the $\chi_{2\nu}$ distribution of the mean local level y of the amplitude x

$$p(y) = \frac{2b}{\Gamma(\nu)}(by)^{2\nu-1}\exp(-b^2y^2)$$

Given y, the speckle component follows the Rayleigh distribution

$$p(x|y) = \frac{\pi x}{2y^2}\exp\left(-\frac{\pi x^2}{4y^2}\right)$$

where $c = b\sqrt{\pi/4}$ and ν are the scale and shape parameters respectively, of the K distribution.

D'Addio et al. [33] was brought to my attention from a reference in the UNIX USENET. Their work is based on Ward's observation that "the product of a Rayleigh distributed random variable (r.v.) by a generalized $\chi_{2\nu}$ distributed r.v. (i.e. the square root of a generalized chi-squared r.v. with 2ν degrees of freedom, $\chi^2_{2\nu}$) is K distributed". Working through their formulas, the following recipe is extracted for independent K distributed PRN's:

Given a Rayleigh r.v. R of mean value one, with

$$f_R(y) = \frac{\pi y}{2} \exp\left(-\frac{\pi y^2}{4}\right) \qquad 0 < y < \infty$$

and a $\chi_{2\nu}$ r.v. C with

$$f_C(x) = \frac{2b^{2\nu}}{\Gamma(\nu)} x^{2\nu-1} e^{-b^2x^2} \qquad 0 < x < \infty$$

their product $A = C \cdot R$, using the appropriate formula from Papoulis [100, page 146] for the density of the product of two r.v.'s (*and assuming independence of R and C making the joint density the product of their individual ones*) is the desired (A.1).

The Rayleigh r.v. R is generated from the square root of the exponential

$$\mathcal{E} = -\frac{4}{\pi} \ln(1-u)$$

where $u \sim U[0, 1]$.

The $\chi_{2\nu}$ r.v. C is similarly generated from the square root of a $\chi^2_{2\nu}$, which is a special case of a gamma distributed variable G. For integer values of ν the function *GAMDEV* from [103] is found useful (after scaling with $1/b^2$). For half-integer ν, G can be easily enough generated as a sum of $m = 2\nu$ squared normal deviates, or (from the IMSL manual) as

$$G = -2 \ln \prod_{i=1}^{m} u_i + n_i^2$$

where $u_i \sim U[0, 1]$ and $n_i \sim N(0, 1)$. Finally, if ν is not an integer/half integer and k is its integer part, i.e. the greatest integer contained in ν, the following procedure is used:

If $(\nu - k) \leq 0.015$ or $(\nu - k) \geq 0.985$, G is generated as a gamma with integer parameter (Erlang) $Er(k)$ or $Er(k+1)$ respectively. Otherwise, two uniform PRN's from $U[0, 1]$, u_1 and u_2, are generated and the quantity W computed

$$W = u_1^{1/(\nu-k)} \left(u_1^{1/(\nu-k)} + u_2^{1/(1-\nu+k)}\right)^{-1}$$

Moreover, an exponential $T = Er(1)$ and an Erlang $Z = Er(k)$ are generated, and the final gamma G is obtained from

$$G = Z + TW$$

Results are shown in Fig. A.1 for two cases of ν and $b = 1/\sqrt{2}$.

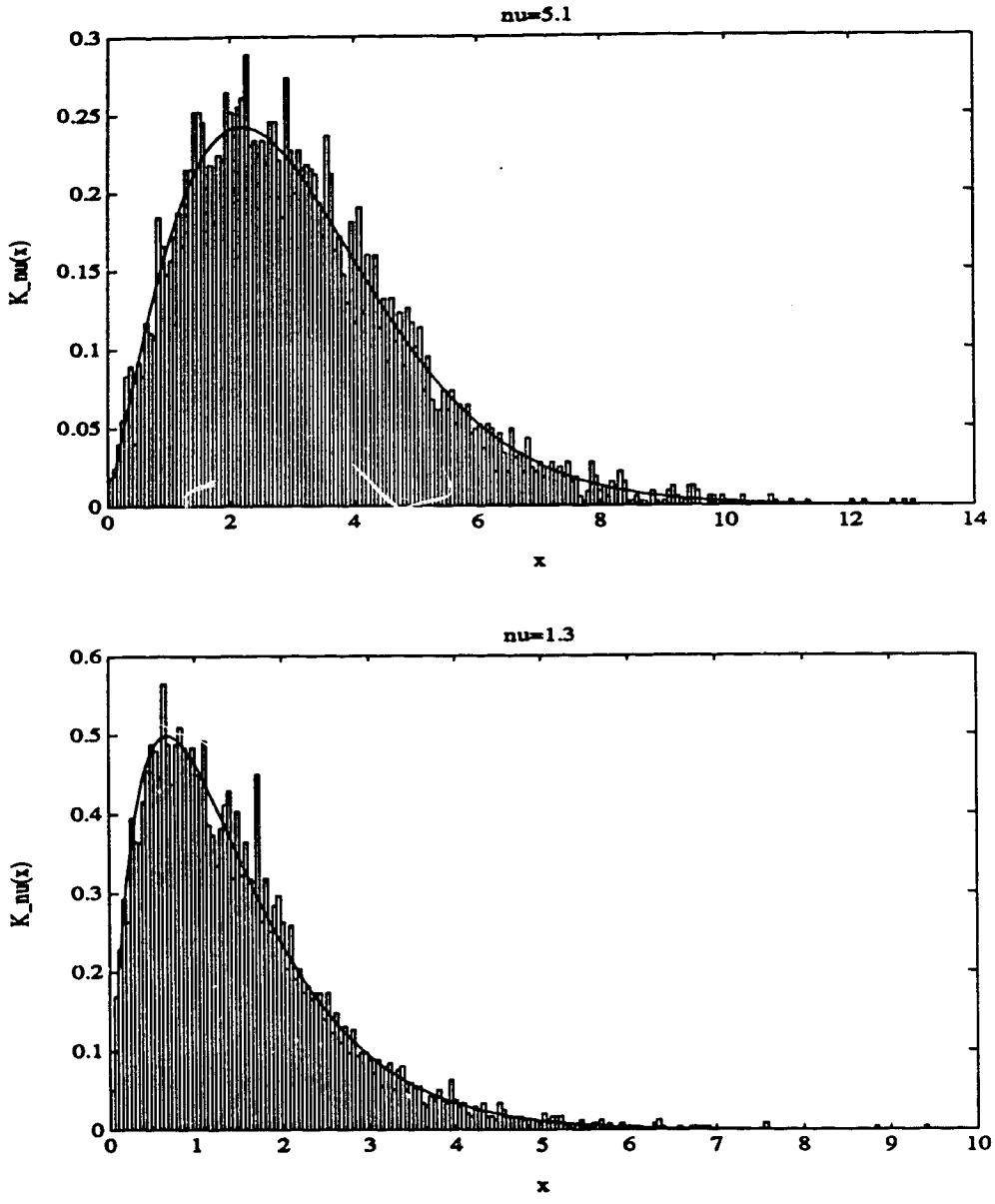

Figure A.1: Histograms of 5000 K distributed PRN's together with the theoretical probability density for two values of ν and the same $b^2 = 0.5$.

Table A.1: The shape ν and scale b^2 parameters estimated from the moment method. Thermal noise of power $2\sigma^2$ is assumed in one case. The other case assumes zero noise present. The datasets are generated with $\nu = 5.1$, and $\nu = 1.3$ respectively (same $b^2 = 0.5$ for both cases) and to check the effect of the number of samples, datasets of 5000 and 50,000 samples are used. For comparison, 5000 Rayleigh PRN's are also generated from a uniform $U[0, 1]$ and the same procedure applied.

dataset	with thermal noise			without noise	
	ν	b^2	$2\sigma^2$	ν	b^2
$\nu = 5.1$ (5,000 samples)	3.744	0.411	1.340	4.661	0.459
$\nu = 5.1$ (50,000 samples)	2.614	0.352	3.610	4.996	0.487
$\nu = 1.3$ (5,000 samples)	1.247	0.481	0.066	1.297	0.490
$\nu = 1.3$ (50,000 samples)	1.560	0.545	−0.256	1.348	0.507
Rayleigh	1.57×10^{-4}	0.245	1.285	3.906×10^2	3.869×10^2

The converse problem is also of interest. Given a dataset that we assume comes from a K distributed process, how can the ν and b parameters be estimated ? A possible answer is given in [135] in terms of the process moments. A white noise background of $2\sigma^2$ power level may also be included, leading to

$$\nu = \frac{18(m_4 - 2m_2^2)^3}{(12m_2^3 - 9m_2m_4 + m_6)^2}$$

$$2\sigma^2 = m_2 - \sqrt{\frac{\nu(m_4 - 2m_2^2)}{2}}$$

$$b^2 = \frac{4\nu}{\pi(m_2 - 2\sigma^2)}$$

When there is no thermal noise the following expressions are adequate

$$\nu = \left[\frac{m_4}{2m_2^2} - 1\right]^{-1}$$

$$b^2 = \frac{4\nu}{\pi m_2}$$

Binning the data into N intervals (200 are used here) of length Δx, and scaling (so that the total area is 1), the required moments are easily estimated from

$$\hat{m}_n = \sum_{i=1}^{N} x_i^n h(x_i)\Delta x$$

The results are given in Table A.1. The no-noise estimates are seen to be in good agreement with the assumed values. The Rayleigh distribution is also seen to have a large shape value ν (no-noise case), as expected.

Appendix B

Development of Signal Model

B.1 Introducing the channel spread function

Let us define a coordinate system, such that the location of a specific point in the receiving aperture is given by the vector $\mathbf{r}$. The complex voltage measured by a sensor placed at this point is given by the function $r(t)$, with a complex envelope representation

$$r(t) = \Re e\left\{\tilde{r}(t)e^{j2\pi f_c t}\right\}$$

where $\tilde{r}(t)$ is the complex envelope of $r(t)$ and f_c the carrier frequency. The function $\tilde{r}(t)$ is a slowly varying time function representing the baseband modulation of the carrier.

The received signal can then be divided into its separate components as follows

$$\tilde{r}(t) = \tilde{s}_T(t) + \tilde{s}_S(t) + \tilde{s}_D(t) + \tilde{w}(t)$$

where $\tilde{s}_T(t)$, $\tilde{s}_S(t)$ and $\tilde{s}_D(t)$ are the direct, specular and diffuse components respectively while $\tilde{w}(t)$ is the ubiquitous receiver noise commonly modelled as a zero-mean, narrowband, white Gaussian process with covariance function

$$\mathrm{E}\{\tilde{w}(t)\tilde{w}^*(t+\tau)\} = \frac{N_0}{2}\delta(\tau)$$

Both the direct and specular components are well defined with respect to incoming direction, signal amplitude and phase, and can easily be modeled in deterministic terms as incoming plane waves scaled by the complex reflection coefficient ρ and appropriate propagation factors

$$\tilde{s}_T(t) = \sqrt{P_t}e^{-jkR}\frac{\lambda}{4\pi}\frac{\sqrt{G_t^{dir}G_r^{dir}}}{R}e^{-j\mathbf{k}\cdot\mathbf{r}}$$

for the direct component, where G_t^{dir}, G_r^{dir} are the transmitter/receiver antenna gains, facing the receiver/transmitter directions respectively.

$$\tilde{s}_D(t) = \sqrt{P_t}e^{-jk(R_1+R_2)}\frac{\lambda}{(4\pi)^{3/2}}\frac{\sqrt{G_t^{spe}G_r^{spe}}}{R_1R_2}\rho e^{-j\mathbf{k}'\cdot\mathbf{r}}$$

for the specular component, where G_t^{spe}, G_r^{spe} are the transmitter/receiver antenna gains, facing the specular reflection point. Note that for the direct component the 4π in the denominator is not raised to 3/2 since this is the direct path. The first phase factor in both relations, refers to the distance from the transmitter to receiver coordinate system origin, while the second, to the additional phase factor from receiver origin to sensor element.

The diffuse component on the other hand is considered to be statistical in nature. For a given direction μ, the incoming field, is taken to be the combined field from all scattering points on the surface radiating in that direction

$$\tilde{s}_D(t) = \sqrt{P_t}\frac{\lambda}{(4\pi)^{3/2}}\int e^{-jk(R_1+R_2)}\frac{\sqrt{G_tG_r}}{R_1R_2}\rho e^{-jk\mu'\cdot\mathbf{r}}d\mu' = \int b(\mu')e^{-jk\mu'\cdot\mathbf{r}}d\mu'$$

where μ' is the direction cosine vector of the wavefront incident to the receiver, related to the scattered wavevector as $\mathbf{k}_s = k\mu'$. Both R_1, R_2 and G_t, G_r are functions of μ'.

For a full characterization of the diffuse term, a complete description of $b(\mu)$ is required. Assuming that the field coming from direction μ, most likely arises fron many points independently radiating in that direction, one can model $b(\mu)$ as a complex, Gaussian, zero-mean, random variable for each μ, with covariance

$$\mathsf{E}\{b(\mu')b^*(\mu'')\} = K(\mu,\mu')\delta(\mu'-\mu'')$$

in essence, a colore noise Gaussian process. This states that radiation coming from different directions is independent, and the term $K(\mu,\mu')$ simply represents the spectral density from direction μ' for a source at μ (a weekly stationary random process is implied as well; McGarty citemgar2,mgar1 calls this the channel spread function (CSF) because it represents the signal spreading in the propagation channel due to the diffuse field.

Let $e^{j2\pi f_c t}d\mathbf{E}(\theta,\phi)$ be the diffuse field[1] coming to the sensor from the solid angle $\theta, \theta + d\theta, \phi, \phi + d\phi$ at time t. This is a random vector field with total incident power density

$$S_{in} = \frac{1}{2\eta_0}\mathsf{E}\left\{\left|\int_0^{2\pi}\int_{-\pi/2}^{\pi/2} d\mathbf{E}(\theta,\phi)\right|^2\right\}$$

where $\eta_0 = 120\pi$, is the intrinsic impedance of free space (assuming that the atmosphere above the scattering sea surface can be accurately modelled in this way).

The received power will be

$$\mathsf{E}\{|\tilde{s}_D(t)|^2\} = \int K(\mu,\mu')d\mu' = A_eS_{in} = \frac{\lambda^2}{4\pi}\frac{1}{2\eta_0}\mathsf{E}\left\{\left|\int_0^{2\pi}\int_{-\pi/2}^{\pi/2}\sqrt{G_r}d\mathbf{E}(\theta,\phi)\right|^2\right\}$$

where A_e is the effective aperture of the receiver.

[1] If the imposed time modulation is different from sinusoidal with frequency f_c the diffuse field expression should be multiplied with the modulation function.

Assuming that the scattered field is statistically independent, i.e.

$$\mathrm{E}[d\mathbf{E}^H(\theta',\phi')d\mathbf{E}(\theta,\phi)] = \begin{cases} 0 & \theta \neq \theta', \phi \neq \phi' \\ \tilde{K}(\theta,\phi)d\theta d\phi & \theta = \theta', \phi = \phi' \end{cases}$$

where the superscript H is the hermitian operator (complex conjugate transpose) and the column vector convention is followed, we have the following expression for the CSF

$$K(\mu,\mu') = \frac{\lambda^2}{4\pi}\tilde{K}(\theta,\phi)\frac{d\theta d\phi}{d\mu'}\frac{G_r}{2\eta_0}$$

B.2 Computing the channel spread function

Consider the geometry in Figures B.1 and B.2. The source of radiation (target) is at point T and the receiver is at point S. The source has power P_t transmitted through an antenna with gain $G_t(\theta^t,\phi^t)$ where θ^t and ϕ^t are the elevation and azimuth respectively defined with respect to T. The two points S and T are located over a spherical earth of radius R_E. The transmitter height is h_T and the receiver height h_R. Consider the solid angle generated from the origin S of the receiver frame, from $\theta, \theta + d\theta$ to $\phi, \phi + d\phi$, the elevation and azimuth angles respectively, defined with respect to S. This solid angle intersects the earth's surface at an area dA and it is from this area that power must be scattered, in order to be received at the sensor S.

Let $\mathbf{k}_i$ be the incident wavevector from T to dA and $\mathbf{k}_s$ the scattered wavevector, from dA to S. Define the scattering cross-section per unit area as $\sigma(\mathbf{k}_i,\mathbf{k}_s)$, the distance from S to the centre of dA as R_1, the distance from T to the centre of dA as R_2, and the distance from T to S as R.

The incident power density (W/m^2) at S is

$$\frac{P_t G_t(\theta^t,\phi^t)}{(4\pi)^2 R_1^2 R_2^2}\sigma(\mathbf{k}_i,\mathbf{k}_s)dA$$

and therefore $\tilde{K}(\theta,\phi)$, the mean-square voltage density ($V^2/m^2 \cdot sr$), is given by

$$\tilde{K}(\theta,\phi) = 2\eta_0\frac{P_t G_t(\theta^t,\phi^t)}{(4\pi)^2 R_1^2 R_2^2}\sigma(\mathbf{k}_i,\mathbf{k}_s)\frac{dA}{d\theta d\phi}$$

where $G_t(\theta^t,\phi^t)$ is the transmitter gain looking into the direction of dA. The CSF becomes then

$$K(\mu,\mu') = P_t\frac{\lambda^2}{(4\pi)^3}\frac{G_t(\theta^t,\phi^t)G_r(\theta,\phi)}{R_1^2 R_2^2}\sigma(\mathbf{k}_i,\mathbf{k}_s)\frac{dA}{d\theta d\phi}\frac{d\theta d\phi}{d\mu'} \tag{B.1}$$

where $G_r(\theta,\phi)$ is the receiver gain looking into the direction of dA. Note that the individual factors in CSF above are functions of receiver, transmitter and scattering frame coordinates. Therefore, we will first need to find the relations between the different coordinate systems.

Coordinate transformations

Consider again Fig. B.1 depicting the scattering geometry. Let O, S, T and C be the origins of the coordinate frames of the earth's centre, the receiver sensor, the transmitter (source/target) and the

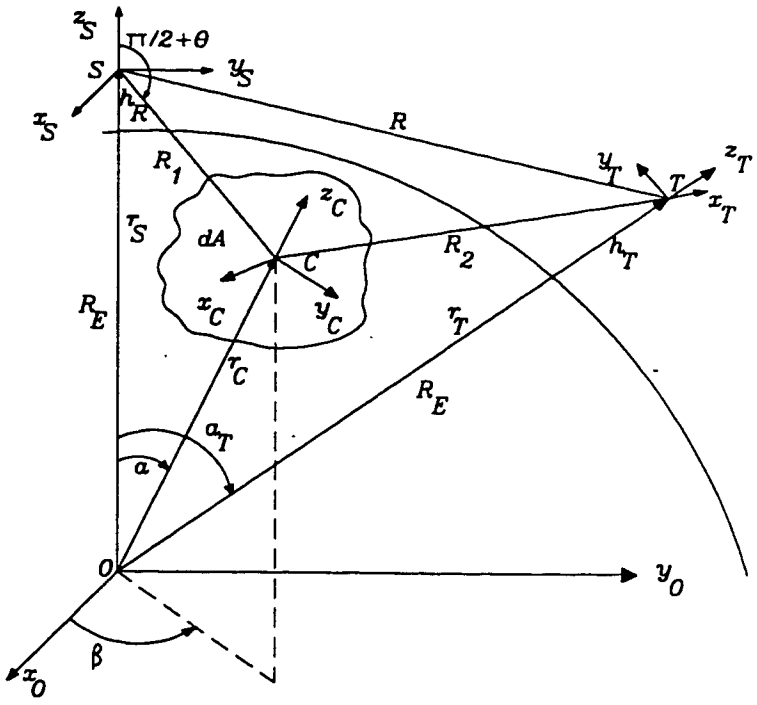

Figure B.1: The scattering geometry with the four frames of reference involved. Transmitter frame T, receiver(sensor) frame S, scattering frame C, and centre of earth frame O. The antenna gains G_t, G_r are always referred to the transmitter and receiver frame respectively. The azimuth angle ϕ (frame S) is equal to the azimuth angle β (frame O).

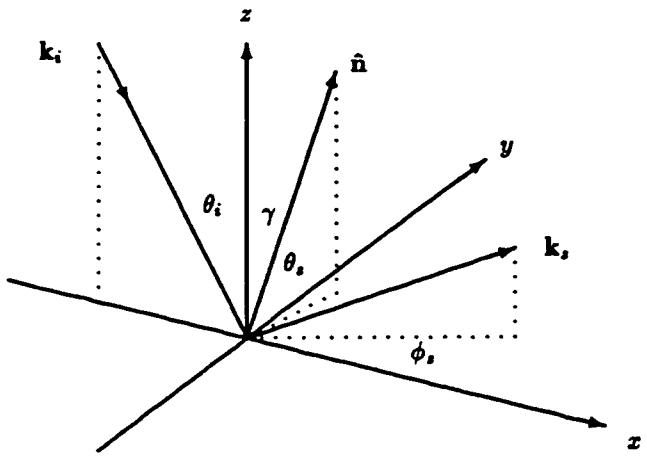

Figure B.2: The local scattering geometry at the centre of dA. It is further assumed that the source point T lies in the xz plane towards the negative x-axis. $\hat{\mathbf{n}}$ is the local surface normal of the specular point while the z-axis is parallel to the local normal on dA.

scattering frame respectively. The problem to be solved can be stated as follows: *How can we express the scattering frame incidence and scattering angles θ_i, θ_s and ϕ_s, as well as the transmitter azimuth and elevation angles ϕ^t and θ^t as a function of the receiver "look" direction (θ, ϕ) and the known lengths h_R (receiver height), h_T (transmitter height), R_E (earth radius) and R (receiver–transmitter distance) ?*

The receiver "look" direction (θ, ϕ) defines a unit vector

$$\hat{\mathbf{v}} = (\cos\theta\cos\phi, \cos\theta\sin\phi, \sin\theta)$$

From standard analytic geometry this defines a parametric representation (with parameter q) of a three-dimensional line in space that intersects the earth sphere at a point (x, y, z) satisfying in O frame coordinates:

$$\begin{aligned} x^2 + y^2 + z^2 &= R_E^2 \\ x &= q\cos\theta\cos\phi \\ y &= q\cos\theta\sin\phi \\ z &= (R_E + h_R) + q\sin\theta \end{aligned}$$

The distance R_1 can now be computed and the angle α can be found from the modified cosine law[2].

---

[2] $$a^2 + (a+h)^2 - 2a(a+h)\cos\phi = h^2 + 4a(a+h)\sin^2\frac{\phi}{2}$$

to avoid the computational problem of subtracting two nearly equal large numbers.

Let us define in earth centre coordinates the vectors

$$\begin{aligned}
\mathbf{r}_C &= R_E(\sin\alpha\cos\phi, \sin\alpha\sin\phi, \cos\alpha) \\
\mathbf{r}_S &= (R_E + h_R)(0, 0, 1) \\
\mathbf{r}_T &= (R_E + h_T)(0, \sin\alpha_T, \cos\alpha_T) \\
\mathbf{R}_1 &= \mathbf{r}_S - \mathbf{r}_C \\
\mathbf{R}_2 &= \mathbf{r}_T - \mathbf{r}_C \\
\mathbf{R} &= \mathbf{r}_S - \mathbf{r}_T
\end{aligned}$$

where we used the fact that $\beta = \phi$ and $\beta_T = \pi/2$ in earth centre coordinates.

The scattering frame incidence and elevation scattering angles can be computed from

$$\cos\theta_i = \hat{\mathbf{R}}_2 \cdot \hat{\mathbf{r}}_C \qquad \text{and} \qquad \cos\theta_s = \hat{\mathbf{R}}_1 \cdot \hat{\mathbf{r}}_C$$

where $\hat{}$ indicates the unit vector of the quantity underneath. The scattering frame basis vectors can be expressed as

$$\begin{aligned}
\hat{\mathbf{x}}_C &= (\hat{\mathbf{R}}_2 \times \hat{\mathbf{r}}_C) \times \hat{\mathbf{r}}_C \\
\hat{\mathbf{y}}_C &= \hat{\mathbf{R}}_2 \times \hat{\mathbf{r}}_C \\
\hat{\mathbf{z}}_C &= \hat{\mathbf{r}}_C
\end{aligned}$$

which, considering

$$\mathbf{R}_1 = R_1(\sin\theta_s\cos\phi_s, \sin\theta_s\sin\phi_s, \cos\theta_s)$$

gives us

$$\tan\phi_s = \frac{\hat{\mathbf{R}}_1 \cdot \hat{\mathbf{y}}_C}{\hat{\mathbf{R}}_1 \cdot \hat{\mathbf{x}}_C}$$

Similarly, the transmitter frame basis vectors are

$$\begin{aligned}
\hat{\mathbf{x}}_T &= \hat{\mathbf{R}} \times \hat{\mathbf{r}}_T \\
\hat{\mathbf{y}}_T &= \hat{\mathbf{r}}_T \times (\hat{\mathbf{R}} \times \hat{\mathbf{r}}_T) \\
\hat{\mathbf{z}}_T &= \hat{\mathbf{r}}_T
\end{aligned}$$

The elevation angle of the transmitter, measured from the z_T-axis, can then be obtained from

$$\theta^t = 180^\circ - \cos^{-1}(\hat{\mathbf{R}}_2 \cdot \hat{\mathbf{z}}_T)$$

and the azimuth angle, measured from the x_T-axis

$$\phi^t = 180^\circ + \tan^{-1}\left(\frac{\mathbf{R}_2 \cdot \hat{\mathbf{y}}_T}{\mathbf{R}_2 \cdot \hat{\mathbf{x}}_T}\right)$$

Note that the transmitter boresight is the y_T axis.

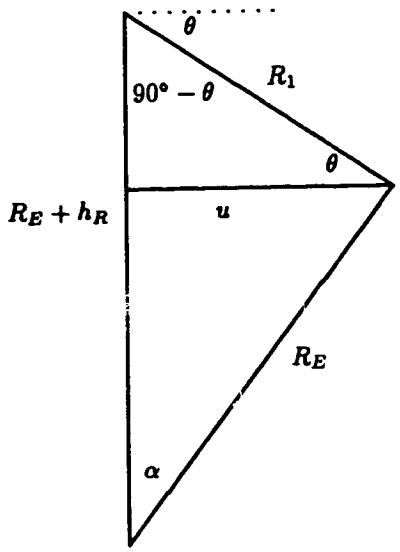

Figure B.3: A closer look at the triangle defining the relationship between incidence and scattering angles and lengths.

The Jacobian $dA/d\theta d\phi$

This term basically relates the changes in the incremental surface area dA to the solid angle that generates it. McGarty [81] gives a general formula (equation 24 in his paper) from which he derives the final form of the Jacobian (equation 25 in his paper). I could not personally derive his general formula and I do not see how he can go from it to the final expression he gives. An independent derivation (Fig. B.3) however, does give the same final result.

The surface area is given by

$$dA = u d\phi R_E d\alpha$$

where $u = R_E \sin\alpha$ and the "trick" lies in expressing properly $d\alpha$ as a function of $d\theta$. Notice that R_1, θ and α can all change interdependently while only R_E and h_R remain constant. One should therefore start from

$$\tan\theta = \frac{R_E + h_R - R_E\cos\alpha}{R_E \sin\alpha}$$

differentiate, to obtain the relationship between $d\alpha$ and $d\theta$, and substituting into dA arrive finally at the Jacobian

$$\frac{dA}{d\theta d\phi} = \left| \frac{R_1^2 \sin\alpha}{1 - \cos\alpha(1 + h_R/R_E)} \right|$$

B.3 The linear array receiver

The scattering cross-section per unit area $\sigma(\mathbf{k}_i, \mathbf{k}_s)$ is the term that contains all the purely scattering information that depend on surface structure and properties, including the incident and scattered

polarization of the field. Before using explicit expressions from theory, let us first consider the information we can get from a linear array receiver similar to the one used for our experimental data collection.

With an array receiver, the total demodulated signal is represented by the output of M sensors located at positions $\mathbf{r}_i$, $i = 1, 2, \ldots M$. By introducing the $M \times 1$ delay vector $\mathbf{d}(\mu)$ given by

$$\mathbf{d}(\mu) = \begin{bmatrix} \exp(-jk\mu \cdot \mathbf{r}_1) \\ \exp(-jk\mu \cdot \mathbf{r}_2) \\ \vdots \\ \exp(-jk\mu \cdot \mathbf{r}_M) \end{bmatrix}$$

the total array output in vector form, normalized to the direct component, is given by

$$\tilde{\mathbf{r}} = \mathbf{d}(\mu) + \rho \frac{R}{\sqrt{4\pi} R_1 R_2} e^{-jk(R_1+R_2-R)} \sqrt{\frac{G_t^{spe} G_r^{spe}}{G_t^{dir} G_r^{dir}}} \mathbf{d}(\mu') + \mathbf{b} + \mathbf{w} \tag{B.2}$$

where $\mathbf{w}$ is an $M \times 1$ zero-mean Gaussian random vector with covariance $\mathbf{K}_w = \sigma_w^2 \mathbf{I}$ and the components of $\mathbf{b}$ are

$$b_i = \frac{4\pi R}{\lambda \sqrt{P_t} \sqrt{G_t^{dir} G_r^{dir}}} \int b(\mu') d_i(\mu') d\mu' \tag{B.3}$$

where $d_i(\mu) = \exp(-jk\mu \cdot \mathbf{r}_i)$.

Let us consider the voltage v_i which is the ith element of $\tilde{\mathbf{r}}$ above

$$v_i = d_i(\mu) + \tilde{\rho} d_i(\mu') + b_i + w_i \tag{B.4}$$

where the expression for $\tilde{\rho}$ can be found from (B.2) above by inspection. The autocorrelation function of this relation is

$$R_v(\ell) = \mathsf{E}[v_i^* v_{i+\ell}] = d_i^*(\mu) d_{i+\ell}(\mu) + |\tilde{\rho}|^2 d_i^*(\mu') d_{i+\ell}(\mu') + \mathsf{E}[b_i^* b_{i+\ell}] + \mathsf{E}[w_i^* w_{i+\ell}]$$

where we take into account all possible lags ℓ. We also assume that the zero-mean random variables b_i and w_i are independent, otherwise the cross correlation terms can make the process v_i non-stationary (see, e.g. [51]).

Let us express the μ vector as a function of θ and ϕ, which expression is

$$\mu = -(\cos\theta \cos\phi, \cos\theta \sin\phi, \sin\theta)$$

Note that a positive θ corresponds to directions above the xy-plane while the opposite holds true for negative θ.

The position vector $\mathbf{r}_i$ is

$$\mathbf{r}_i = -d_e \left[i - \frac{M+1}{2} \right] \hat{\mathbf{z}}$$

where d_e is the array interelement spacing and $i = 1, 2, \ldots M$, the number of array elements. Note that we have used as reference the array centre. Note also that $i = 1$ corresponds to the top array

element in the positive z-direction. We can then express the dot product of μ and the position vector as

$$k\mu \cdot \mathbf{r}_i = kd_e \sin\theta \left[i - \frac{M+1}{2}\right] = 2\pi\kappa \left[i - \frac{M+1}{2}\right]$$

where we have defined the independent variable of the wavenumber spectrum as

$$\kappa = \frac{d_e}{\lambda} \sin\theta \tag{B.5}$$

Let us now assume for simplicity that the index i is continuous and that $i-(M+1)/2$ takes values from $-\infty$ to $+\infty$. We then have

$$d_i^*(\mu) d_{i+\ell}(\mu) = e^{-j2\pi\kappa\ell}$$

The wavenumber spectrum (the Fourier transform of the autocorrelation function) becomes then

$$S_v(\kappa) = \begin{cases} \delta(\kappa - \kappa_T) + |\tilde{\rho}|^2 \delta(\kappa - \kappa_S) + \sigma_w^2 + \\ \\ \dfrac{1}{P_t}\left(\dfrac{4\pi R}{\lambda}\right)^2 \dfrac{1}{G_t^{dir} G_r^{dir}} \displaystyle\int_\ell \left[\int_{\mu'} K(\mu,\mu') e^{-j2\pi\kappa_D \ell} d\mu'\right] e^{j2\pi\kappa\ell} d\ell \end{cases}$$

where the subscripts T, S and D refer to the target(direct), specular and diffuse components respectively.

Interchanging the integration order we can simplify the last integral as follows

$$\int_{\mu'} d\mu' K(\mu,\mu') \left[\int_\ell e^{j2\pi(\kappa-\kappa_D)\ell} d\ell\right] = \int_{\mu'} d\mu' K(\mu,\mu') \delta(\kappa - \kappa_D)$$

and by substituting the CSF expression (B.1) and simplifying, the diffuse spectrum expression becomes

$$S_D(\kappa_D) = \frac{R^2}{4\pi G_t^{dir} G_r^{dir}} \int_{\phi=0}^{\pi} \frac{G_t G_r}{R_2^2} \sigma(\mathbf{k}_i, \mathbf{k}_s) \left| \frac{\sin\alpha}{1 - \cos\alpha(1 + h_R/R_E)} \right| d\phi \tag{B.6}$$

where κ_D corresponds to all the possible diffuse component directions-of-arrival (i.e. the angles θ that result in a non-zero integrand). The total diffuse power is given by

$$P_{dif} = \int_{-\pi/2}^{\theta_{max}} S_D(\kappa_D) d\theta$$

where $\theta = -\pi/2$ corresponds to the receiver base and $\theta = \theta_{max}$ to the transmitter base or horizon.

Wrapping

In (B.5) we defined the independent variable of the wavenumber spectrum. When the physical angle of elevation θ varies in $[-\pi/2, \pi/2]$, κ varies correspondingly in $[-d_e/\lambda, d_e/\lambda]$. If $d_e/\lambda \leq 0.5$ we have a 1–to–1 mapping between θ and κ and the wavenumber power spectrum is straightforward, in principle, to compute. If, however, $d_e/\lambda > 0.5$, the mapping is no longer 1–to–1. The factor κ

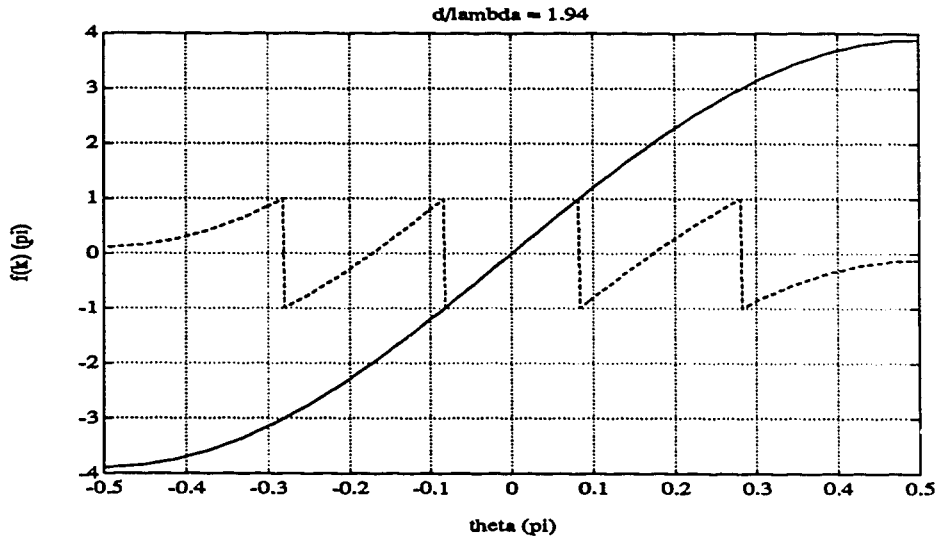

Figure B.4: The function $2\pi\kappa$, for θ in $[-\pi/2, \pi/2]$, for the case $d_e/\lambda = 1.94$.

is analogous to the normalized sampling frequency in an ordinary Fourier transform, and $\kappa > 0.5$ means undersampling, which leads to aliasing). E.g. in Fig. B.4 we see the case of $d_e/\lambda = 1.94$. Both the unwrapped (solid) and wrapped (dashed) mappings are shown. The power spectrum computed for this case will be a function of the wrapped κ. As we can see from the graph, the unambiguous field of view will be $\kappa \in [-1/2, 1/2]$ corresponding to $|\theta| \leq 14.9°$. The four other 1-to-1 segments are wrapped around the principal interval $[-1/2, 1/2]$. If we are only given the final wrapped result and no other a priori information, it is impossible to implement unwrapping. Starting however from a given model, the wrapping/unwrapping procedure is relatively straightforward. In fact, it is better to take each segment separately and perform the convolutions with the array factor, with FFT's (the CPU time saving can be enormous). The individual results are then added together in the appropriate wavenumber interval and this also takes care of the wrapping.

Grating lobes

With $d_e/\lambda > 0.5$ grating lobes appear [5]. As an example, for the case $d_e/\lambda = 1.94$ and $M = 32$ there are (Fig. B.5) three grating lobes appearing in the array factor. This gives us the array response for a plane wave impinging from angle θ. Note that for more accurate results the directional patterns of the transmitter and receiver pyramidal horns has to be taken into account. In fact, improvement is observed, both for the grating lobe and tail-end behaviour. The standard gain horn patterns were calculated from [5, pages 565-576]). Even though no diffraction effects are included in these formulas and their derivation considers the pyramidal horn as an aperture antenna mounted on an infinite ground plane, they give accurate enough results for the purposes required here. The final receiver

response will be the convolution of the theoretical diffuse spectrum in (B.6) with the array factor in Fig. B.5.

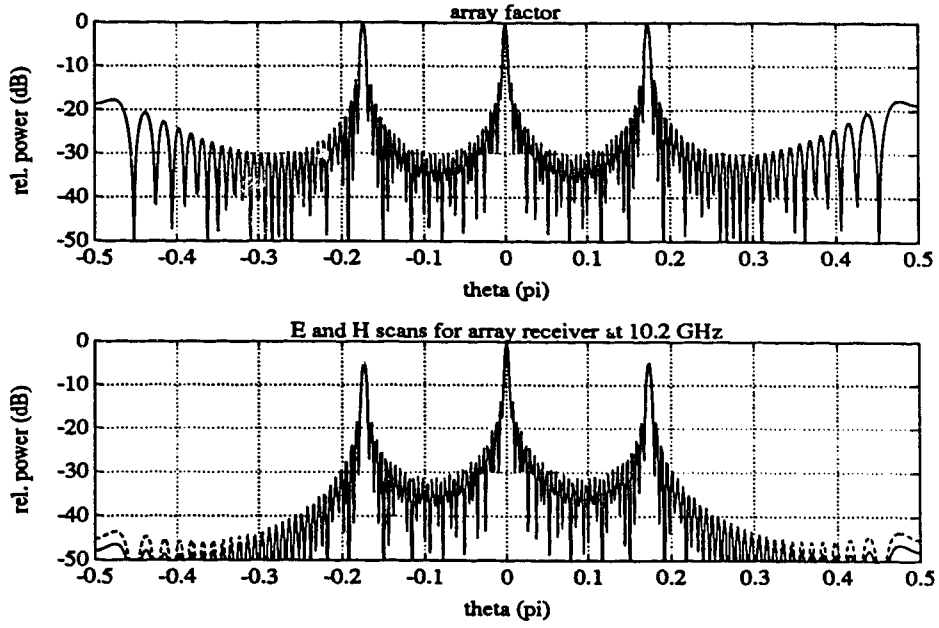

Figure B.5: The array factor for a 32 element linear array when $d_e/\lambda = 1.94$ as a function of θ (top graph). When the field pattern of the pyramidal horn elements is taken into account, this is modified to the bottom graph. E scan solid, H scan dashed.

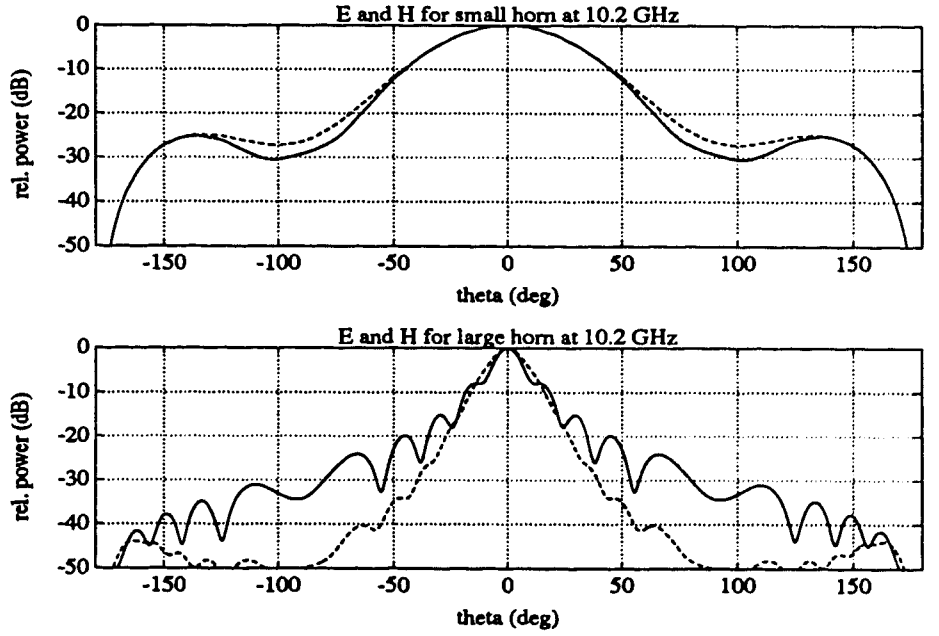

Figure B.6: The E(solid) and H(dashed) field patterns of the small and large horns used in the lake Huron experiments at 10.2 GHz.

Bibliography

[1] M. Abramowitz and I.A. Stegun. *Handbook of Mathematical Functions.* Dover Publications, Inc., New York, 1972.

[2] J.R. Apel. Electromagnetics and the sea. In *Principles of Ocean Physics*, chapter 8. Academic Press, 1987.

[3] B.C. Armstrong and H.D. Griffiths. Modelling spatially correlated K-distributed clutter. *Electronics Letters*, 27:1355–1356, 1991.

[4] R.M Axline and A.K. Fung. Numerical computations of scattering from a perfectly conducting random surface. *IEEE Trans. Ant. Prop.*, AP-26:482–488, 1978.

[5] C.A. Balanis. *Antenna Theory: Analysis and Design.* Harper and Row, New York, 1982.

[6] D.E. Barrick. Rough surface scattering based on the specular point theory. *IEEE Trans. Ant. Prop.*, AP-16:449–454, 1968.

[7] D.E. Barrick. Theory of HF and VHF propagation across the rough sea, 2, Application to HF and VHF propagation above the sea. *Radio Science*, 6:527–533, 1971.

[8] D.E. Barrick. First order theory and analysis of MF/HF/VHF scatter from the sea. *IEEE Trans. Ant. Prop.*, AP-20:2–10, 1972.

[9] D.E. Barrick and E. Bahar. Rough surface scattering using specular point theory. *IEEE Trans. Ant. Prop.*, AP-29:798–800, 1981.

[10] H. Bartelt, A.W. Lohmann, and B. Wirnitzer. Phase and amplitude recovery from bispectra. *Applied Optics*, 23:3121–3129, 1984.

[11] D.K. Barton. Low-angle radar tracking. *Proc. IEEE*, 62:687–704, 1974.

[12] D.K. Barton. Low-angle tracking. *Microwave Journal*, pages 19–24, December 1976.

[13] F.G. Bass and I.M. Fuks. *Wave scattering from statistically rough surfaces.* Pergamon Press, 1979.

[14] P. Beckmann. Shadowing of random rough surfaces. *IEEE Trans. Ant. Prop.*, AP-13:384–388, 1965. (see comment in AP-14 (1966) pp. 253).

[15] P. Beckmann. *The Depolarization of Electromagnetic Waves.* The Golem Press, Boulder, Colorado, 1968.

[16] P. Beckmann and A. Spizzichino. *The Scattering of Electromagnetic Waves from Rough Surfaces.* Pergammon Press, 1963. (Reprinted by Artech House in 1987).

[17] P.M. van den Berg and A.T. de Hoop. Reflection and transmission of electromagnetic waves at a rough interface between two different media. *IEEE Trans. Geoscience and Remote Sensing*, GE-22:42–52, 1984.

[18] A.J. Blanchard and B.R. Jean. Antenna effects in depolarization measurements. *IEEE Trans. Geosc. Rem. Sens.*, GE-21:113–117, 1983.

[19] A.J. Blanchard, R.W. Newton, and B.R. Jean. Amplitude and phase errors involved in retrieving depolarized radar cross section measurements. *IEEE Trans. Geosc. Rem. Sens.*, GE-21:314–319, 1983.

[20] W.M. Boerner, M.B. El-Arini, C.Y. Chan, and P.M. Mastoris. Polarization dependence in electromagnetic inverse problems. *IEEE Trans. Ant. Prop.*, AP-29:262–271, 1981.

[21] D.R. Brillinger. An introduction to polyspectra. *Ann. Math. Statist.*, 36:1351–1374, 1965.

[22] R.A. Brockelman and T. Hagfors. Note on the effect of shadowing on the backscattering of waves from a random rough surface. *IEEE Trans. Ant. Prop.*, AP-14:621–629, 1966.

[23] T.P. Bronez. Personal communication.

[24] G.S. Brown. A comparison of approximate theories for scattering from rough surfaces. *Wave Motion*, 7:195–205, 1985.

[25] H.L. Chan and A.K. Fung. A numerical study of the Kirchhoff approximation in horizontally polarized backscattering from a random surface. *Radio Science*, 13:811–818, 1978.

[26] A.D. Chave, D.J. Thomson, and M.E. Ander. On the robust estimation of power spectra, coherences, and transfer functions. *J. Geophys. Res.*, 92(B1):633–648, 1987.

[27] J.S. Chen and A. Ishimaru. Numerical simulation of the second-order Kirchhoff approximation from very rough surfaces and a study of backscattering enhancement. *J. Acoust. Soc. Am.*, 88:1846–1850, 1990.

[28] K.S. Chen and A.K. Fung. A scattering model for ocean surface. In *IEEE International Conference of the International Geographic and Remote Sensing Society (IGARSS)*, pages 1251–1254, 1991.

[29] W.C. Chew. *Waves and Fields in Inhomogeneous Media.* Van Nostrand Reinhold, 1990.

[30] S.K. Cho. *Electromagnetic Scattering.* Springer-Verlag, New York, 1990.

[31] C. Cox and W. Munk. Slopes of the sea surface deduced from photographs of sun glitter. *Bulletin, Scripts Institute of Oceanography,* 6:401–488, 1956.

[32] C. Cox and W.H. Munk. Measurement of the roughness of the sea from photographs of the sun's glitter. *J. Opt. Soc. Amer.,* 44:838–850, 1954.

[33] E. D'Addio, S. Giannatempo, and G. Galati. Generation of K-distributed random variables. *Trans. of the Soc. for Computer Simulations,* 5:159–174, 1988.

[34] J.D. DeLorenzo and E.S. Cassedy. A study of the mechanism of sea surface scattering. *IEEE Trans. Ant. Prop.,* AP-14:611–620, 1966.

[35] R. Devayya and D.J. Wingham. The numerical calculation of rough surfcae scattering by the conjugate gradient method. *IEEE Trans. on Geoscience and Remote Sensing,* 30:645–648, 1992.

[36] M.A. Donelan and W.J. Pierson, Jr. Radar scattering and equilibrium ranges in wind-generated waves with application to scatterometry. *J. Geophys. Res.,* 92(C5):4971–5029, 1987.

[37] A. Drosopoulos. Lake Huron 1987: Experimental data description and calibration. Technical Report CRL No. 256, Communications Research Laboratory, McMaster University, Ontario, 1992.

[38] A. Drosopoulos and S. Haykin. Angle-of-arrival estimation in presence of multipath. *Electronics Letters,* 27:2273–2274, 1991.

[39] A. Drosopoulos and S. Haykin. Adaptive radar parameter estimation with Thomson's multiple-window method. In S. Haykin and A. Steinhardt, editors, *Adaptive Radar Detection and Estimation,* chapter 7. Wiley, 1992.

[40] A. Drosopoulos and S. Haykin. Bearing estimation in a colored noise background using the method of multiple windows. In *IEEE International Conference on Acoustics, Speech and Signal Processing, ICASSP-92,* volume 5, pages 385–388, 1992.

[41] C. Eftimiu. First-order Wiener-Hermite expansion in the electromagnetic scattering by conducting rough surfaces. *Radio Science,* 23:769–779, 1988.

[42] C. Eftimiu. Second-order Wiener-Hermite expansion in the electromagnetic scattering by conducting rough surfaces. *Radio Science,* 23:1075–1084, 1988.

[43] A.K. Fung. Mechanisms of polarized and depolarized scattering from a rough dielectric surface. *J. of the Franklin Inst.,* 285:125–133, 1968.

[44] A.K. Fung and H.L. Chan. Backscattering of waves by composite rough surfaces. *IEEE Trans. Ant. Prop.*, AP-17:590–597, 1969.

[45] A.K. Fung and K.S. Chen. Kirchhoff model for a skewed random surface. *J. Electromagnetic Waves and Applications*, 5:205–216, 1991.

[46] A.K. Fung and M.F. Chen. Numerical simulation of scattering from simple and composite random surfaces. *J. Opt. Soc. Am. A*, 2:2274–2284, 1985.

[47] A.K. Fung and H.J. Eom. Multiple scattering and depolarization by a randomly rough Kirchhoff surface. *IEEE Trans. Ant. Prop.*, AP-29:463–471, 1981.

[48] G.M. Gallatin. Functional-integral representation of rough surfaces. *J. Opt. Soc. Am. A*, 8:97–104, 1991.

[49] R.E. Glazman. Near-nadir radar backscatter from a well-developed sea. *Radio Science*, 25:1211–1219, 1990.

[50] K. Hasselmann, W. Munk, and G. MacDonald. Bispectra of ocean waves. In M. Rosenblatt, editor, *Proceedings of the Symposium of Time Series Analysis*, chapter 8. John Wiley, 1963.

[51] S. Haykin, Ed. *Array Signal Processing, Chapter 4*, S. Haykin, *Radar Array Processing for Angle of Arrival Estimation.* Prentice-Hall, 1985.

[52] D. Holliday, G. St-Cyr, and N.E. Woods. A radar ocean imaging model for small to moderate incidence angles. *Int. J. Remote Sensing*, 7:1809–1834, 1986.

[53] D. Holliday, G. St-Cyr, and N.E. Woods. Comparison of a new radar ocean imaging model with SARSEX internal wave image data. *Int. J. Remote Sensing*, 8:1423–1430, 1987.

[54] X.Y. Hou and N. Morinaga. Detection performance in K-distributed and correlated Rayleigh clutter. *IEEE Trans. Aerospace and Electronic Systems*, AES-25:634–641, 1989.

[55] A. Ishimaru and J.S. Chen. Scattering from very rough surfaces based on the modified Kirchhoff approximation with angular and propagation shadowing. *J. Acoust. Soc. Am.*, 88:1877–1883, 1990.

[56] K. Ivanova, M.A. Michalev, and O.I. Yordanov. Study of the Phase Perturbation Technique for Scattering of Waves by Rough Surfaces at Intermediate and Large Values of the Roughness Parameter. *J. of Electromagnetic Waves and Applications*, 4:401–404, 1990.

[57] E. Jakeman and P.N. Pusey. Non-Gaussian fluctuations in electromagnetic radiation scattered by a random phase screen. I. Theory. *J. Phys. A: Math. Gen.*, 8:369–391, 1975.

[58] E. Jakeman and P.N. Pusey. Non-Gaussian fluctuations in electromagnetic radiation scattered by a random phase screen. II. Application to dynamic scattering in a liquid crystal. *J. Phys. A: Math. Gen.*, 8:392–410, 1975.

[59] E. Jakeman and P.N. Pusey. A model for non-Rayleigh sea echo. *IEEE Trans. Ant. Prop.*, AP-24:806–814, 1976.

[60] E. Jakeman and R.J.A. Tough. Generalized K distribution: A statistical model for weak scattering. *J. Opt. Soc. Am. A*, 4:1764–1772, 1987.

[61] E. Jakeman and R.J.A. Tough. Non-Gaussian models for the statistics of scattered waves. *Advances in Physics*, 37:471–529, 1988.

[62] W.C. Keller and J.W. Wright. Microwave scattering and the straining of wind-generated waves. *Radio Science*, 10:139–147, 1975.

[63] D.E. Kerr, Ed. *Propagation of Short Radio Waves. M.I.T. Radiation Laboratory Series, vol. 13.* McGraw-Hill, 1951.

[64] V. Kezys. Multi-frequency angle-of-arrival estimation: An experimental evaluation. *Proc. SPIE, Advanced Algorithms and Architectures for Signal Processing III*, 975:93–100, 1988.

[65] B. Kinsman. *Wind Waves.* Englewood Cliffs, N.J., 1963. (Reprinted by Dover in 1984).

[66] G.J. Klinker, S.A. Shafer, and T. Kanade. Using a color reflection model to separate highlights from object color. In *Proc. of the First International Conference on Computer Vision*, pages 145–150, 1987.

[67] R.D. Kodis. A note on the theory of scattering from an irregular surface. *IEEE Trans. Ant. Prop.*, AP-14:77–82, 1966.

[68] J.A. Kong. *Electromagnetic Wave Theory.* John-Wiley, 1986.

[69] J.C. Leader. Bidirectional scattering of electromagnetic waves from rough surfaces. *J. Appl. Phys.*, 42:4808–4816, 1971.

[70] J.C. Leader. An analysis of the spatial coherence of laser light scattered from a surface with two scales of roughness. *J. Opt. Soc. Am.*, 66:536–546, 1976.

[71] J.C. Leader. Incoherent backscatter from rough surfaces: The two-scale model reexamined. *Radio Science*, 13:441–457, 1978.

[72] R.R Lentz. A numerical study of electromagnetic scattering from ocean-like surfaces. *Radio Science*, 9:1139–1146, 1974.

[73] T. Lo and J. Litva. Use of a highly deterministic multipath signal model in low-angle tracking. *Proc. IEE-F*, 138:163–171, 1991.

[74] M.W. Long. *Radar Reflectivity of Land and Sea.* Artech House, 1983.

[75] M.S. Longuet-Higgins. The statistical analysis of a random, moving surface. *Phil. Trans. Royal Soc. A*, 249:321–387, 1957.

[76] M.S. Longuet-Higgins. Statistical properties of an isotropic random surface. *Phil. Trans. Royal Soc. A*, 250:157–174, 1957.

[77] M.S. Longuet-Higgins. The effect of non-linearities on statistical distributions in the theory of sea waves. *J. Fluid Mech.*, 17:459–480, 1963.

[78] M.S. Longuet-Higgins. On the skewness of sea surface slopes. *J. Physical Oceanography*, 12:1283–1291, 1982.

[79] P.J. Lynch and R.J. Wagner. Rough-surface scattering: Shadowing, multiple scatter and energy conservation. *J. Math. Physics*, 11:3032–3042, 1970.

[80] H. Masuko, K. Okamoto, M. Shimada, and S. Niwa. Measurement of microwave backscattering signatures of the ocean surface using X band and K_a band airborne scatterometers. *J. Geophys. Res.*, 91(C11):13065–13083, 1986.

[81] T.P. McGarty. Antenna performance in the presence of diffuse multipath. *IEEE Trans. Aerospace and Electronic Systems*, AES-12:42–54, 1976.

[82] Yu.V. Mel'nichuk and A.A. Chernikov. Spectra of radar signals from sea surface for different polarizations. *Atmospheric and Oceanic Physics*, 7:17–24, 1971.

[83] J.M. Mendel. Tutorial on Higher-Order Statistics (Spectra) in Signal Processing and System Theory: Theoretical Results and Some Applications. *Proc. IEEE*, 79:278–305, 1991.

[84] R.L. Mitchell. *Radar Signal Simulation.* Artech House, 1976.

[85] K.M. Mitzner. Change in polarization on reflection from a tilted plane. *Radio Science*, 1:27–29, 1966.

[86] A.V. Mrstik and P.G. Smith. Multipath limitations on low-angle radar tracking. *IEEE Trans. Aerospace and Electronic Syst.*, AES-14:85–102, 1978.

[87] S. Mudaliar and J.K. Lee. Microwave scattering and emission from a half-space anisotropic random medium. *Radio Science*, 25:1199–1210, 1990.

[88] F.E Nathanson, J.P. Reilly, and M.N. Cohen. *Radar Design Principles.* McGraw-Hill, New York, 2nd edition, 1991.

[89] R.J. Nelson and A.J. Blanchard. The effect of system parameters on the quality of polarized and depolarized bistatic radar cross section measurements. *Remote Sens. Environ.*, 27:187–199, 1989.

[90] M. Nieto-Vesperinas. Depolarization of electromagnetic waves scattered from slightly rough random surfaces: A study by means of the extinction theorem. *J. Opt. Soc. Am.*, 72:539–547, 1982.

[91] M. Nieto-Vesperinas. Radiometry of rough surfaces. *Optica Acta*, 29:961–971, 1982.

[92] M. Nieto-Vesperinas and N. Garcia. A detailed study of the scattering of scalar waves from random rough surfaces. *Optica Acta*, 28:1651–1672, 1981.

[93] M. Nieto-Vesperinas and J.M. Soto-Crespo. Monte Carlo simulations for scattering of electromagnetic waves from perfectly conductive random rough surfaces. *Optics Letters*, 12:979–981, 1987.

[94] C.L. Nikias and M.R. Raghuveer. Bispectrum estimation: A digital signal processing framework. *Proc. IEEE*, 75:869–891, 1987.

[95] T. Nohara and S. Haykin. Canadian east coast radar trials and the K-distribution. *IEE Proc. F*, 138:80–88, 1991.

[96] K.A. O'Donnell and E.R. Mendez. Experimental study of scattering from characterized random surfaces. *J. Opt. Soc. Am. A*, 4:1194–1205, 1987.

[97] J.A. Ogilvy. *Theory of Wave Scattering from Random Rough Surfaces.* Adam-Hilger, Bristol, Philadelphia and New York, 1991.

[98] C.J. Oliver. Correlated K-distributed clutter models. *Optica Acta*, 32:1515–1547, 1985.

[99] C.J. Oliver and R.J.A. Tough. On the simulation of correlated K-distributed random clutter. *Optica Acta*, 33:223–250, 1986.

[100] A. Papoulis. *Probability, Random Variables and Stochastic Processes.* McGraw-Hill, 2nd edition, 1984.

[101] O.M. Phillips. *The dynamics of the upper ocean.* Cambridge University Press, 2nd edition, 1977.

[102] W.J. Plant and W.C. Keller. Evidence of Bragg scattering in microwave Doppler spectra of sea return. *J. Geophys. Res.*, 95(C9):16299–16310, 1990.

[103] W.H. Press, B.P. Flannery, S.A. Teukolsky, and W.T. Vetterling. *Numerical Recipes.* Cambridge University Press, 1986.

[104] R.S. Raghavan. Adaptive processing of microwave sea echo for the suppression of strong reflections from scatterers. *IEEE J. Oceanic Eng.*, 14:76–83, 1989.

[105] M.R. Raghuveer and C.L. Nikias. Bispectrum estimation: A parametric approach. *IEEE Trans. Acoust., Speech, Signal Processing*, ASSP-33:1213–1230, 1985.

[106] T.S. Rao and M.M. Gabr. *An Introduction to Bispectral Analysis and Bilinear Time Series Models.* Springer-Verlag, 1984.

[107] G. Rasigni, M. Rasigni, J. Palmari, C. Dussert, and F. Varnier. Statistical parameters for random and pseudorandom rough surfaces. *J. Opt. Soc. Am. A*, 5:99–103, 1988.

[108] M.I. Sancer. An analysis of the vector Kirchhoff equations and the associated boundary-line charge. *Radio Science*, 3:141–144, 1968.

[109] M.I. Sancer. Shadow-corrected electromagnetic scattering from a randomly rough surface. *IEEE Trans. Ant. Prop.*, AP-17:577–585, 1969.

[110] D. Slepian. Some asymptotic expansions for prolate spheroidal wave functions. *J. Math. and Phys.*, 44:99–140, 1965.

[111] D. Slepian. A numerical method for determining the eigenvalues and eigenfunctions of analytic kernels. *SIAM J. Numerical Analysis*, 5:586–600, 1968.

[112] D. Slepian. Prolate Spheroidal Wave Functions, Fourier Analysis, and Uncertainty — V: The Discrete Case. *Bell Syst. Tech. J.*, 57:1371–1430, 1978.

[113] D. Slepian and E. Sonnenblick. Eigenvalues associated with prolate spheroidal functions of zero order. *Bell Syst. Tech. J.*, 44:1745–1760, 1965.

[114] B.G. Smith. Geometrical shadowing of a random rough surface. *IEEE Trans. Ant. Prop.*, AP-15:668–671, 1967.

[115] A.W. Straiton and C.W. Tolbert. Measurements and analysis of instantaneous radio height-gain curves at 8.6 millimeters over rough surfaces. *IRE Trans. Ant. Prop.*, AP-4:346–351, 1956.

[116] C.T. Tai. *Dyadic Green's Functions in Electromagnetic Theory.* International Textbook Company, 1971.

[117] C.T. Tai. Kirchhoff theory: Scalar, vector, or dyadic ? *IEEE Trans. Ant. Prop.*, 20:114–115, 1972.

[118] D.R. Thompson. Calculation of radar backscatter modulations from internal waves. *J. Geophys. Res.*, 93(C10):12371–12380, 1988.

[119] D.R. Thompson. Calculation of microwave doppler spectra from the ocean surface with a time-dependent composite model. In G.J. Komen and W.A. Oost, editors, *Radar Scattering from Modulated Wind Waves*, pages 27–40. Kluwer Academic Publishers, Dordrecht, The Netherlands, 1989. Proceedings of the Workshop on Modulation of Short Wind Waves in the Gravity-Capillary Range by Non-Uniform Currents, held in Bergen aan Zee, the Netherlands, 24-26 May 1988.

[120] D.J. Thomson. Spectrum estimation and Harmonic analysis. *Proc. IEEE*, 70:1055–1096, 1982.

[121] D.J. Thomson. Multi-Window Bispectrum Estimates. *Proceedings of the Workshop on Higher-Order Spectral Analysis*, pages 19–23, June 28-30 1989. (Sponsored by Office of Naval Research and National Science Foundation, in cooperation with the IEEE societies: Control Systems; Geoscience and Remote Sensing; Acoustics, Speech and Signal Processing).

[122] D.J. Thomson. Quadratic-inverse spectrum estimates: applications to paleoclimatology. *Phil. Trans. R. Soc. Lond. A*, 332:539–597, 1990.

[123] D.J. Thomson. Time series analysis of Holocene climate data. *Phil. Trans. R. Soc. Lond. A*, 330:601–616, 1990.

[124] D.J. Thomson and A.D. Chave. Jackknifed error estimates for spectra, coherences and transfer functions. In S. Haykin, editor, *Advances in Spectrum Analysis and Array Processing, Vol. I*, chapter 2. Prentice-Hall, 1991.

[125] K. Torrance and E. Sparrow. Theory for off-specular reflection from roughened surfaces. *J. Opt. Soc. Am.*, 57:1105–1114, 1967.

[126] R.J.A. Tough and K.D. Ward. Physical mechanisms associated with the compound K-distribution sea clutter model. In *IEE Colloquium on Radar Clutter and Multipath Propagation (Digest No. 62)*, pages 4/1–4, 1989.

[127] D.B. Trizna. Statistics of low grazing angle radar sea scatter for moderate and fully developed ocean waves. *IEEE Trans. Ant. Prop.*, AP-39:1681–1690, 1991.

[128] D.B. Trizna and J.P. Hansen. Laboratory studies of radar sea spikes at low grazing angles. *J. Geophys. Res.*, 96(C7):12529–12537, 1991.

[129] L.A. Tsang, J.A. Kong, and R.T. Shin. *Theory of Microwave Remote Sensing.* John-Wiley, 1985.

[130] F.T Ulaby, R.K. Moore, and A.K. Fung. *Microwave Remote Sensing.* Artech House, Vol. I, 1981; Vol. II, 1982; Vol. III, 1986.

[131] G.R. Valenzuela. Depolarization of EM waves by slightly rough surfaces. *IEEE Trans. Ant. Prop.*, AP-15:552–557, 1967.

[132] G.R. Valenzuela. Theories for the interaction of electromagnetic and oceanic waves — A review. *Boundary-Layer Meteorology*, 13:61–85, 1978.

[133] R.J. Wagner. Shadowing of randomly rough surfaces. *J. Acoust. Soc. Amer.*, 41:138–147, 1967.

[134] S. Watts. Radar detection prediction in sea clutter using the compound K-distribution model. *IEE Proc. F*, 132:613–620, 1985.

[135] S. Watts. Radar detection prediction in K-distributed sea clutter and thermal noise. *IEEE Trans. Aerospace and Electronic Systems*, AES-23:40–45, 1986.

[136] F.J. Wentz. Cox and Munk's sea surface slope variance. *J. Geophys. Res.*, 81(9):1607–1608, 1976.

[137] L.B. Wetzel. A model for sea backscatter intermittency at extreme grazing angles. *Radio Science*, 12:749–756, 1977.

[138] D.P. Winebrenner. *A surface field phase-perturbation technique for scattering from rough surfaces.* Ph.D. dissertation, Univ. of Washington, Seattle, Wash., 1985.

[139] D.P. Winebrenner and A. Ishimaru. Application of the phase-perturbation technique to randomly rough surfaces. *J. Opt. Soc. Am. A*, 2:2285–2294, 1985.

[140] D.P. Winebrenner and A. Ishimaru. Investigation of a surface field phase perturbation technique for scattering from rough surfaces. *Radio Science*, 20:161–170, 1985.

[141] L.B. Wolff. Surface orientation from polarization images. In *Proc. SPIE, Vol. 850, Optics, Illumination, and Image Sensing for Machine Vision II*, pages 110–121, 1987.

[142] L.B. Wolff. Classification of material surfaces using the polarization of specular highlights. In *Proc. SPIE, Vol. 1005, Optics, Illumination, and Image Sensing for Machine Vision III*, pages 206–213, 1988.

[143] L.B. Wolff. Using polarization to separate reflection components. In *Proc. of IEEE Computer Society Conference on Computer Vision and Pattern Recognition*, pages 363–369, San Diego, CA, June 1989.

[144] J.W. Wright. A new model for sea clutter. *IEEE Trans. Ant. Prop.*, AP-16:217–223, 1968.

[145] J.W. Wright. Detection of ocean waves by microwave radar: The modulation of short gravity-capillary waves. *Boundary-Layer Metorology*, 13:87–105, 1978.